

IONOSPHERIC ERROR MODELING FOR HIGH INTEGRITY  
CARRIER PHASE POSITIONING

BY

JASON WILLIAM NEALE

Submitted in partial fulfillment of the  
requirements for the degree of  
Master of Science in Aerospace and Mechanical Engineering  
in the Graduate College of the  
Illinois Institute of Technology

Approved \_\_\_\_\_  
Advisor

Chicago, Illinois  
July 2010



## ACKNOWLEDGMENT

I want to thank my advisor, Professor Boris Pervan, for allowing me the opportunity to carry out this research. His support and guidance throughout this work has been invaluable and greatly appreciated. I value his attention to detail and enthusiasm towards this work. Moreover, I appreciate his effort to instill in me critical thinking qualities that will be beneficial to my career. Special thanks also go to Mathieu Joerger who has worked closely with me and provided valuable insights into this work. In addition, I appreciate his willingness to answer questions as well as his help in the proofreading of this document. I also want to thank my thesis defense and reading committee of Professor Kevin Cassel and Professor Matthew Spenko for their time.

I am also grateful for all of my lab mates in the Navigation and Guidance Lab for their friendship and support: Fang-Cheng Chan, Samer Khanafseh, Livio Gratton, Steven Langel, and Jing Jing.

To Trevor Garner from the University of Texas at Austin, I owe thanks for providing me with actual low earth orbit data used in this work. I am also grateful for Seebany Datta-Barua from the Atmospheric and Space Technology Research Associates who provided me with simulated low earth orbit data and shared her expertise on the ionosphere. Thanks also go to the Boeing Company for sponsoring this work.

I am also grateful for the support and of my family and friends who have stood by me during the course of this research. I especially owe much thanks to my parents, Bob and Laura Neale, for the sacrifices they have made for me throughout the years. Without these sacrifices and their support, I would not have the opportunities I do today. I also want to acknowledge my sister, Angela, for her encouragement and support.

## TABLE OF CONTENTS

	Page
ACKNOWLEDGEMENT .....	iii
LIST OF TABLES .....	vi
LIST OF FIGURES .....	viii
LIST OF ABBREVIATIONS .....	xi
LIST OF SYMBOLS .....	xiii
ABSTRACT .....	xv
 CHAPTER	
1. INTRODUCTION .....	1
1.1 Previous Work .....	5
1.2 Ionospheric Errors and Carrier Phase Positioning .....	9
1.3 Contributions .....	12
2. GPS AND IRIDIUM BACKGROUND .....	14
2.1 Global Positioning System .....	14
2.2 GPS Error Sources .....	15
2.3 GPS Signals and Measurements .....	18
2.4 Iridium .....	19
3. THE IONOSPHERE .....	21
3.1 Effects on Signals .....	22
3.2 Classifying Ionospheric Activity .....	24
3.3 Ionospheric Activity Breakdown .....	27
3.4 Nominal Ionospheric Error Model .....	28
3.5 Using the Nominal Ionospheric Error Model with iGPS .....	34
4. METHODOLOGY FOR EXPERIMENTAL EVALUATION OF THE MODEL .....	36
4.1 Database and Other Sources of Information .....	36
4.2 Method of Data Processing .....	38
4.3 Mathematical Formulation for Nominal Model Evaluation .....	39

5. NOMINAL IONOSPHERE ERROR MODEL EVALUATION .....	48
5.1 Quiet Day Analysis .....	48
5.2 Unsettled Day Analysis .....	69
5.3 Active Day Analysis .....	72
6. MODEL MODIFICATION TO ACCOUNT FOR TRAVELING IONOSPHERIC DISTURBANCES.....	76
6.1 Quadratic Model .....	76
6.2 Sinusoidal Model .....	81
7. MODEL EVALUATION USING LOW EARTH ORBIT DATA.....	98
7.1 Simulated Data.....	98
7.2 Actual Low Earth Orbit Data.....	106
8. CONCLUSIONS AND FUTURE WORK .....	118
8.1 Summary of Error Model Evaluation .....	118
8.2 Review of Contributions .....	121
8.3 Future Work .....	123
BIBLIOGRAPHY.....	126

## LIST OF TABLES

Table	Page
3.1. Relationship between Daily Single Station Index $A_K$ and Ionospheric Activity .....	26
3.2. Ionospheric Activity Breakdown by Year.....	27
3.3. Ionospheric Activity for Days between 1997 and 2007 .....	28
5.1. CORS Sites used for Model Evaluation.....	48
5.2. Values used for Measurement Vector Augmentation .....	49
5.3. Estimated Parameter Values for Quiet Ionospheric Days with Original Error Model.....	64
5.4. Summary of Winter and Summer Wave Analysis .....	68
5.5. Wave Occurrences in Winter and Summer.....	68
5.6. Estimated Parameter Values for Unsettled Ionospheric Days with Original Error Model.....	72
5.7. Estimated Parameter Values for Active Ionospheric Days with Original Error Model.....	75
6.1. Estimated Parameter Values for Quiet Ionospheric Days with Quadratic Error Model.....	81
6.2. Prior Knowledge for Sinusoidal Model States.....	87
6.3. Estimated Parameter Values for Quiet Ionospheric Days with Sinusoidal Error Model.....	94
7.1. Estimated Parameter Values for Simulated LEO Data with Original Error Model.....	102
7.2. Estimated Parameter Values for Simulated LEO Data with Quadratic Error Model.....	106
7.3. Sites used in Actual LEO Data Analysis.....	107
7.4. Estimated Parameter Values for Actual LEO Data with Original Error Model.....	110

7.5.	Estimated Parameter Values for Actual LEO Data with Quadratic Error Model .....	113
7.6.	Estimated Parameter Values for Actual LEO Data with Sinusoidal Error Model .....	117

## LIST OF FIGURES

Figure	Page
1.1. GPS and Iridium Constellations [20] .....	4
1.2. Worldwide WAAS Ionospheric Grid Points (Bands 9 and 10 not shown) [31].....	7
2.1. GPS Error Sources .....	17
3.1. Relative Electron Density Profile with Layers of the Ionosphere.....	21
3.2. Top View of Earth-Sun System with Error Model Assumptions.....	29
3.3. Bias and Gradient Modeling of Ionospheric Errors .....	32
5.1. Analysis of Residual Errors for Determining Model’s Linearity Limit.....	50
5.2. System Availability versus Maximum IPP Displacement [21].....	52
5.3. Data and Model for 700-800 km Segment at Houston, Texas .....	54
5.4. Model Analysis for 700-800 km Segment at Houston, Texas .....	55
5.5. Model Analysis for 700-800 km Segment at Cleveland, Ohio .....	56
5.6. Model Analysis for 700-800 km Segment at Battle Creek, Michigan .....	56
5.7. Model Analysis for 700-800 km Segment at Los Angeles, California .....	57
5.8. Data and Model for 700-800 km Segment at Miami, Florida .....	58
5.9. Model Analysis for 700-800 km Segment at Cleveland, Ohio.....	59
5.10. Model Analysis for 700-800 km Segment at Salt Lake City, Utah .....	59
5.11. Model Analysis for 700-800 km Segment at Miami, Florida.....	60
5.12. Model Analysis for 700-800 km Segment at Holland, Michigan.....	60
5.13. Folded Residual CDF for Quiet Ionospheric Days .....	62
5.14. Worst Case Residual Example for Holland, Michigan.....	63
5.15. Worst Case Residual Example for Cleveland, Ohio.....	63

5.16. Segments Exhibiting Wave Events in January 2007 .....	66
5.17. Segments Exhibiting Wave Events in July 2007 .....	67
5.18. Data and Model for Unsettled Day Example at Holland, Michigan.....	69
5.19. Unsettled Day Example at Holland, Michigan (1/2/07) .....	70
5.20. Unsettled Day Example at Holland, Michigan (4/30/07) .....	70
5.21. Folded Residual CDF for Unsettled Ionospheric Days.....	71
5.22. Data and Model for Active Day Example at Holland, Michigan .....	72
5.23. Active Day Example at Holland, Michigan (1/30/07).....	73
5.24. Active Day Example at Holland, Michigan (5/23/07).....	73
5.25. Folded Residual CDF for Active Ionospheric Days .....	74
6.1. Original and Quadratic Model Comparison at Holland, Michigan.....	78
6.2. Original and Quadratic Model Comparison at Cleveland, Ohio.....	79
6.3. Original and Quadratic Model Comparison at Salt Lake City, Utah .....	79
6.4. Original and Quadratic Model Comparison at Holland, Michigan.....	80
6.5. Folded Residual CDF Comparison between Original and Quadratic Models .....	80
6.6. Original and Sinusoidal Model Comparison at Holland, Michigan .....	90
6.7. Original and Sinusoidal Model Comparison at Cleveland, Ohio .....	90
6.8. Original and Sinusoidal Model Comparison at Holland, Michigan .....	91
6.9. Original and Sinusoidal Model Comparison at Miami, Florida .....	91
6.10. Original and Sinusoidal Model Comparison at Houston, Texas.....	92
6.11. Original and Sinusoidal Model Comparison at Holland, Michigan .....	92
6.12. Comparison of Folded Residual CDFs for Original and Sinusoidal Models.....	93

6.13. Non-Converging Segment at Miami, Florida .....	96
6.14. Non-Converging Segment at Salt Lake City, Utah.....	96
6.15. Non-Converging Segment at Battle Creek, Michigan .....	97
7.1. Simulated LEO Data Residual Variation - Example 1.....	100
7.2. Simulated LEO Data Residual Variation - Example 2.....	101
7.3. Folded Residual CDF for Original Model with Simulated LEO Data.....	101
7.4. Simulated LEO Data Residual CDF Outlier - Example 1.....	103
7.5. Simulated LEO Data Residual CDF Outlier - Example 2.....	103
7.6. Original and Quadratic Model Comparison with Simulated LEO Data .....	104
7.7. Folded Residual CDF Comparison for Original and Quadratic Models with Simulated LEO Data.....	105
7.8. Original Model Applied to Actual LEO Data at Albany, New York.....	108
7.9. Original Model Applied to Actual LEO Data at Austin, Texas .....	108
7.10. Original Model Applied to Actual LEO Data at Oneonta, New York.....	109
7.11. Folded Residual CDF for Original Model with Actual LEO Data .....	110
7.12. Original and Quadratic Model Comparison with Actual LEO Data at Albany, New York.....	111
7.13. Original and Quadratic Model Comparison with Actual LEO Data at Austin, Texas .....	111
7.14. Folded Residual CDF Comparison for Original and Quadratic Models with Actual LEO Data .....	112
7.15. Original and Sinusoidal Model Comparison with Actual LEO Data at Austin, Texas .....	114
7.16. Original and Sinusoidal Model Comparison with Actual LEO Data at Albany, New York.....	115
7.17. Folded Residual CDF Comparison for Original and Sinusoidal Models with Actual LEO Data .....	116

## LIST OF ABBREVIATIONS

Abbreviation	Definition
AGW	Atmospheric Gravity Wave
CIDR	Coherent Ionospheric Doppler Receiver
CONUS	Contiguous United States
CORS	Continuously Operating Reference Stations
COSMIC	Constellation Observing System for Meteorology, Ionosphere, and Climate
FAA	Federal Aviation Administration
GPS	Global Positioning System
GSM	Geocentric Solar Magnetospheric
IPP	Ionospheric Pierce Point
IRI	International Reference Ionosphere
LAAS	Local Area Augmentation System
LEO	Low Earth Orbit
LOS	Line Of Sight
MEO	Medium Earth Orbit
MOPS	Minimum Operational Performance Standards
NAVCEN	United States Coast Guard Navigation Center
NGS	National Geodetic Survey
OCS	Operational Control Segment
OSCAR	Orbiting Satellite Carrying Amateur Radio
RADCAL	Radar Calibration

SV	Space Vehicle
SWPC	Space Weather Prediction Center
TEC	Total Electron Content
TID	Traveling Ionospheric Disturbance
UTC	Coordinated Universal Time
WAAS	Wide Area Augmentation System

## LIST OF SYMBOLS

Symbol	Definition
$\theta_k$	Satellite Elevation Angle
$c$	Speed of Light in a Vacuum ( $2.997925 \times 10^8$ m/s)
$R_E$	Radius of the Earth (6,378 km)
$h_I$	Ionospheric Shell Height (350 km)
$f_{L1}$	GPS L1 Frequency (1575.42 MHz)
$f_{L2}$	GPS L2 Frequency (1227.60 MHz)
$f_{IRIDIUM}$	Iridium Frequency (1624 MHz)
$r_k$	True Range from Satellite to User
N	Carrier Phase Cycle Ambiguity
$\rho_k$	Code Phase Pseudorange
$\phi_{L1}$	L1 Frequency Carrier Phase Measurement (Cycles)
$\phi_{L2}$	L2 Frequency Carrier Phase Measurement (Cycles)
$I_k$	Ionospheric Delay
$T_k$	Tropospheric Delay
$E_k$	Orbit Ephemeris Error
$\epsilon_{\rho,k}$	Code Phase Measurement Noise
$\epsilon_{\phi,k}$	Carrier Phase Measurement Noise
$\delta t_u$	Receiver Clock Bias
$\delta t^s$	Satellite Clock Bias
$\lambda_{L1}$	L1 Frequency Wavelength (19.03 cm)

$\lambda_{L2}$	L2 Frequency Wavelength (24.42 cm)
$d_{IPP,k}$	Ionospheric Pierce Point Displacement
$\epsilon_{I,k}$	Ionospheric Delay on Carrier Phase Measurements
$c_{OB,k}$	Obliquity Factor
$b_{VI}$	Vertical Ionosphere Bias
$g_{VI}$	Vertical Ionosphere Gradient
$q_{VI}$	Quadratic Coefficient
$b$	Inter-frequency and Cycle Ambiguity Bias
$a_C$	Cosine Amplitude in Sinusoidal Model
$a_S$	Sine Amplitude in Sinusoidal Model
$f_{TID}$	TID Frequency in Sinusoidal Model

## ABSTRACT

The Global Positioning System's (GPS) carrier phase measurements can provide centimeter-level positioning accuracy. To achieve this precise positioning, cycle ambiguities must be estimated, which typically requires the use of differential GPS and filtering measurements over long periods of time. Augmenting GPS with low earth orbit (LEO) satellites helps to overcome these restrictions. In this work, a system called iGPS is investigated, which is the combination of GPS and LEO Iridium telecommunications satellites.

An added complication to accurately estimating cycle ambiguities is that satellite signals are subject to many error sources; the largest and most sensitive being a dispersive region of the atmosphere known as the ionosphere, whose effects vary with time of day, location, season, and eleven-year-long solar cycles. For accurate cycle ambiguity estimation in a non-differential system, the effects of the ionosphere must be precisely modeled.

Current GPS ionospheric error models are not accurate enough for precise non-differential carrier phase positioning, and the addition of Iridium satellites makes them even less accurate. This is because of the fast motion of LEO satellites, which generate large displacements across the ionosphere in short periods of time. Over these displacements, error variations induced by the ionosphere are much larger than with GPS.

This work seeks to evaluate an ionospheric error model applicable to GPS and LEO satellite signals. To avoid adding uncertainty to the positioning solution, which lowers navigation system availability, the model must be described with a minimal number of parameters. The model must also be demonstrated to accurately fit large

amounts of actual ionospheric error data to help validate the integrity for the navigation system. Model evaluation is carried out using experimental data from GPS and LEO satellites. Methods for processing this experimental data are developed, and the model is applied to the processed data in a piece-wise linear manner. Based on the results, a piece-wise quadratic model is derived to decrease residual errors. Observed decimeter-level residual errors are shown to result from Traveling Ionospheric Disturbances (TIDs). To account for TIDs, a nonlinear error model is derived, applied to the data, and shown to offer significant reduction in residual magnitudes.

## CHAPTER 1

### INTRODUCTION

Satellite navigation is exploited in increasingly complex applications, such as autonomous shipboard landing of aircraft and autonomous navigation of ground-based vehicles [20]. These tasks require that the navigation system provide highly precise measurements. The most widely used satellite navigation system currently in operation that is called upon for these complex applications is the Global Positioning System (GPS).

GPS, which will be discussed in detail in chapter 2, broadcasts data on two microwave carrier frequencies, known as L1 and L2. Most civilian users only have access to L1 as dual frequency capability for civilian use is not expected until 2015 or later [26]. Modulated on these carrier signals is the code phase, which provides an absolute range between the satellite and user based on signal travel time. In addition, ranging can also be accomplished through the carrier signal itself. The ranging measurements based on the carrier signal, known as carrier phase measurements, are much more precise than code phase (due to a much smaller wavelength and lower measurement noise; more in chapter 2). For this reason, carrier phase measurements are preferred when extremely high accuracy is needed.

However, a problem with using carrier phase is the fact that these measurements are biased by an unknown number of cycles, which are often referred to as cycle ambiguities. Roughly speaking, cycle ambiguities represent the integer number of cycles of the carrier phase signal between the satellite and receiver. Thus to achieve highly precise positioning using GPS, these unknown cycle ambiguities must be estimated. Once

cycle ambiguities have been determined, carrier phase measurements have the capability to provide centimeter-level positioning accuracy, although, due to slow satellite motion, a considerable period of time is required to reliably estimate these ambiguities. This makes carrier phase positioning difficult for applications where precise real-time positioning is required. Satellite motion is important in the estimation of cycle ambiguities because the change in satellite geometry induced by the motion aids in distinguishing ambiguities from other contributions to the measurement.

An added complication to the accurate estimation of cycle ambiguities is that GPS signals are subject to a variety of error sources, with the largest and most sensitive being a dispersive region of the atmosphere known as the ionosphere. Approaches for removing the majority of the ionospheric error to improve the reliability of the cycle ambiguity estimation process can be employed.

One such method is to utilize differential corrections from a local reference station that can be applied to GPS measurements in order to account for ionospheric errors. For instance, corrections can be provided from ground stations belonging to the Wide Area Augmentation System (WAAS), which will be discussed shortly.

Another technique to reduce the effect of ionospheric errors involves the use of dual frequency (L1 and L2) measurements for constructing ionosphere-free measurements. Since the effect of the ionosphere is related to signal frequency, measurements can be used in combination to eliminate most of the ionospheric error, leaving a small residual error which can be more easily dealt with. The drawback to the ionosphere-free approach is that the measurement noise increases by a factor of approximately three [26].

Single frequency code and carrier phase measurements can also be employed to reduce ionospheric errors. The fact that the ionosphere causes a delay on code measurements and an advance on carrier phase measurements can be exploited to estimate the change in ionospheric delay over time. The change in ionospheric delay over time can be determined since the code delay and carrier advance are equal and opposite in magnitude. This is known as code-carrier divergence [17].

In the context of this work, the aforementioned approaches to mitigating ionospheric errors cannot be used. Since the overall goal is to provide precise positioning over large areas, no local reference stations are assumed to be nearby (which eliminates the possibility for differential ionospheric corrections). For this reason, non-differential single frequency carrier phase measurements are employed because, as noted earlier, only single frequency L1 measurements are utilized in civil navigation. (Technically, data at the L2 frequency is available, and will be used in the experimental validation portion of this work, but it cannot be relied upon in real-time navigation systems for civil aviation.)

Using non-differential single frequency carrier phase measurements means that accurate modeling of ionospheric errors must be performed to mitigate the effects of the ionosphere on the cycle ambiguity estimation process. The observation, analysis, and modeling of ionospheric errors are the source of this work.

Proper modeling of ionospheric errors will help to alleviate some of the difficulty in estimating cycle ambiguities, but the issue of estimating these ambiguities for real-time positioning still remains due to slow satellite motion. A solution to this problem is to augment the GPS system with another satellite constellation in an effort to induce satellite geometry changes that allow cycle ambiguities to be estimated more quickly. In

order to achieve very fast geometry changes, combining GPS with a low earth orbit (LEO) constellation is an attractive option. This is because LEO satellites appear to move across the sky much faster than GPS satellites as viewed from a location on the earth. Consequently, a greater change in satellite geometry is attained and can be exploited to quickly estimate cycle ambiguities. One such example of a LEO system with which GPS can be augmented is the Iridium telecommunications satellite constellation. The combination of these constellations is called iGPS, which makes precise and real-time positioning using carrier phase a possibility over large areas. The iGPS system considered in this work is assumed to be a single frequency system in order to make it applicable to civil navigation (where only the L1 frequency can be relied upon). The GPS (outer) and Iridium (inner) constellations are depicted in figure 1.1; more details about these constellations will be given in the next chapter.

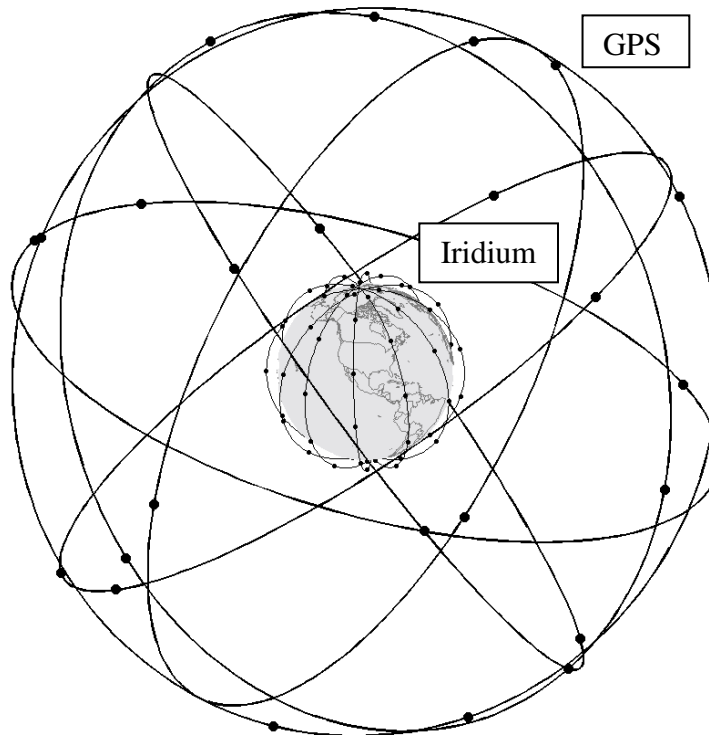


Figure 1.1. GPS and Iridium Constellations [20]

Before moving on, a discussion of previous work conducted on ionospheric errors and the iGPS system is provided.

## **1.1 Previous Work**

Work has been done on how to set up the iGPS system to provide users with high precision carrier phase positioning over large areas [20-22]. Since the ionospheric delay causes the largest error for single frequency systems, work has gone into understanding how these errors behave. Using knowledge of error behavior, reliable means of reducing ionospheric errors have been devised in an attempt to increase positioning performance. These are discussed below.

**1.1.1 Characteristics of Ionospheric Delays.** It has been determined that, unlike other error sources affecting the transmitted signals, vertical ionospheric delays do not follow similar trends from day to day. The vertical delay is defined as the error that would be experienced if the signal penetrated the ionosphere perpendicularly. It is computed using the delay along the line-of-sight from the satellite to the receiver (slant delay) and the elevation angle of the satellite. In fact, the magnitudes of these delays are influenced by a number of factors, including the time of day, season, location, and time in the solar cycle. Moreover, the change in the vertical delay over a satellite pass as a function of time has been found to vary linearly over short time intervals [28].

The linear behavior of the vertical ionospheric delay over limited time periods has also been documented in [14] through a correlation analysis of the errors applicable to the WAAS system [15]. For days when the ionosphere is quiet (non-stormy), the vertical delay has been shown to vary linearly for ionospheric pierce point (IPP) displacements up to 2,000 km. Results of this work indicate that the delay does behave in a predictable

fashion for mid-latitude locations and quiet ionospheric days. This suggests that a linear vertical ionospheric error model may work well provided it is applied over a limited range of distances (which will not be the same as with the WAAS application).

When stormy days are encountered in the WAAS correlation analysis, the regularity of the error distribution vanishes and no linear trend is present [14]. In addition, the errors on stormy days become decorrelated much faster as compared to quiet days [28].

**1.1.2 Modeling and Correcting for Ionospheric Errors.** Several methods have been developed to help single frequency systems account for ionospheric errors. These methods either provide the user with corrections to account for the error or provide a way to obtain an estimate of the delay itself.

Ionosphere error modeling has been incorporated into the two systems used for civil aviation applications, namely the Local Area Augmentation System (LAAS) [30] and WAAS [31]. These systems, developed by the Federal Aviation Administration (FAA), aim at providing users with ground corrections that can be applied to their ranging measurements. These corrections help to improve positioning accuracy by accounting for a majority of the ionospheric error.

The WAAS system utilizes measurements collected from a network of ground stations based across the United States to generate differential corrections of the ionospheric error. To construct these corrections, the ionosphere is modeled as a thin shell at an altitude of 350 km [14, 15]. An imaginary grid is laid out on the thin shell with ionospheric grid points (IGPs) located at the intersection of lines of constant geodetic latitude and lines of constant geodetic longitude spaced every five degrees between 55

degrees north latitude and 55 degrees south latitude [31]. Other IGPs exist outside this region, but are less densely spaced. IGPs are located within 11 different bands which are numbered from zero to ten. Figure 1.2 shows the location of worldwide IGPs within bands zero through eight (nine and 10 are not shown). Ionospheric corrections are computed at each IGP and then uplinked to satellites in geostationary orbit. These geostationary satellites subsequently broadcast the corrections to the users. More detailed information about IGP bands and the computation of ionospheric corrections at each IGP can be found in [31]. Deficiencies with WAAS for carrier phase navigation exist, and will be discussed shortly.

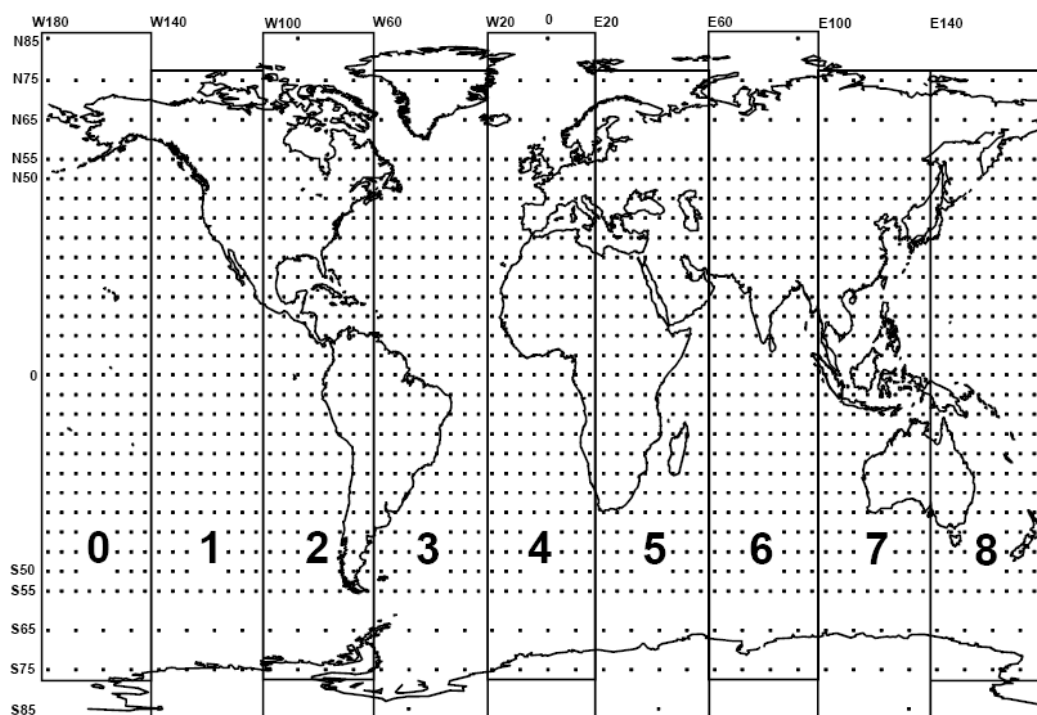


Figure 1.2. Worldwide WAAS Ionospheric Grid Points (Bands 9 and 10 not shown) [31]

Other methods have tried to improve the accuracy of WAAS ionospheric corrections. The error introduced by the ionosphere is directly related to the density of electrons within this medium. Thus, if the density could be determined, it would aid in

providing a way to take the delay into account. In [13], a tomographic approach is used to produce a real time estimate of the electron density. This density estimate is derived from the collection of total electron content (TEC) data obtained from dual frequency receivers. The density estimate can then be implemented to improve the WAAS correction of the ionospheric error.

LAAS is a system which has the capability to provide differential ionospheric corrections to aircraft on final approach. These corrections are broadcast to the users directly from the closest ground facility. LAAS ground stations are based on or near airports. The broadcasted corrections, although accurate, are only valid for the area in the immediate vicinity of the ground facility.

Another method for determining ionospheric delays, which is less accurate, involves using the principle of code-carrier divergence, introduced earlier. This method helps to improve the accuracy of the single frequency user's position [3]. Differencing code and carrier measurements from a single epoch leaves the cycle ambiguity and twice the ionospheric delay (along with increased measurement noise), which are unable to be distinguished from one another. This problem is avoided if the delay is mapped from the vertical domain to a line of sight domain through an obliquity factor. Since the obliquity factor changes as function of satellite elevation, the delay and ambiguity can be distinguished and estimated in real time to improve positioning performance.

**1.1.3 iGPS System.** Much of the groundwork for the iGPS system has been devised in [20-22]. Single frequency iGPS capability is assumed and a basis for the envisioned architecture of the user, space, and ground segments is provided. Positioning algorithms based on highly precise carrier phase measurements have been developed. The error

models for the various error sources are also derived, with the linear vertical ionospheric error model serving as the starting point for the analysis to be carried out in this work.

This prior work indicates that single frequency iGPS is close to meeting some of the most difficult requirements in place for civil aviation today [21].

## **1.2 Ionospheric Errors and Carrier Phase Positioning**

The methods of modeling or correcting for ionospheric errors that have been discussed provide ways to increase positioning performance by decreasing the effect of the ionosphere. For carrier phase positioning, these methods are not sufficient, thereby necessitating the need for a new error model. A new model is even more imperative with the addition of LEO satellites.

The insufficiency of GPS ionospheric error mitigation methods results from the fact that, in order to estimate cycle ambiguities, the variation of the ionospheric residual error over time must be accurately accounted for. Previous research on the iGPS system [20-22] has shown that capturing the dynamics of the residual variation is a major driver for increasing the positioning performance of the system. For this reason, an error model intending to support carrier phase navigation must be able to track these variations over time.

Current GPS ionosphere models do not provide the ability to track the dynamics of the error. For example, the Klobuchar model [26] requires the input of four coefficients which are transmitted in the GPS navigation message. Due to constraints with the data transmission rate of GPS, these coefficients are only updated a few times a day. Thus, there is no way to gain information about ionospheric dynamics in the time

between coefficient updates. Moreover, the Klobuchar model is only able to account for about 50% of the error caused by the ionosphere.

The WAAS ionosphere model is also unable to capture the dynamics of the error. This is due to poor spatial and temporal resolution of the corrections. The poor resolution follows from the fact that the grid points from where the corrections are derived are separated by large distances. In addition, even though the corrections are absolute, they are only updated every few minutes and their accuracy is not good enough for carrier phase, as meter-level residual errors remain after applying them. Moreover, LAAS is also insufficient for general use. LAAS corrections are not absolute and, although accurate over time, are only valid near the ground station.

Existing ionosphere error models and corrections are inadequate with GPS signals to perform carrier phase positioning, and adding LEO satellites will make them even worse. Due to the low orbital altitude of LEO satellites, a large displacement across the ionosphere will be traced by these vehicles over short periods of time. Over these displacements, error variations induced by the ionosphere are much larger than with GPS and make existing error models even less accurate.

While an ionospheric model that allows for carrier phase positioning needs to make up for where GPS models are lacking, at the same time, it must not compromise any of the four quantities which describe a navigation system's performance. These quantities include accuracy, integrity, continuity, and availability. Accuracy can be thought of as the variation of the system output from truth given fault-free conditions. Most often, accuracy is given in terms of a 95% confidence level. Integrity is the capability of the system to provide users with timely warnings when the system should

not be used. The integrity risk is the probability that an undetected error or failure from the system introduces hazardously misleading information. Continuity is related to the system's ability to support accuracy and integrity requirements over the course of a mission. The continuity risk is the probability that a detected but unexpected error or fault happens after the mission has been started. Lastly, availability refers to the fraction of time the navigation system can be implemented to support a mission. This time is based on the system's ability to meet accuracy, integrity, and continuity requirements.

Availability and integrity help dictate the form of the ionospheric error model serving as the starting point for this work (model will be introduced in chapter 3). As mentioned earlier, signals traveling from satellite to user are subject to other errors in addition to the ionosphere. In the iGPS positioning algorithm described in [20-22], each of these error sources has its own error model similar to that for the ionosphere. Each of these models contains unknown parameters. This means that the positioning algorithm must estimate the user position, the cycle ambiguity, and the parameters in the error models, all of which have a degree of uncertainty. The uncertainty in these estimated quantities contributes to greater uncertainty of the final position estimate, leading to a decrease in the overall system availability. High integrity can be ensured by increasing the number of parameters in the error model to more accurately capture the ionosphere, but the increase in parameters will be detrimental to availability. For this reason, the ionospheric error model must not exhibit unnecessary complexity or employ exotic basis functions with a large number of model parameters.

The iGPS positioning algorithms introduced above require prior knowledge on the parameters in each error model. This prior knowledge is expressed as bounding values on

each parameter's probability distribution. In the case of the ionospheric error model, these bounding values will be determined through an evaluation of the error model from applying it to large amounts of data. Application of the model to substantial amounts of data will make sure that the results have statistical significance. Evaluation of the model is conducted in chapters 5-8.

### **1.3 Contributions**

The following contributions have been made while working on ionospheric error modeling for the iGPS system.

#### **1.3.1 Development of Methods and Algorithms to Analyze and Categorize**

**Ionospheric Errors using Multiple Sources of Experimental Data.** Algorithms and methods needed to process dual-frequency measurements have been developed. The processed data is used to measure, analyze, and categorize ionospheric delays based on such parameters as location, time of the day, level of ionospheric activity, and satellite elevation. These methods and algorithms have been applied to GPS data, and also to simulated and actual data from LEO satellites currently in orbit.

#### **1.3.2 Analysis and Quantification of the Accuracy of a Linear Model for the**

**Vertical Ionospheric Delay.** Analysis of experimental data in the form of dual-frequency carrier phase GPS measurements collected from Continuously Operating Reference Stations (CORS) over many months at several locations has been performed. After fitting the error model to the data, residual errors were found to exceed decimeter-level magnitudes. These decimeter-level residuals have been shown to be the product of a phenomenon present in the ionosphere known as Traveling Ionospheric Disturbances, or

TIDs, whose magnitude, dynamic behavior, and likelihood of occurrence have been studied. TIDs are discussed in detail in chapter 3.

### **1.3.3 Development and Evaluation of a Piece-wise Linear and a Piece-wise**

**Quadratic Model for the Vertical Ionospheric Delay.** From the analysis of the experimental data, an upper limit on the displacement over which the model can be applied and the vertical ionospheric error will vary linearly has been determined. As a result of this limit, the model must be applied in a piece-wise linear fashion to each satellite pass instead of considering an entire pass at once. In addition to applying the piece-wise model to the data and quantifying the residual errors, nominal parameter values and the corresponding standard deviations for the states within the model have been estimated. This information is needed to construct the required prior knowledge for the iGPS carrier phase positioning algorithms described in [20-22]. Based on observations of the experimental data, a piece-wise quadratic model has also been formulated and shown to decrease residual magnitudes.

### **1.3.4 Derivation and Testing of a New Non-Linear Ionospheric Error Model to**

**Account for TIDs.** Since TIDs have been found to produce wave-like variations in the residual error over time, a new harmonic model has been derived. This model takes into account the effect of TIDs in an attempt to lower residual magnitudes. Nonlinear estimation procedures for obtaining nominal parameter values and standard deviations for the states in the model have been devised and evaluated using experimental data. The results with the new harmonic model have been compared to those with the model presented in [20-22]. This comparison shows that the new model offers a significant improvement in terms of observed residual magnitudes.

## CHAPTER 2

### GPS AND IRIDIUM BACKGROUND

An overview of the Global Positioning System (GPS) and Iridium is given below.

#### **2.1 Global Positioning System**

GPS, whose first satellite was launched in 1978, became fully operational in 1995 [26]. It is a space-based satellite navigation system consisting of 24 satellites occupying six orbital planes (constellation is shown in figure 1.1). These orbital planes are inclined with respect to the equator by an angle of 55 degrees. The four satellites within each plane are not evenly spaced [35]. The uneven spacing is implemented to minimize the loss of system performance if one of the satellites develops a problem and must be taken offline.

GPS satellites reside in medium earth orbit (MEO), which encompasses altitudes between 5,000 km and 20,000 km. The near circular orbits of the satellites, at an altitude of 20,192 km, enables an orbital period of 11 hours, 58 minutes, and 2 seconds to be attained. This period corresponds to half of a sidereal day. As a result, satellites repeat their ground tracks every sidereal day.

GPS is a passive system. This means it can handle an unlimited number of users since it does not require user interaction. The system works on the principle of trilateration. If the satellites and the user receiver are synchronized to GPS time, a signal transit time can be computed which can be converted to a ranging measurement between the satellite and the user. If there are at least three ranging measurements available, the three components of the user's position can be determined. However, user receivers have quartz clocks which deviate from GPS time and cause miscalculations of the signal

transit time. This matter can be resolved if a fourth satellite is visible, which is used to compute the deviation of the receiver clock from GPS time. This provides the user with a four-dimensional solution of position and time.

**2.1.1 GPS System Architecture.** The GPS system consists of three distinct parts known as the control, user, and space segments. The space segment is composed of the 24 active satellites whose payloads enable broadcasting of navigation data and ranging measurements. The user segment is comprised of all GPS receivers that obtain the broadcast data from the space segment. For example, these receivers can be on aircraft, automobiles, or surveying equipment. The control segment, sometimes called the Operational Control Segment (OCS), is made up of ground stations which monitor the satellites' health. In addition, the OCS performs orbit determination and clock estimation, which is uplinked to the satellites and subsequently broadcast to the user segment. For the satellites to maintain proper orbits, occasional maneuvers must be conducted. These maneuvers are planned and executed by the OCS.

## **2.2 GPS Error Sources**

The measurements obtained by the user receiver from the space segment are subject to a variety of errors. These errors are a result of many factors, including signal propagation through various layers of the atmosphere, satellite orbit determination, and satellite clock estimation. These sources of error are discussed below, with the exception of the ionosphere, which is the focus of this work, and will be discussed in greater detail in the next chapter. The ionosphere is the most sensitive and usually the largest source of error in GPS.

Based on the predicted information uplinked by the OCS, each satellite broadcasts data unique to itself that provides information on its orbit and clock. Parameters broadcast about the satellite's position are known as the orbit ephemeris. The estimation of the orbit ephemeris parameters introduces errors in the ranging measurements between satellite and user, known as the orbit ephemeris error.

The broadcasted clock information also introduces errors to the ranging measurements since this information is estimated by the OCS together with the orbit ephemeris parameters. Clock information is used to correct for the satellite clock bias. This bias, which is different for each satellite, represents the deviation of the individual atomic clocks onboard the satellites from GPS system time. This means the satellite and receiver clocks will not be properly synchronized and the signal transit time will be incorrectly computed. The satellite clock bias can be reduced by applying the broadcasted clock correction parameters. However, even after applying these corrections, residual errors due to satellite clock drift can reach up to two meters.

Another source of error for the signals is caused by the troposphere, a non-dispersive layer of the atmosphere existing at altitudes between sea-level and 18 km. The troposphere causes signals propagating through it to be refracted, leading to a delay in the travel time. In order to mitigate tropospheric delays, numerous error models exist to calibrate the error. One popular choice is the Hopfield model [26]. After applying a model to account for tropospheric error, there is typically still about 0.3 m of residual error.

The noise produced by the receiver itself can also have an impact on the arriving signal. Components of the receiver, such as cables, or thermal effects from processes

within the receiver, generate noise that is picked up by the antenna along with the incoming signal. The signal can be distorted by this extra noise if there is a low signal-to-noise ratio. This is most often the case when the satellite transmitting the signal is at low elevation. Therefore, the impact of receiver noise varies with the elevation of the satellite, but typically causes about 0.2 cm of error for carrier phase measurements.

The term multipath is employed to designate a signal reaching an antenna from two or more paths after reflecting off nearby structures. The reflected signals usually have a lower power than the direct signal, but the resulting ranging measurements are constructed from the sum of all the signals reaching the antenna. Multipath can cause up to about two centimeters of error for carrier phase measurements.

Figure 2.1 depicts code and carrier phase data (explained shortly) being broadcast from a satellite. The various error sources described above are also shown to illustrate where the signal is affected throughout its path from the satellite to the receiver. A closer view of the receiver is given in the lower left of the figure in order to show multipath.

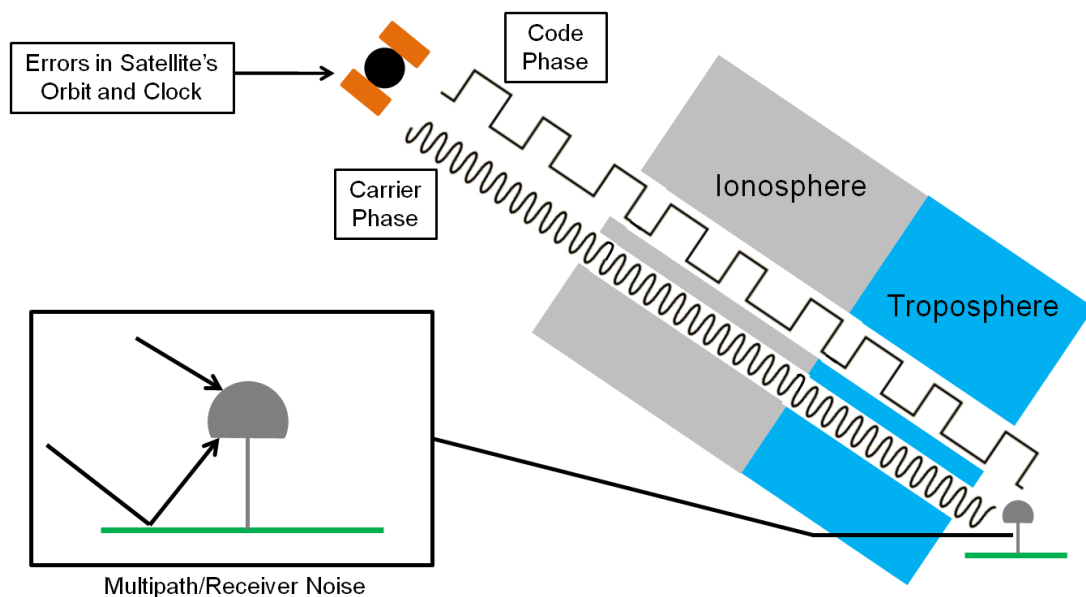


Figure 2.1. GPS Error Sources

### 2.3 GPS Signals and Measurements

As mentioned previously in chapter 1, GPS satellites broadcast data via two carriers whose frequencies are in the microwave band. These frequencies are known as L1 and L2. L1 is centered at 1575.42 MHz while L2 is centered at 1227.60 MHz. Most civilian users only have access to the L1 frequency.

Ranging measurements can be obtained from either the code phase or carrier phase. Code phase measurements are formed by converting the receiver-measured signal transit time into a range (distance). Since the receiver and satellite clocks are not synchronized, the range will be biased. For this reason, the code phase measurement is referred to as a pseudorange. The pseudorange,  $\rho_k$ , for a time epoch,  $k$ , is given as follows:

$$\rho_k = r_k + c\delta t_{u,k} - c\delta t_k^s + I_k + T_k + E_k + \varepsilon_{\rho,k} \quad (2.1)$$

where:

$r_k$  : true range between user and satellite

$c$  : speed of light in a vacuum ( $2.997925 \times 10^8$  m/s)

$\delta t_{u,k}$  : user clock bias

$\delta t_k^s$  : satellite clock bias

$I_k$  : ionospheric delay

$T_k$  : tropospheric delay

$E_k$  : orbit ephemeris error

$\varepsilon_{\rho,k}$  : code phase measurement noise

The carrier phase of the GPS signals can also be used to obtain ranging measurements. However, when using the carrier phase, the cycle ambiguity,  $N$ , is

unknown. This ambiguity is effectively the integer number of whole cycles of the carrier phase wave between the satellite and user. It results from the fact that the user receiver can only track the carrier phase with modulus  $2\pi$ . The value of  $N$  remains the same for a particular satellite as long as the user receiver maintains lock on it. The equation for the carrier phase ranging measurement, at an epoch,  $k$ , in meters, is given below:

$$\lambda\phi_k = r_k + c\delta t_{u,k} - c\delta t_k^s + \lambda N - I_k + T_k + E_k + \varepsilon_{\phi,k} \quad (2.2)$$

The  $\lambda$  factor in equation 2.2 is the wavelength of the carrier frequency and is used to convert the measurement from cycles into a range. For the L1 frequency, the wavelength is 19.03 cm and for L2 the wavelength is 24.42 cm.

The carrier phase measurement noise,  $\varepsilon_{\phi,k}$ , is much smaller than  $\varepsilon_{\rho,k}$ . Usually,  $\varepsilon_{\rho,k}$  is around 0.5 m while  $\varepsilon_{\phi,k}$  is near 0.5 cm. This means the carrier phase is more precise than code phase. Although the carrier phase is more precise, it is also ambiguous as a result of the cycle ambiguity. Conversely, code phase measurements are unambiguous but are much less precise.

It is to be noted that the ionosphere causes a delay on code phase measurements and an advance on carrier phase measurements. For this reason, the ionosphere term,  $I_k$ , in equation 2.1 is positive, while in equation 2.2, it is negative.

## 2.4 Iridium

Iridium is a telecommunications satellite system which first became operational in November of 1998 [9]. It consists of 66 active satellites arranged in six orbital planes with eleven satellites in each (constellation depicted in figure 1.1). These planes have an inclination angle with respect to the equator of 86.4 degrees. Due to the near polar orientation of the orbits, at any given time there is a higher concentration of satellites near

the poles than near the equator, and there is pronounced north-south directionality to the satellite motion.

Iridium satellites are found in low earth orbit (LEO) at an altitude of 780 km. The orbital period for these vehicles is 100 minutes and 28 seconds. This period limits the amount of time the spacecraft are visible over a particular site to about ten minutes [22].

For an observer on earth, Iridium satellites appear to be moving 30 times faster than GPS satellites over the same period of time [20]. This means that, in a given time, a greater distance across the sky will be covered by Iridium satellites as compared to GPS. These large displacements achieved by Iridium produce substantial changes in satellite line-of-sight geometry. Thus by augmenting GPS with Iridium, these substantial geometry changes can be exploited to estimate cycle ambiguities in real-time, allowing for precise carrier phase positioning.

Currently, Iridium can only broadcast via a single L-band frequency, centered at 1624 MHz [9]. A second, Ka-band frequency (23 GHz) is available [22], but it cannot be used continuously since the wavelength is low enough to be potentially affected by rain. The inconsistent availability of this second frequency means dual frequency capability for Iridium cannot be assumed.

In this work, it is assumed that Iridium signals are subject to the same error sources as GPS. This means both GPS and Iridium are influenced by the error source which has yet to be discussed, namely the ionosphere. An explanation of the ionosphere, including the effect it has on signals and the introduction of the model to account for the errors it produces is the focus of the next chapter.

## CHAPTER 3

### THE IONOSPHERE

The ionosphere is a region of the Earth's atmosphere extending from 50 km to 1000 km of altitude. This region contains gases that become ionized by solar radiation, creating free electrons which move throughout the ionosphere. The flux of these free electrons causes the ionosphere to be divided into four layers. These layers are distinguished by their ability to retain free electrons. Figure 3.1 shows the range of altitudes each layer of the ionosphere encompasses [12] (indicated by dashed lines). In addition, the figure depicts the general profile of the relative electron density as a function of altitude within the ionosphere. The relative electron density increases with altitude until 350 km (thick line) and then decreases as the upper altitudes of the ionosphere are reached.

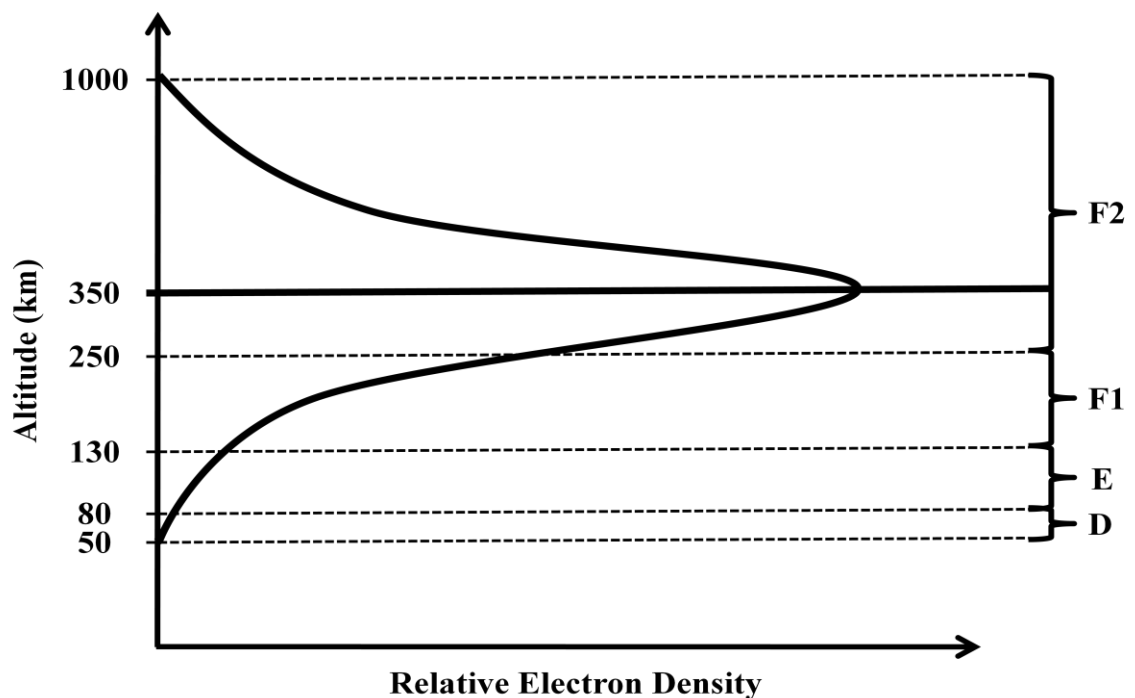


Figure 3.1. Relative Electron Density Profile with Layers of the Ionosphere

### **3.1 Effects on Signals**

**3.1.1 Global Effects.** Ionospheric effects are sensitive to the time of day, season, location, and place in the eleven-year long solar cycles. All of these aspects are related to solar exposure.

As the sun heats up the ionosphere, it causes electron concentrations to change. Over the course of a day, the electron concentration can change by one to two orders of magnitude [26]. During nighttime hours, the impact of both the D and F1 layers of the ionosphere disappears completely. The effect of the E layer also decreases as the night progresses until it becomes negligible. The influence of the F2 layer remains throughout the night, but it continually declines until a minimum is reached just before sunrise [33].

The ionosphere's effects vary depending on upon location. Low, mid, and high latitude locations must contend with unique events particular to each latitude zone, which are influenced by solar radiation [33].

The solar cycle, or the periodic variation in solar activity, also influences the ionosphere. During more active periods of a cycle, the ionosphere becomes more disturbed which introduces more variability into the errors that can be experienced by satellite signals.

Throughout the rest of this work, the daily, seasonal, location, and solar cycle effects will be referred to as global effects. These influence the localized effects described below.

**3.1.2 Localized Effects.** Due to spatially varying electron concentrations within the ionosphere, a random variation in the signal's amplitude and phase can occur. This process is known as scintillation. Scintillation is more prevalent and pronounced in the F2

layer at altitudes between 250 km and 400 km. The largest variations in electron concentration are found at these altitudes. Scintillation causes signals to be delayed and is influenced by electrons and ions which make up only 0.4% of the total atmospheric matter for a particular altitude within the ionosphere [33].

The F2 layer contains the highest electron density, persists throughout the night hours, and is the layer where the most scintillation occurs. Consequently, in this work, the total effect of the ionosphere on signals will be assumed to be concentrated within the F2 layer.

Other difficult to predict ionospheric phenomena include Traveling Ionospheric Disturbances, or TIDs. TIDs can be described as local, short term variations in the density of the electrons within the ionosphere [1, 27]. These density fluctuations are most commonly found within the F1 and F2 layers. These variations manifest themselves in the form of waves which move throughout the ionosphere with a wide range of frequencies and velocities. The two most common forms of TIDs are known as large scale and medium scale.

The mechanisms that cause TIDs are still being investigated, but most researchers point to a link with atmospheric gravity waves (AGW) [16]. AGWs are waves present in the thermosphere, a neutral layer of the atmosphere above altitudes of around 85 km. The thermosphere overlaps with lower layers of the ionosphere. This leads to collisions between the neutral particles of the thermosphere and the ionized particles of the ionosphere. These collisions produce waves at ionospheric altitudes. AGWs are thought to originate from meteorological events, such as eclipses, neutral winds, or the solar

terminator (the imaginary line that divides the day side of the earth from the night side) [7].

Previous work has shown that large scale TIDs, or LSTIDs, usually exhibit wavelengths between 600 km and 2000 km, while medium scale TIDs, or MSTIDs, have wavelengths in the range of 100 km to 500 km [7]. LSTIDs exhibit a period greater than one hour and a horizontal velocity faster than 0.3 km/s. For MSTIDs, a period of ten minutes to one hour and a horizontal velocity ranging from 0.05 km/s to 0.3 km/s is typical. It has been found that MSTIDs occur most often during the daytime in the local winter and during the night in the local summer [16].

In this work, the global and localized effects of the ionosphere discussed above will be referred to as nominal effects since these are encountered most consistently. Only nominal effects will be considered in this work.

**3.1.3 Ionospheric Storms.** Ionospheric storms impact signals propagating through the ionosphere. These storms result from solar flares which can disrupt communication with satellites for locations on the daytime side of the earth. This disruption occurs because of increased electron densities in the D and E layers of the ionosphere. Storms can last for many days and can affect large areas [33]. Due to the unpredictable behavior of ionospheric storms, these are not considered to be nominal effects. Therefore, storms are a subject for investigation in future work.

## **3.2 Classifying Ionospheric Activity**

The ionosphere is sensitive to many factors, including solar activity. Variations in solar activity cause the ionosphere to behave differently and affect the extent to which satellite signals are impacted. To distinguish levels of solar activity, geomagnetic indices

have been developed. The K and A indices are two prominent geomagnetic scales in use today. For the mid-latitude region of the United States, these indices are generated at the National Weather Service/Space Weather Prediction Center facilities in Boulder, Colorado and Fredericksburg, Virginia. These indices classify the ionosphere as being in one of seven states: quiet, unsettled, active, minor storm, major storm, severe storm, or very major storm.

An overview of the K and A indices is given below, but more detailed information can be found in [25, 33].

**3.2.1 K Index Scale.** K index readings are taken every three hours throughout the course of a day. The three hour interval is large enough to detect a disturbance which lasts for a few hours, but it is short enough not to affect the overall classification for the day [25].

The K values provide an indication of the variation in the magnetic field resulting from solar wind. These take on logarithmically-scaled integer values between zero and nine.

Derived from the K index is the standardized,  $K_s$ , index. This value is obtained by removing local and seasonal variations from the K readings. The standardized  $K_s$  index scale ranges from zero to nine, but is broken down into sub-levels. There are 28 sub-levels:  $0_0, 0_+, 1_-, 1_0, 1_+, \dots, 9_-, 9_0$ . A planetary K index,  $K_p$ , is derived from the standardized indices obtained at 12 worldwide stations located between geomagnetic latitudes of -42 and 63 degrees [33]. The  $K_p$  index is a daily (24-hour) value. This daily value must be computed from the standardized index instead of the individual K values

collected throughout the day. This is because these  $K$  values cannot be linearly averaged since quasi-logarithmic operations are used to generate them [25].

**3.2.2 A Index Scale.** This scale is a result of the conversion of the  $K$  index readings to an approximately linear scale [33]. Converting the  $K$  index value from each three hour segment into this linear scale leads to an index called the  $a_K$ . In a similar fashion, the  $a_P$  index follows from the conversion of the  $K_P$  index. The daily average of the  $a_K$  indices computed from each three hour segment at a particular site produces a daily single station index,  $A_K$ . The averaging of the daily single station indices obtained at each of the 12 worldwide stations produces a daily planetary value,  $A_P$ .

Table 3.1 below gives the relationship between the daily single station index  $A_K$  and the various types of ionospheric activity [33]. The daily single station index  $A_K$  is shown since this value will be used in the data processing to distinguish the ionospheric activity present at various locations over many days within the United States. The  $A_K$  indices from Fredericksburg, Virginia will be used in the data analysis to distinguish between days exhibiting the various types of ionospheric activity.

Table 3.1. Relationship between Daily Single Station Index  $A_K$  and Ionospheric Activity

$A_K$ Index	Type of Activity
0	Quiet
2	Quiet
3	Quiet
4	Quiet to Unsettled
7	Unsettled
15	Active
27	Active
48	Minor Storm
80	Major Storm
132	Severe Storm
208	Very Major Storm
400	Very Major Storm

### 3.3 Ionospheric Activity Breakdown

It is important to have an idea of the frequency of occurrence for each of the ionospheric states. This will be useful information when validating the error model since a baseline for how often to expect each state will be established.

To establish this baseline, data from the Space Weather Prediction Center (SWPC) is processed. The SWPC provides archived  $A_K$  and K index data collected at the National Weather Service/SWPC facility located in Fredericksburg, Virginia. Data from 1997 to 2007 is gathered and processed based on the ranges of  $A_K$  values presented in Table 3.1. Table 3.2 shows the percentage of occurrence of the various ionospheric states for each year during this ten year span.

Table 3.2. Ionospheric Activity Breakdown by Year

Year	Quiet	Unsettled	Active	Minor Storm	Major Storm	Severe Storm	Very Major Storm
1997	24.657	61.369	13.698	0.273	0.00	0.00	0.00
1998	29.041	57.534	11.781	0.548	0.274	0.00	0.00
1999	25.205	56.438	18.082	0.00	0.00	0.00	0.00
2000	20.218	58.196	20.218	0.546	0.00	0.273	0.00
2001	22.191	64.383	12.328	0.821	0.274	0.00	0.00
2002	21.643	64.383	13.151	0.274	0.00	0.00	0.00
2003	9.863	51.232	37.260	0.822	0.00	0.548	0.00
2004	26.775	59.836	12.295	0.273	0.819	0.00	0.00
2005	32.602	51.232	15.616	0.548	0.00	0.00	0.00
2006	51.506	39.726	8.493	0.274	0.00	0.00	0.00
2007	52.328	42.465	5.205	0.00	0.00	0.00	0.00

Years 1997-2000 are at the end of an eleven-year solar cycle. Therefore, the number of unsettled and active days is increasing until the solar maximum is reached during years 2001-2003. This explains the larger percentage of active and stormy days during this period. Years from 2004 onward show a decrease in the percentage of

unsettled days and an increase in quiet days. This trend indicates that these years are in between two solar maximums. The next solar maximum is expected to occur around 2012.

In addition, all 3,652 days (when taking into account leap years) over this ten year period are broken down according to  $A_K$  values. This will help to document how often the various states occur on a day-to-day basis. Table 3.3 provides the results from considering all of the days throughout the ten year span.

Table 3.3. Ionospheric Activity for Days Between 1997 and 2007

Ionospheric Activity	$A_K$ Index Range	Percentage Of Days With Activity
Quiet	0 – 4	28.727
Unsettled	5 – 14	55.165
Active	15 – 47	15.285
Minor Storm	48 – 79	0.398
Major Storm	80 – 131	0.124
Severe Storm	132 – 207	0.074
Very Major Storm	208 – 400	0.000

The results of Table 3.3 point to the fact that quiet, unsettled, and active days should be the main focus for the purposes of evaluating the ionospheric error model, which will be presented shortly, since these states occur 99.2% of the time. Naturally, stormy days should be investigated in future work once the model can be shown to work well with quiet, unsettled, and active days.

### 3.4 Nominal Ionospheric Error Model

The nominal form of the ionosphere error model, which serves as a starting point for this work, has been derived in [20-22]. It is based upon three assumptions, which are shown in figure 3.2. This figure is a top view of the earth-sun system. The ionosphere is

depicted as being elongated toward the sun in order to represent the variations in electron density present within this region.

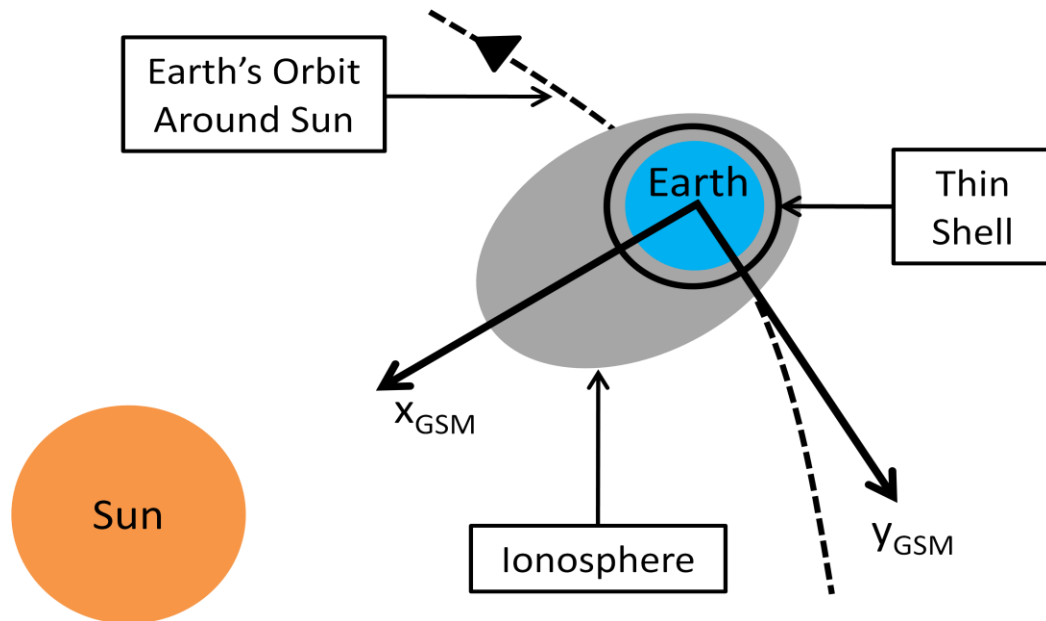


Figure 3.2. Top View of Earth-Sun System with Error Model Assumptions

First, the global effects of the ionosphere (section 3.1.1) are assumed to be constant when considered in a Geocentric Solar Magnetospheric (GSM) coordinate frame over a limited time interval. A GSM coordinate frame is one where the positive x-axis points toward the sun, the positive z-axis points in the same direction as the northern magnetic pole, and the y-axis is perpendicular to the earth's magnetic dipole [25]. The positive y-axis is defined to point toward dusk, in the opposite direction the earth is traveling in its orbit. This type of coordinate frame is favored when studying the ionosphere since it is connected to both the sun and the Earth's magnetic field, both of which influence the ionosphere.

Second, the ionosphere is approximated to be a thin shell around the Earth at a mean height of 350 km. This height is chosen since it lies within the F2 region of the ionosphere where most of the ionospheric effects (scintillation, TIDs) are introduced. The

thin shell approximation means that the effects of the ionosphere are concentrated at the ionospheric pierce point, or IPP. The IPP is the intersection of the thin shell with the line-of-sight vector (LOS) between a receiver close to the surface of the earth and the satellite [26]. IPP motion is the product of the movement of the earth, the user, and the satellite.

Lastly, the vertical ionospheric delay affecting a satellite signal is assumed to vary linearly with IPP displacement ( $d_{IPP}$ ) up to a certain limit. As stated in chapter 1, the vertical delay is the delay experienced by a signal penetrating the ionosphere perpendicularly. IPP displacements are measured in terms of great circle distance in a GSM reference frame. The great circle distance is defined as the shortest distance between two points on the surface of a sphere without going through the inner portions of the sphere. In this work, IPP displacements are measured in kilometers. This linearity limit will be determined using experimental data in chapter 5.

Variations in the ionospheric delay at the L1 frequency over time can be estimated using the error model and measured using dual-frequency satellite measurements. The delay is related to the total electron content (TEC). TEC is defined as the number of electrons inside a  $1 \text{ m}^2$  cross section of a tube extending from the satellite to the user receiver. In addition, the delay is inversely proportional to the square of the carrier frequency [26]. This relationship between TEC and frequency is used to compute the delay on the L1 frequency using dual frequency measurements [21, 26]. For this reason, dual frequency data will be employed to evaluate the model. The method for computing the delay at the L1 frequency from dual frequency measurements will be presented in the next chapter.

**3.4.1 Error Model Equation.** The ionospheric error model developed in [20-22] is shown in equation 3.1. It follows from the three assumptions discussed previously.

$$\epsilon_{I,k} = c_{OB,k}(b_{VI} + d_{IPP,k} \cdot g_{VI}) \quad (3.1)$$

where:

$c_{OB,k}$  : obliquity factor

$b_{VI}$  : vertical ionospheric bias

$d_{IPP,k}$  : ionospheric pierce point displacement (measured as a great circle distance)

$g_{VI}$  : vertical ionospheric gradient

Throughout the rest of this work, the model given in equation 3.1 will be referred to as the original, or nominal, model. It is to be noted that the model of equation 3.1 only contains two terms,  $b_{VI}$  and  $g_{VI}$ , which need to be estimated. This is because the model avoids unnecessary complexity in order to reduce the amount of uncertainty introduced to the positioning solution which can decrease system availability (discussed in chapter 1).

Although the error model in equation 3.1 is linear with respect to the vertical ionospheric delay, it is misleading to call it a linear model because the delay is modulated by the obliquity factor, which is a function of satellite elevation angle. This model assumes that the ionospheric pierce point follows a path described by the great circle while exhibiting minimal lateral motion [22]. The terms in this error model are explained below.

**3.4.2 Error Model Parameters.** The ionosphere first causes an initial uncertainty in the signal when it is acquired by the receiver. This uncertainty cannot be accurately captured by existing GPS ionosphere models or corrections. For real time carrier phase positioning, this initial uncertainty needs to be precisely known or conservatively

accounted for. The vertical ionospheric bias term,  $b_{VI}$ , in the error model accounts for this uncertainty. Variations in this initial uncertainty over a given sampling period must also be included in the model. These variations are modeled as a ramp with a constant slope over a given sampling period known as the vertical ionospheric gradient, or  $g_{VI}$ .

Figure 3.3 graphically depicts how the  $b_{VI}$  and  $g_{VI}$  terms are used to capture ionospheric errors with the model. The vertical ionospheric bias,  $b_{VI}$ , is the initial uncertainty (y-intercept), and the slope of the ramp over the pierce point displacement  $d_{IPP}$  which accounts for variations in the initial uncertainty is the vertical ionospheric gradient,  $g_{VI}$ .

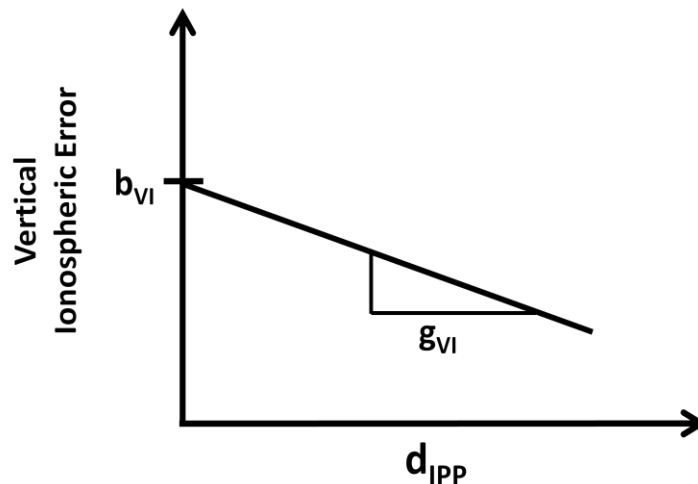


Figure 3.3. Bias and Gradient Modeling of Ionospheric Errors

Approximating the ionosphere as a thin shell means that satellite signals will have varying path lengths through the ionosphere. The path length depends on the satellite's elevation angle. A scaling factor must be introduced to account for this elevation dependency [22]. The scaling quantity is known as the obliquity factor,  $c_{OB,k}$ , and it is computed as follows:

$$c_{OB,k} = \left[ 1 - \left( \frac{R_E}{R_E + h_I} \right)^2 \cos^2 \theta_k \right]^{-\frac{1}{2}} \quad (3.2)$$

where:

$R_E$  : radius of the earth (6378.1383 km)

$h_I$  : ionospheric shell height (350 km)

$\theta_k$  : satellite elevation angle

The obliquity factor ranges from a value of one at zenith (directly overhead) to a value of about three at five degrees of elevation.

Modeling the ionospheric effects as a bias and gradient allows the model to be used with WAAS corrections. WAAS corrections are provided in terms of a bias, but this estimate contains some error. This error is due to the interpolation that must be done to convert the ionospheric delay at the IGP into a delay at the satellite IPP for the user location [31]. The initial error in the bias estimate as well as the variations of this estimate over a given sampling period must be captured. This means WAAS corrections can be applied and the error model can account for the error in the bias estimate and the variation of the estimate over time.

In order to improve the integrity of the error model, the  $b_{VI}$  and  $g_{VI}$  terms must be determined on a per satellite basis. Due to the large separations between satellites as well as the spatial and temporal variability of the ionosphere, each satellite will be affected differently. Since the model is applied over limited IPP displacements, which are not large enough to overlap IPPs from other satellites, determining a single bias and gradient for a section of the ionosphere is unrealistic. Analysis on a per satellite basis allows for the errors to be more conservatively accounted for, which leads to higher integrity for the model.

### 3.5 Using the Nominal Ionospheric Error Model with iGPS

The ionospheric error model has been introduced and its parameters explained. Now, an explanation on how the model is used in the context of iGPS will be given. First, the model must be evaluated. This is done using dual frequency carrier phase measurements (the procedure for evaluating the model will be shown in chapter 4). The purpose of the model evaluation is to determine prior knowledge on the  $b_{VI}$  and  $g_{VI}$  states as well as to establish how well the model fits the data. This model evaluation, which requires the application of the model to large amounts of data to ensure the results are statistically significant, is performed in this work.

The prior knowledge obtained from this model evaluation is then used for iGPS single frequency carrier phase positioning. These carrier phase observations, as described in [20-22], have the form (shown for time epoch  $k$ ):

$$\phi_k = -\mathbf{e}_k^T \mathbf{x}_k + \tau_k + N + \epsilon_{E,k} + \epsilon_{T,k} - \epsilon_{I,k} + \nu_k \quad (3.3)$$

where:

$\mathbf{e}_k^T$  : line-of-sight vector between satellite and user

$\mathbf{x}_k$  : user position vector

$\tau_k$  : user clock offset

$N$  : cycle ambiguity

$\epsilon_{E,k}$  : orbit ephemeris and satellite clock error

$\epsilon_{T,k}$  : tropospheric error

$\epsilon_{I,k}$  : ionospheric error

$\nu_k$  : measurement noise (includes receiver noise and multipath)

Single frequency measurements provide no information about the ionosphere which could distinguish it from other error sources. In addition, ionospheric effects are unpredictable and dynamic in nature. This means that the error model must be utilized to account for ionospheric effects in the single frequency observations in order to improve positioning accuracy.

The ionospheric error model given by equation 3.1 is substituted for the ionospheric error term,  $\epsilon_{I,k}$ , in equation 3.3. Moreover, the orbit ephemeris and satellite clock error ( $\epsilon_{E,k}$ ) and the tropospheric error ( $\epsilon_{T,k}$ ) have models similar in form to that of the ionospheric model [21]. These models are also substituted in equation 3.3 for the appropriate error sources. This means that the parameters in these models must be estimated along with those in the ionospheric error model, the user position and clock bias, and the cycle ambiguity (While the error model parameters are estimated, the goal is not to obtain precise estimates of these states, but rather to use the uncertainty in these parameters determined from the model evaluation to aid in capturing each error's behavior over time.). As mentioned in chapter 1, since overall navigation system availability decreases as the number of parameters in the estimation algorithm increases, the error models must be described with as few parameters as possible.

Precise position estimation using carrier phase observations is carried out in a separate analysis which is beyond the scope of this work. As discussed earlier, the purpose of this work is to evaluate the error model. Before the evaluation can be performed, the tools needed for this analysis must be introduced. These tools will be laid out in the next chapter.

## CHAPTER 4

### METHODOLOGY FOR EXPERIMENTAL EVALUATION OF THE ERROR MODEL

Evaluation of the ionospheric error model requires collecting, processing, and analyzing experimental data. The steps needed to collect and process the data for analysis are discussed below.

#### **4.1 Database and Other Sources of Information**

Various sources are utilized to obtain the required data and information for evaluating the model. Constants needed in the analysis, such as the precise wavelengths of the L1 and L2 frequencies, are taken from the Interface Control Document (ICD-GPS-200C) [18].

**4.1.1 Dual Frequency GPS Carrier Phase Data.** In this work, dual frequency carrier phase measurements are exploited to compute the ionospheric delay at the L1 frequency. Archived carrier phase measurements collected at multiple locations over more than a decade are available from the Continuously Operating Reference Stations (CORS) database [4]. CORS is a network of worldwide ground stations run by the National Geodetic Survey (NGS). These stations collect GPS code and carrier phase data and make it accessible to the public.

As part of the precautions taken when selecting a CORS site for this analysis, photographs of the antenna location, obtainable from the CORS database, are inspected to guarantee that the antenna is in full view of the sky. Ensuring that this criterion is met minimizes unwanted effects from multipath. The selected sites are based all across the United States in order to provide geographic diversity.

**4.1.2 Low Earth Orbit Data.** Two types of low earth orbit data are used in this work: simulated Iridium line-of-sight data and actual satellite data. Simulated ionospheric delays on Iridium line-of-sights are provided by Dr. Seebany Datta-Barua of the Atmospheric and Space Technology Research Associates. The actual LEO data is generated by Trevor Garner from the Applied Research Laboratory, the University of Texas at Austin, and has been obtained through Dr. Datta-Barua.

**4.1.3 Satellite Almanacs.** Almanacs consist of seven parameters broadcast by each satellite in the GPS constellation. These parameters provide information on the health of the satellite and orbital data used to predict when the satellite will be in view. Data in the almanacs are valid over the course of a day, and are coarser versions of the data transmitted in the ephemeris that is updated every two hours. The almanacs' role in this work is to aid in generating satellite azimuth and elevation angles. These are used to compute the latitude and longitude of the ionospheric pierce point (IPP). Almanacs are obtained from the U.S. Coast Guard Navigation Center (NAVCEN) [11].

**4.1.4 Ionospheric Pierce Point Latitude and Longitude.** Using the azimuth and elevation angles generated from the almanacs, the ionospheric pierce point latitude and longitude can be determined. These are used to compute the IPP displacement,  $d_{IPP}$ , in a GSM reference frame. The IPP displacement multiplies the vertical ionospheric gradient ( $g_{VI}$ ) in the error model (equation 3.1). Guidelines for determining IPP latitude and longitude are found in the WAAS Minimum Operational Performance Standards (MOPS) document [31].

## 4.2 Method of Data Processing

There are different ways of processing dual-frequency measurements to evaluate ionospheric delays. These methods are presented in [24]. A variant of one of these methods, known as the time-step method, is employed in this work.

**4.2.1 Modified Time-Step Method.** The original time-step method pairs a single reference station and satellite. Differences in ionospheric delays over predefined time intervals determine the ionospheric gradients. The gradient is equal to the delay difference divided by the time interval (if a gradient over time is desired) or by the IPP displacement  $d_{IPP}$  over this interval (to obtain the gradient of interest,  $g_{VI}$ ). This means that the gradient can be computed for a range of IPP displacements simply by adjusting the time interval.

There are constraints with the original time-step method, the most notable being related to changes in satellite geometry. Over short time intervals, the time-step method is applicable because the obliquity factor is assumed constant [24]. If the change in obliquity is negligible, the ionospheric bias does not impact the gradient estimation.

To avoid the satellite geometry constraint, a variation of the time-step method is used in this work. This modified method accounts for changes in the obliquity factor over longer time intervals by considering an ionospheric bias parameter along with the gradient. Greater IPP displacements can be evaluated with this modified approach since satellite geometry changes are taken into account.

**4.2.2 Sampling Interval Selection.** An appropriate sampling interval between measurement epochs must be determined. In order to maximize the amount of data

available for processing, a sampling interval of 30 seconds is chosen. This is the amount of time between measurement epochs in the data provided by CORS.

This sampling interval is short enough that GPS observations cannot be considered to be independent because of the measurement error time correlation due to multipath. Since GPS satellites are in medium earth orbit (MEO), to a user on earth the space vehicles appear to be moving very slowly. This slow movement means a sufficient amount of time (a few minutes in some cases) is needed for the multipath reflections to change and reduce the correlation of measurements. In order to use a 30 second sampling interval, this time correlation must be taken into account when evaluating the model.

For LEO data that will be investigated in chapter 7, a 30 second sampling interval does not lead to problems with multipath time correlation. LEO satellites move much faster, as viewed from the ground, and generate large displacements over a short period of time. The fast motion of the spacecraft changes the multipath environment very quickly. This means the multipath time constant will be small and the time correlation between measurements will be negligible.

### **4.3 Mathematical Formulation for Nominal Model Evaluation**

It is important to remember the objectives for the model evaluation. First, residual errors after applying the model to the data need to be quantified. Both mis-modeling errors and measurement noise contribute to these residual errors. Secondly, sample distributions of  $b_{VI}$  and  $g_{VI}$  need to be obtained. Certain statistics from these sample distributions, most notably standard deviation, will be used in the iGPS positioning algorithms of [20-22].

**4.3.1 Least-Squares Batch Estimation Algorithm.** To achieve the objectives described above, a weighted least squares estimation scheme will be used. This algorithm requires linear equations of the form:

$$\mathbf{z} = \mathbf{H}\mathbf{x} + \mathbf{v} \quad (4.1)$$

where  $\mathbf{H}$  is the observation matrix that relates the measurement vector,  $\mathbf{z}$ , to the state vector of quantities to be estimated,  $\mathbf{x}$ . Elements of the measurement noise vector,  $\mathbf{v}$ , are assumed to be normally distributed random variables with zero mean. If measurement errors are not independent, their correlation over time (due to multipath) will be accounted for in the off-diagonal terms of the measurement noise covariance matrix  $\mathbf{V}$ .

When the number of measurements exceeds the number of unknown states (assuming that individual measurement equations are linearly independent), the state vector can be estimated. The least-squares estimate of the state vector,  $\hat{\mathbf{x}}$ , is computed by:

$$\hat{\mathbf{x}} = (\mathbf{H}^T \mathbf{V}^{-1} \mathbf{H})^{-1} \mathbf{H}^T \mathbf{V}^{-1} \mathbf{z} \quad (4.2)$$

The least-squares state estimate is used in the computation of the residual vector,  $\mathbf{r}$ . This vector provides the difference between the true measurements and the estimated measurements. It is given by:

$$\mathbf{r} = \mathbf{z} - \mathbf{H}\hat{\mathbf{x}} \quad (4.3)$$

The state covariance matrix,  $\hat{\mathbf{P}}$ , is another metric that is generated in the computation of equation 4.2. This matrix provides an indication of the quality of the estimated state vector. The variances for the states are found on the diagonal of the state covariance matrix,  $\hat{\mathbf{P}}$ . For example, the covariance for the first state in the state vector will be in the first row and first column of the covariance matrix,  $\hat{\mathbf{P}}$ . Small diagonal terms

in  $\hat{\mathbf{P}}$  means the estimated values are close to actual parameter values with high probability. The state covariance matrix is computed from:

$$\hat{\mathbf{P}} = (\mathbf{H}^T \mathbf{V}^{-1} \mathbf{H})^{-1} \quad (4.4)$$

Now that the general estimation procedure has been laid out, it will be shown how to incorporate it into this work.

### 4.3.2 Computing the Ionospheric Delay from Dual-Frequency Measurements.

Dual frequency measurements offer the ability to compute the delay caused by the ionosphere at the L1 frequency. As mentioned in the previous chapter, this delay is related to the total electron content (TEC) and is inversely proportional to the square of the carrier frequency. Using these relationships, the ionospheric delays at the L1 and L2 frequencies,  $I_{L1}$  and  $I_{L2}$ , can be written as [26]:

$$I_{L1,k} = -\frac{1}{f_{L1}^2} \cdot A_k \quad (4.5)$$

$$I_{L2,k} = -\frac{1}{f_{L2}^2} \cdot A_k \quad (4.6)$$

where:

$$A_k = 40.3 \cdot TEC_k \quad (4.7)$$

Consider the carrier phase ranging measurements at the L1 and L2 frequencies for epoch  $k$ :

$$\lambda_{L1} \phi_{L1,k} = r_k + c\delta t_{u,k} - c\delta t_k^s + \lambda_{L1} N_{L1} - I_{L1,k} + T_k + E_k + \epsilon_{\phi_{L1,k}} \quad (4.8)$$

$$\lambda_{L2} \phi_{L2,k} = r_k + c\delta t_{u,k} - c\delta t_k^s + \lambda_{L2} N_{L2} - I_{L2,k} + T_k + E_k + \epsilon_{\phi_{L2,k}} \quad (4.9)$$

The wavelengths of the L1 and L2 frequencies,  $\lambda_{L1}$  and  $\lambda_{L2}$ , as well as all other terms in these equations are defined in equations 2.1 and 2.2.

As long as lock is maintained with a satellite, the cycle ambiguity bias,  $N$ , (and other terms such as inter-frequency biases which can be incorporated into the cycle ambiguity bias) will be constant.

The subscript  $k$  indicates that L1 and L2 measurements are considered at the same time epoch  $k$ . These measurements are also collected for a common satellite-receiver pair. Therefore, the range, receiver clock bias, satellite clock and orbit ephemeris errors, and tropospheric error will be the same for both L1 and L2 measurements. Subtracting 4.9 from 4.8 cancels out the range,  $r_k$ , the receiver clock bias,  $c\delta t_{u,k}$ , the satellite clock and orbit ephemeris errors ( $c\delta t_k^S$  and  $E_k$ ), and the tropospheric error,  $T_k$ , to yield:

$$\begin{aligned} (\lambda_{L1}\phi_{L1,k} - \lambda_{L2}\phi_{L2,k}) &= (\lambda_{L1}N_{L1} - \lambda_{L2}N_{L2}) + (\epsilon_{\phi_{L1,k}} - \epsilon_{\phi_{L2,k}}) \\ &\quad - (I_{L1,k} - I_{L2,k}) \end{aligned} \quad (4.10)$$

To reduce the number of variables on the right hand side of equation 4.10, the following variables are defined:

$$b' = (\lambda_{L1}N_{L1} - \lambda_{L2}N_{L2})$$

$$v_k' = (\epsilon_{\phi_{L1,k}} - \epsilon_{\phi_{L2,k}})$$

As shown above, the variable,  $b'$ , is defined in terms of the cycle ambiguity bias, but smaller magnitude inter-frequency biases can also be present within this term. For this reason,  $b'$  will be called the cycle ambiguity and inter-frequency bias. The single-difference L1-L2 carrier phase measurement noise,  $v_k'$ , is a normally distributed random variable, which is correlated in time due to multipath.

As a result of the previous definitions, 4.10 now becomes:

$$(\lambda_{L1}\phi_{L1,k} - \lambda_{L2}\phi_{L2,k}) = b' + v_k' - (I_{L1} - I_{L2}) \quad (4.11)$$

Substituting 4.5 and 4.6 into last term on the right hand side of 4.11 produces:

$$(\lambda_{L1}\phi_{L1,k} - \lambda_{L2}\phi_{L2,k}) = b' + \nu_k' + A_k \left( \frac{1}{f_{L1}^2} - \frac{1}{f_{L2}^2} \right) \quad (4.12)$$

The equivalent delay at the L1 frequency, as given in equation 4.5, needs to be isolated on the right hand side of 4.12. In order to do this, all terms in 4.12 are multiplied by a coefficient,  $f_p$ , which is given as:

$$f_p = -\frac{1}{f_{L1}^2} / \left( \frac{1}{f_{L1}^2} - \frac{1}{f_{L2}^2} \right) = \left( \frac{f_{L2}^2}{f_{L1}^2 - f_{L2}^2} \right) \quad (4.13)$$

Using this coefficient, equation 4.12 can now be written as:

$$f_p \cdot (\lambda_{L1}\phi_{L1,k} - \lambda_{L2}\phi_{L2,k}) = f_p \cdot b' + f_p \cdot \nu_k' - \frac{1}{f_{L1}^2} \cdot A_k \quad (4.14)$$

The last term on the right hand side of equation 4.14 ( $-1/f_{L1}^2 \cdot A_k$ ) is the L1 ionospheric delay,  $I_{L1}$ . It has the same form as equation 4.5. The inter-frequency and cycle ambiguity bias term,  $b'$ , and the measurement noise,  $\nu_k'$ , are still present in equation 4.14. Therefore, the measurement of the delay is both biased and noisy.

In order to fit the linear vertical ionospheric error model to data collected over successive epochs, the ionospheric delay term,  $I_{L1}$ , can be substituted for the error model of equation 3.1. As a result of this substitution, 4.14 becomes:

$$f_p \cdot (\lambda_{L1}\phi_{L1,k} - \lambda_{L2}\phi_{L2,k}) = c_{OB,k}(b_{VI} + d_{IPP,k} \cdot g_{VI}) + f_p \cdot b' + f_p \cdot \nu_k' \quad (4.15)$$

Equation 4.14 is in the form of 4.1. This means it is a linear equation with respect to the three quantities to be estimated, namely  $b_{VI}$ ,  $g_{VI}$ , and the nuisance bias parameter,  $b'$ .

Estimation of  $b_{VI}$ ,  $g_{VI}$ , and  $b'$  requires observability on these states.

Observability can be interpreted as a level of independence between columns of the observation matrix,  $\mathbf{H}$ . It is provided by differences in variations of the coefficients

multiplying the three states over the sampling period. For these coefficients to change, a change in satellite geometry is required.

**4.3.3 Equations for Model Evaluation.** Measurements collected over the sampling period are stacked together in a vector so that equation 4.15 can be written in matrix form (in the same form as equation 4.1) as:

$$\begin{bmatrix} z_1 \\ \vdots \\ z_n \end{bmatrix} = \begin{bmatrix} c_{OB,1} & c_{OB,1} \cdot d_{IPP,1} & 1 \\ \vdots & \vdots & \vdots \\ c_{OB,n} & c_{OB,n} \cdot d_{IPP,n} & 1 \end{bmatrix} \begin{bmatrix} b_{VI} \\ g_{VI} \\ b \end{bmatrix} + \begin{bmatrix} v_1 \\ \vdots \\ v_n \end{bmatrix} \quad (4.16)$$

where:

$$z_k = f_p \cdot (\lambda_{L1} \phi_{L1,k} - \lambda_{L2} \phi_{L2,k})$$

For notational purposes in equation 4.16 and throughout the rest of this work, the following variables are used:

$$b = f_p \cdot b'$$

$$v_k = f_p \cdot v_k'$$

The carrier phase measurement noise,  $v_k$ , is a time-correlated normally distributed random variable with zero mean. Considering the effect of multipath (M) and receiver noise (RN) to be the same on both the L1 and L2 measurements, the measurement noise is given by [21]:

$$v_k = \sqrt{2} \cdot f_p (\epsilon_{M-\phi,k} + \epsilon_{RN-\phi,k})$$

The  $\epsilon_{M-\phi,k}$  and  $\epsilon_{RN-\phi,k}$  terms are normally distributed random variables with zero mean and variances of  $\sigma_{M-\phi}^2$  and  $\sigma_{RN-\phi}^2$ . Assuming that  $\sigma_{M-\phi}^2$  is one centimeter and  $\sigma_{RN-\phi}^2$  is 0.3 cm, which are commonly used values for these parameters that have been employed in previous work [20-22], the carrier phase measurement noise has an expected standard deviation of 2.3 cm.

In this analysis, the size of  $\mathbf{z}$ ,  $\mathbf{H}$ , and  $\mathbf{v}$  depends upon the time it takes to achieve the desired IPP displacement. The system of equations in 4.16 will now be referred to as:

$$\mathbf{z}_{Meas} = \mathbf{H}_{Meas}\mathbf{x} + \mathbf{v}_{Meas} \quad (4.17)$$

Some prior knowledge on the state vector is also available from [20-22]. This prior knowledge is provided through a best guess value of the state and a predicted standard deviation of the state. Prior knowledge can be incorporated by augmenting the measurement vector with direct pseudo-observations of the states. This process is implemented for the  $b_{VI}$  and  $g_{VI}$  terms. Prior knowledge on these states is assumed in [20-22]. The unknown inter-frequency and cycle ambiguity bias term,  $b$ , can take any value, meaning that no a-priori knowledge is assumed.

Measurement vector augmentation helps to constrain the range of values a state can attain. It also aids in the problem of bias observability. There will be portions of data where the obliquity factor will be relatively constant. This causes difficulty in distinguishing between the vertical ionosphere bias term,  $b_{VI}$ , and the inter-frequency and cycle ambiguity bias term,  $b$ . The estimator will not be able to distinguish these two states if both are unconstrained, which can lead to unrealistic  $b_{VI}$  values.

The prior knowledge values for the bias and gradient are denoted as  $b_{VI,0}$  and  $g_{VI,0}$ . These values are provided with a variance indicating the expected range of variation that these states may have. The variances will be used in the weighting matrix which will be described shortly. Putting these augmented measurements in matrix form yields the system given by 4.18.

$$\begin{bmatrix} b_{VI,0} \\ g_{VI,0} \end{bmatrix} = \begin{bmatrix} 1 & 0 & 0 \\ 0 & 1 & 0 \end{bmatrix} \begin{bmatrix} b_{VI} \\ g_{VI} \\ b \end{bmatrix} + \begin{bmatrix} v_{b_{VI,0}} \\ v_{g_{VI,0}} \end{bmatrix} \quad (4.18)$$

This system of augmented measurements in 4.18 is defined as:

$$\mathbf{z}_{Aug} = \mathbf{H}_{Aug}\mathbf{x} + \mathbf{v}_{Aug} \quad (4.19)$$

Combining equations 4.17 and 4.19 results in the system of equations that will be used to evaluate the error model. This system has the form:

$$\mathbf{z} = \begin{bmatrix} \mathbf{z}_{Aug} \\ \mathbf{z}_{Meas} \end{bmatrix} = \begin{bmatrix} \mathbf{H}_{Aug} \\ \mathbf{H}_{Meas} \end{bmatrix} \mathbf{x} + \begin{bmatrix} \mathbf{v}_{Aug} \\ \mathbf{v}_{Meas} \end{bmatrix} = \mathbf{H}\mathbf{x} + \mathbf{v} \quad (4.20)$$

Using 4.20, the least-squares estimate of the state vector can be determined by employing 4.2, but before this computation can be executed, the weighting matrix must be introduced. The weighting matrix is defined as the inverse of the measurement noise covariance matrix. For the system of 4.20, the measurement noise covariance matrix is given as:

$$\mathbf{V} = \begin{bmatrix} \mathbf{V}_{Aug} & \mathbf{0} \\ \mathbf{0} & \mathbf{V}_{Meas} \end{bmatrix} \quad (4.21)$$

The  $\mathbf{V}_{Aug}$  matrix incorporates the variances of the initial guesses provided to the system and is realized as:

$$\mathbf{V}_{Aug} = \begin{bmatrix} \sigma_{b_{VI,0}}^2 & 0 \\ 0 & \sigma_{g_{VI,0}}^2 \end{bmatrix} \quad (4.22)$$

As mentioned earlier, when taking measurements every 30 seconds with GPS data, the time correlation due to multipath must be accounted for. This time correlation is captured in the off diagonal terms of the  $\mathbf{V}_{Meas}$  matrix. Modeling the multipath time correlation as a first order Gauss-Markov process, the  $\mathbf{V}_{Meas}$  matrix takes the form:

$$\mathbf{V}_{Meas} = \begin{bmatrix} \left(\frac{f_{L2}^2}{f_{L1}^2 - f_{L2}^2}\right)^2 \sigma_{\Delta\phi-M}^2 + \sigma_{\Delta\phi-RN}^2 & \cdots & \left(\frac{f_{L2}^2}{f_{L1}^2 - f_{L2}^2}\right)^2 \sigma_{\Delta\phi-M}^2 \cdot e^{-\Delta t(1-n)/T_M} \\ \vdots & \ddots & \vdots \\ \left(\frac{f_{L2}^2}{f_{L1}^2 - f_{L2}^2}\right)^2 \sigma_{\Delta\phi-M}^2 \cdot e^{-\Delta t(1-n)/T_M} & \cdots & \left(\frac{f_{L2}^2}{f_{L1}^2 - f_{L2}^2}\right)^2 \sigma_{\Delta\phi-M}^2 + \sigma_{\Delta\phi-RN}^2 \end{bmatrix} \quad (4.23)$$

where:

$\sigma_{\Delta\phi-M}^2$  : variance of the carrier phase multipath noise ( $\sqrt{2} \cdot 0.01$  m)

$\sigma_{\Delta\phi-RN}^2$  : variance of the carrier phase receiver noise ( $\sqrt{2} \cdot 0.003$  m)

$\Delta t$  : time between measurement epochs (30 Seconds)

$T_M$  : multipath time constant (60 Seconds)

Values used for  $\sigma_{\Delta\phi-M}^2$ ,  $\sigma_{\Delta\phi-RN}^2$ , and  $T_M$  are typical for these parameters, and have been implemented in previous work [20-22].

The components are now in place to evaluate the error model. The parameters in the model can be estimated and the residual errors after applying the model can be determined. Evaluation of the model is performed next.

## CHAPTER 5

## NOMINAL IONOSPHERE ERROR MODEL EVALUATION

The data used for the ionospheric error model evaluation has been collected from seven CORS sites across the United States between January and August of 2007. CORS sites used in this work are listed in table 5.1. The CORS designation and the location of the sites are shown in the table.

Table 5.1. CORS Sites used for Model Evaluation

CORS Site Designation	Site Location	Site Latitude (deg N)	Site Longitude (deg E)
mia3	Miami, Florida	25.78	-80.22
ohcd	Cleveland, Ohio	41.48	-81.67
miho	Holland, Michigan	42.79	-86.11
mibc	Battle Creek, Michigan	43.31	-86.20
zhu1	Houston, Texas	29.76	-95.38
slcu	Salt Lake City, Utah	40.75	-111.88
zla1	Los Angeles, California	34.05	-118.25

The year 2007 is chosen for its place within the eleven-year long solar cycle. It is between solar maxima, meaning that most days throughout this year are days of quiet ionospheric activity. This is evident in the results of table 3.3. Quiet ionospheric days ( $A_K$  index in the range 0-3) will be considered first since the ionospheric delay during these days is expected to be more predictable and easier to model than during unsettled and active ionospheric days. Unsettled and active days will be analyzed after quiet days.

### 5.1 Quiet Day Analysis

In this section, the original vertical delay ionosphere error model presented in chapter 3 (equation 3.1) is fitted to experimental data using the method described in chapter 4. The results presented throughout the rest of this chapter are generated using an

elevation mask of ten degrees. This means that the data from a satellite is used only if the satellite is above ten degrees elevation. The implementation of a mask helps to mitigate the effects of multipath which are more prevalent at low elevations.

To begin the analysis, values for the pseudo-observations (i.e., a-priori estimates) of parameters  $b_{VI}$  and  $g_{VI}$  in equation 4.18 must be defined. Table 5.2 contains the values used for the pseudo-measurements and the corresponding standard deviations used in the weighting matrix. Standard deviation values are set slightly higher than in the literature ([20-22]) because the final delay estimate should not completely rely on assumed prior knowledge.

Table 5.2. Values used for Measurement Vector Augmentation

State	Value of the State	Standard Deviation
$b_{VI}(\text{m})$	2	3
$g_{VI}(\text{m/km})$	0	$5 \times 10^{-3}$

**5.1.1 Determination of the Model's Linearity Limit.** One of the assumptions used in deriving the ionosphere error model is that the vertical ionospheric delay varies linearly with IPP displacements up to a certain limit. Before validating the model, this limit must be determined. Two criteria are considered below.

First, dual-frequency GPS data collected at the CORS sites listed in table 5.1 over several months are processed. Satellite passes are broken up into segments with varying maximum IPP displacements and the model is applied to each segment. The residuals from all of these segments are used to establish figure 5.1.

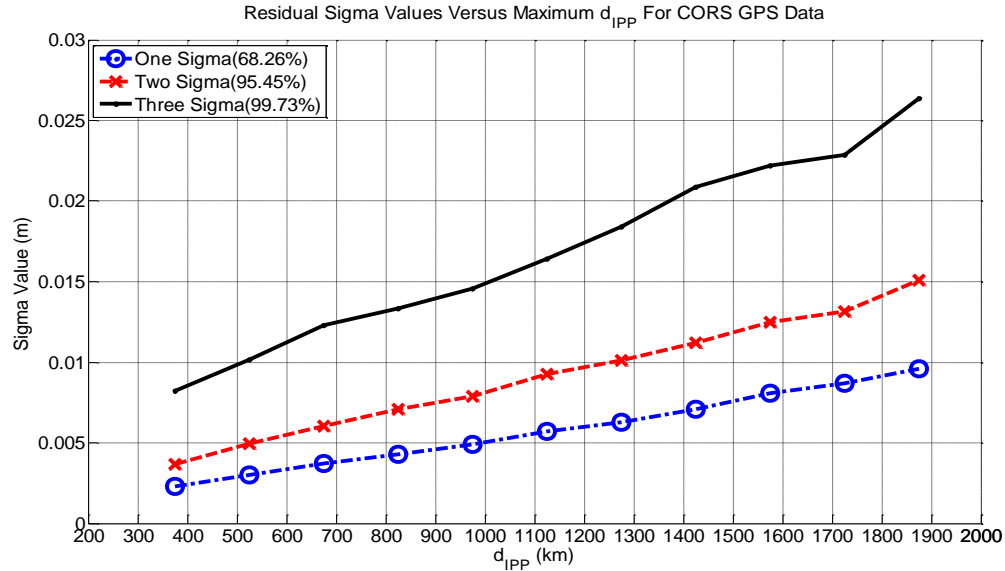


Figure 5.1. Analysis of Residual Errors for Determining Model’s Linearity Limit

Figure 5.1 shows normalized one, two, and three “sigma” curves for the residual distribution generated from this maximum IPP displacement analysis. The points which make up these curves are generated as follows: For a given maximum IPP displacement bin, the one “sigma” point corresponds to the range of residual values which encompass 68.26% of the total number of residuals contained within the displacement bin (assuming a zero-mean symmetric probability distribution of residuals). For instance, a point on the one “sigma” curve with a value of 0.01 means that residuals with values between -0.01 and 0.01 account for 68.26% of the total number of residuals for a given displacement bin. In the same way, values for the two and three “sigma” curves are generated by determining the range of residuals which contain 95.45% and 99.73% of the total number of residuals for a given displacement bin (higher percentiles will be considered later in this chapter).

For comparison with the one “sigma” curve, the two and three “sigma” curves are normalized. This is done by dividing the value corresponding to a 0.9545 confidence

level (two “sigma” value) by two, and the value corresponding to a 0.9973 confidence level (three “sigma” value) by three. Figure 5.1 shows that the residuals distribution is not Gaussian because the sigma curves (after scaling) do not lie on top of each other: the actual distribution has heavier tails than a Gaussian. The figure also shows that all sigma curves vary linearly with maximum IPP displacements in the range of 400km to 1900km.

The ionospheric error model can be roughly considered to match the data if the one, two, and three “sigma” values at the maximum IPP displacement limit where the vertical ionospheric delay varies linearly with respect to IPP displacement are smaller than the measurement noise standard deviation. In this work, the single difference (L1-L2) carrier phase measurement noise standard deviation is 1.4 cm, and these measurements are scaled by the factor  $f_p$  (equation 4.13) to measure the ionospheric delay on L1. This means the model is considered to match the data if the one-sigma value (as well as the two and three-sigma values) of the residuals is less than the measurement noise standard deviation of 2.3 cm. Figure 5.1 shows that all three residual sigma curves for maximum IPP displacements below 1500 km are under the 2.3 cm value.

The second criterion accounts for the impact of the linearity limit on the iGPS system. In previous work on the iGPS system [20-22], navigation system performance was measured in terms of availability of a high-integrity positioning solution. It was determined that nominal system availability (defined in chapter 1) decreases very rapidly for maximum IPP displacements below 600 km. Evidence of this decrease is shown by the curve in figure 5.2. This figure has been taken from [21] (courtesy of Mathieu Joerger) to show the impact of maximum IPP displacement on iGPS navigation system availability.

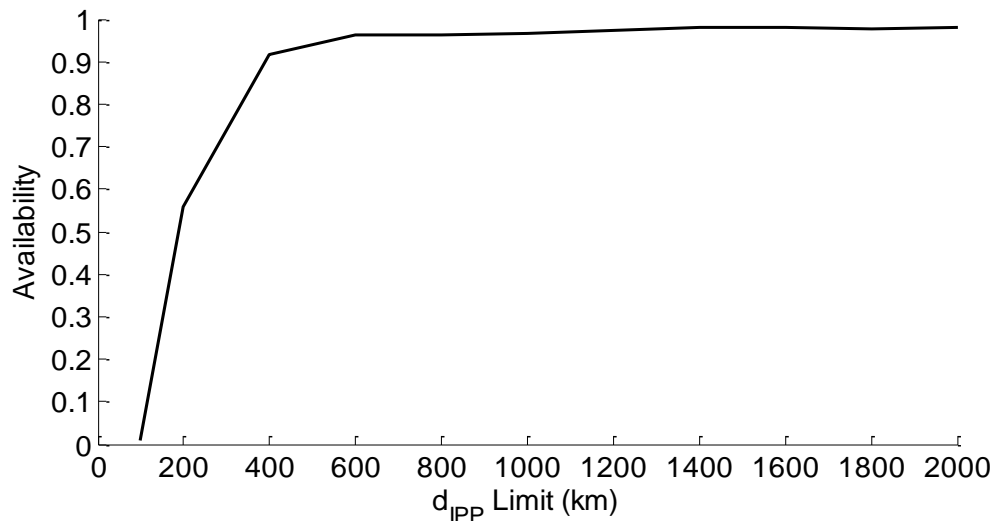


Figure 5.2. System Availability versus Maximum IPP Displacement [21]

The drop in system availability for maximum IPP displacements below 600 km is due to the increase of  $g_{VI}$  states (and ultimately an increase in positioning uncertainty) which are introduced to account for each segment of a satellite pass. For example, if a satellite pass is 1000 km long and the maximum IPP displacement over which the model can be applied is 100 km, then it will require ten segments to model the pass. The first segment provides the initial uncertainty, therefore it requires  $b_{VI}$  and  $g_{VI}$  states. For every subsequent segment, only a  $g_{VI}$  state is needed because the initial uncertainty is already known from the first segment. The initial bias and the ten gradient states each have their own uncertainty. Consequently, since there will be more parameters (each with a degree of uncertainty) in the iGPS estimation algorithm, the uncertainty in the position solution will be larger. This leads to a decrease in system availability.

Results from figures 5.1 and 5.2 must be considered together in order to determine the maximum tolerable IPP displacement for the error model. From the result of figure 5.2, displacements below 600 km are excluded due to the rapid decrease in system availability. The maximum IPP displacement for which the vertical ionospheric

delay varies linearly with IPP displacement is selected to be between 700 km and 800 km so that, even for the three sigma curve in figure 5.1, the standard deviation of the residuals is less than 1.4 cm. This is much less than the assumed measurement noise standard deviation. In addition, this range assures that the predicted system availability will reach 95% or higher. Displacements above the 700-800 km range could provide improved availability performance, but larger displacements would cause higher residual mis-modeling errors.

**5.1.2 Validation Results.** The model is applied to 700-800 km segments of satellite passes from multiple CORS sites between January and August 2007. The bias and gradient parameters,  $b_{VI}$  and  $g_{VI}$ , are estimated for each segment and the residual error is determined.

Figure 5.3 depicts an example showing the variation of the measured ionospheric error (dots) and the error model's fit to the error (line). Data for this figure is generated by using equation 4.20. The y-intercept for the model's fit (line) is the estimated  $b_{VI}$  value for the particular segment, with the slope of the line corresponding to the estimated  $g_{VI}$  value. This example shows that the range of ionospheric error present in the data is about 12 cm. The difference between the dots and the line are the residual errors which are dealt with throughout the rest of this work. Figure 5.3 provides visual representation that the error model removes a large majority of the ionospheric error, leaving centimeter-level residual errors (less than three centimeters). The residual error variation of the example given in figure 5.3 is shown in figure 5.4.

The header of figure 5.3 as well as those for subsequent figures throughout the rest of this work contains the following information: The first line provides the satellite

number (PRN), the date when the data was collected, and the CORS site designation (Table 5.1) of the location where the data was collected. On the second line of the header is the start time of the segment under consideration given in Coordinated Universal Time (UTC), the duration of time the segment was analyzed (i.e., the time it takes to achieve a displacement between 700 km and 800 km), and the daily single station index (Table 3.2),  $A_K$ , for the day when the data was collected.

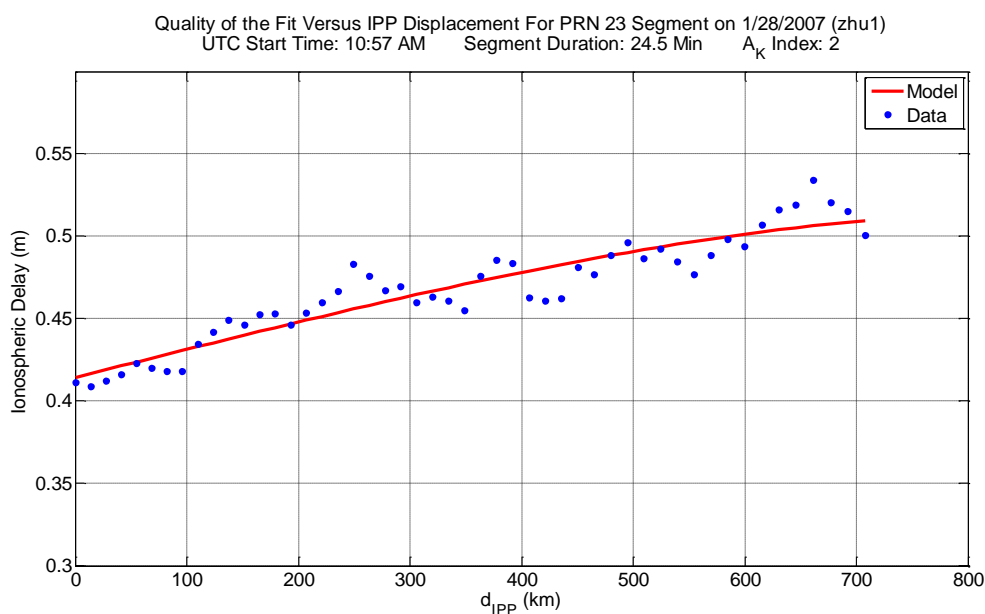


Figure 5.3. Data and Model for 700-800 km Segment at Houston, Texas

Individual segment residual error results are shown next. In the figures that follow, examples from various CORS sites on different days are displayed. Each figure contains two subplots. The top plot depicts the variation of the residual error as function of IPP displacement. The residual error is the difference between the actual measurements and the predicted measurements from the error model (i.e., difference between the dots and the line in figure 5.3). If the error model fits the data perfectly (including measurement noise), residual errors should be zero (horizontal line at  $y = 0$ ).

The bottom plot in the figures is the elevation angle of the satellite over the segment under consideration, plotted as a function of IPP displacement.

In figures 5.4-5.7, examples where residual errors are less than the measurement noise standard deviation of 2.3 cm are shown. These centimeter-level residuals mean that the model fits the data well. It suggests that high integrity positioning performance might be achievable because the error model accounts for the largest part of the ionospheric error. The remaining centimeter-level residual errors can be attributed to measurement noise and multipath effects present in the CORS data. In addition, the results in these figures show that centimeter-level residuals can be obtained for a wide range of elevation angles.

The example in figure 5.4 shows the residual error variation of the segment shown in figure 5.3. Considering figures 5.3 and 5.4 together shows that the error model removes about 10 cm of the error introduced by the ionosphere.

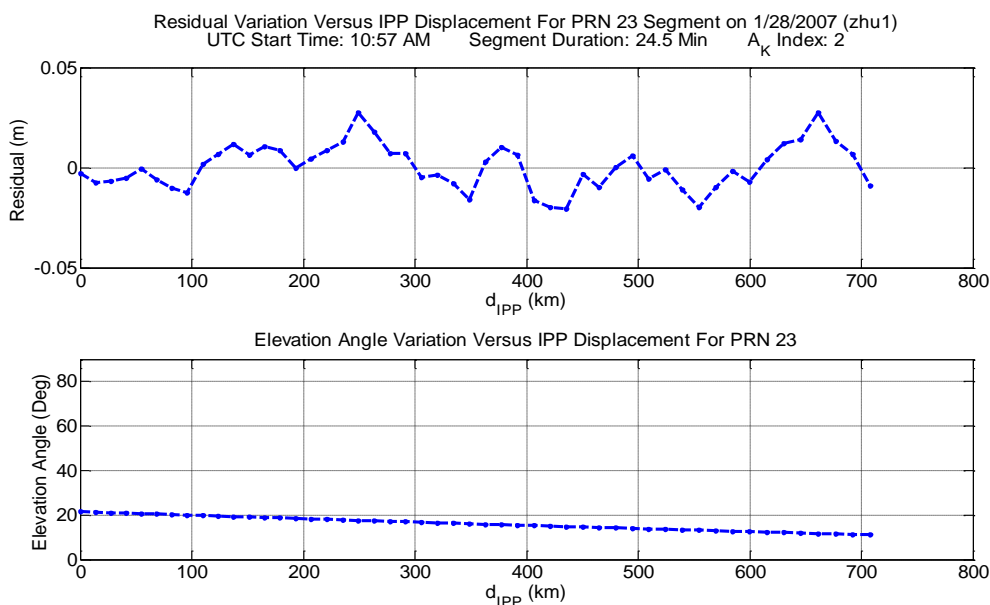


Figure 5.4. Model Analysis for 700-800 km Segment at Houston, Texas

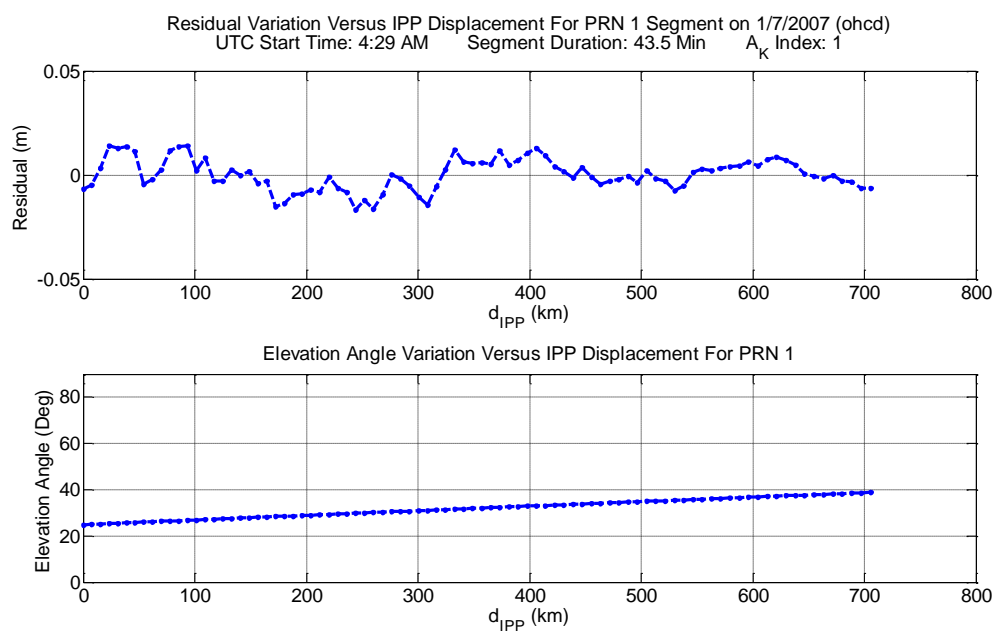


Figure 5.5. Model Analysis for 700-800 km Segment at Cleveland, Ohio

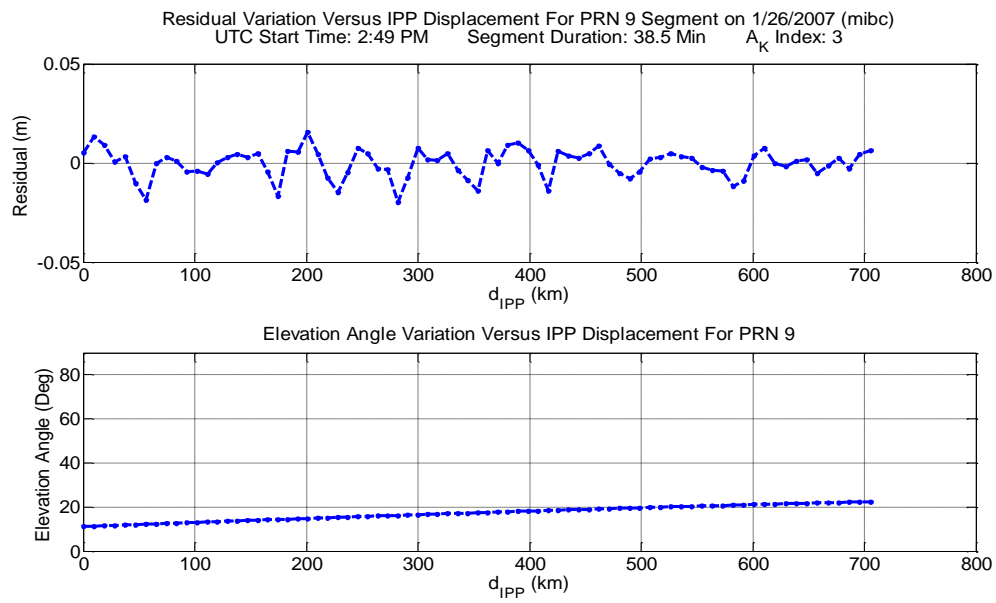


Figure 5.6. Model Analysis for 700-800 km Segment at Battle Creek, Michigan

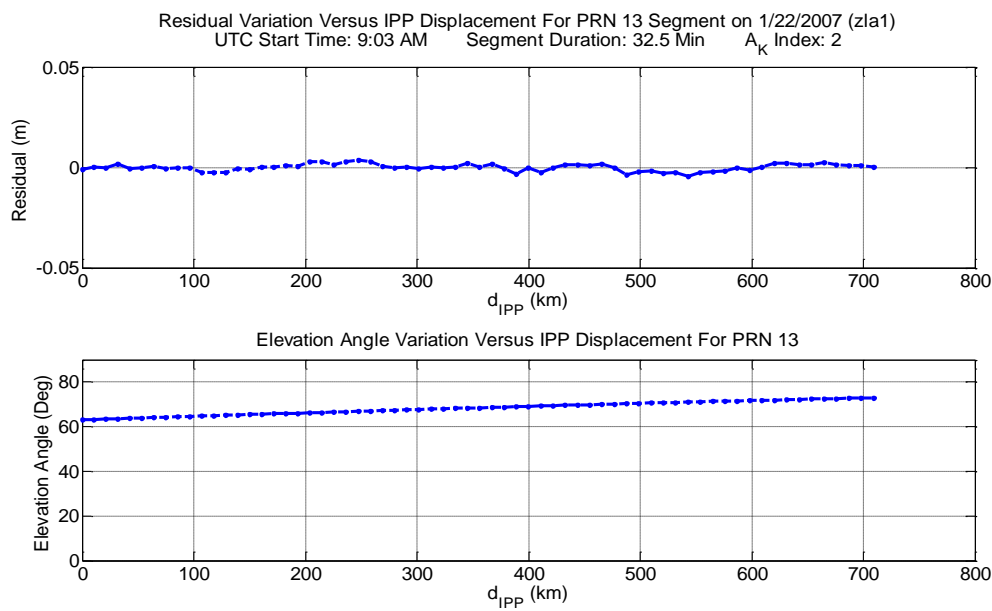


Figure 5.7. Model Analysis for 700-800 km Segment at Los Angeles, California

Figures 5.4-5.7 show that the model can produce centimeter-level residuals for 700-800 km segments. Centimeter-level residuals occur most often (this will be observed in the cumulative probability analysis shortly), but there are cases where decimeter-level residual magnitudes are present.

Even in the cases where decimeter-level residuals exist, the error model still removes much of the ionospheric error. Figure 5.8 shows the variation in the ionospheric error and the model's fit to this error for an example where decimeter-level residuals exist (the residual variation for this example is shown in figure 5.11). It is evident from this figure that without an error model, the variation in the ionospheric error would exceed one meter. The implementation of the error model reduces these errors to below 12 cm (this will be seen in figure 5.11).

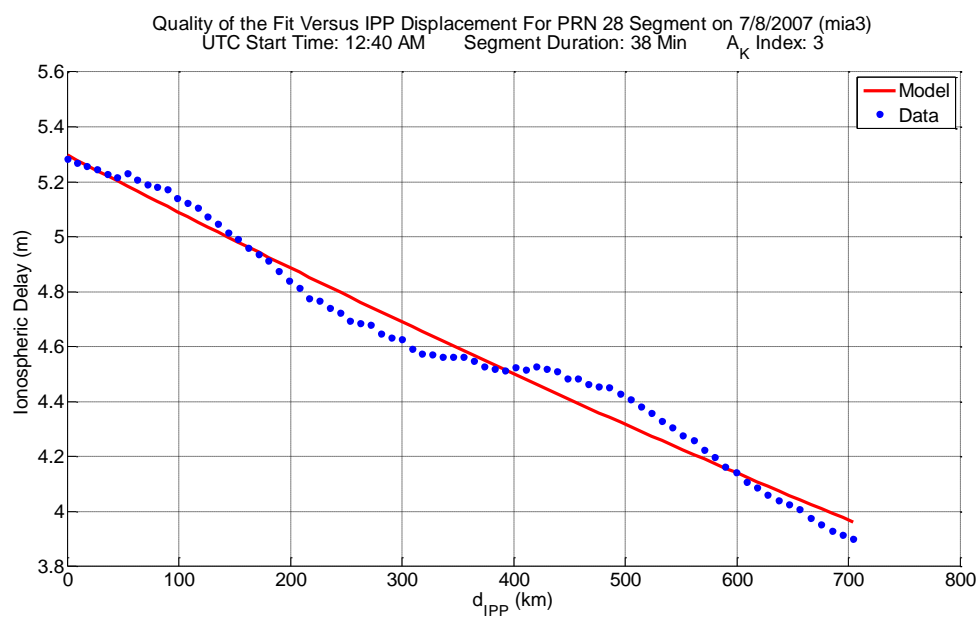


Figure 5.8. Data and Model for 700-800 km Segment at Miami, Florida

The following figures show examples where decimeter-level residual magnitudes are present. Residual variations observed in these examples exhibit bow (Figures 5.9 and 5.10) and wave-like (Figures 5.11 and 5.12) shapes. These variations contain residuals with magnitudes of 20 cm or more in some cases. Residual errors of this magnitude cannot be attributed to CORS measurement noise and multipath. In these cases, the original ionospheric error model is insufficient for its intended precision positioning application.

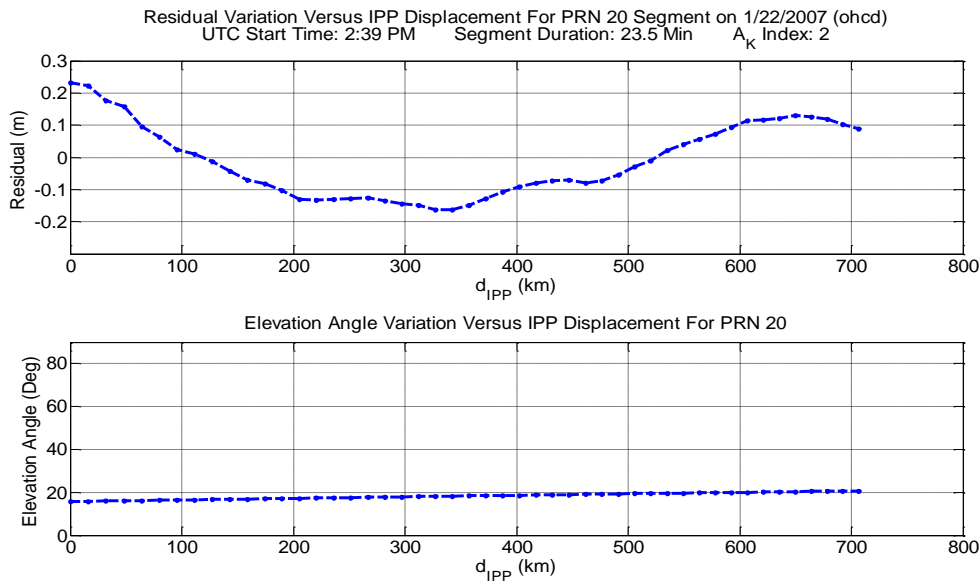


Figure 5.9. Model Analysis for 700-800 km Segment at Cleveland, Ohio

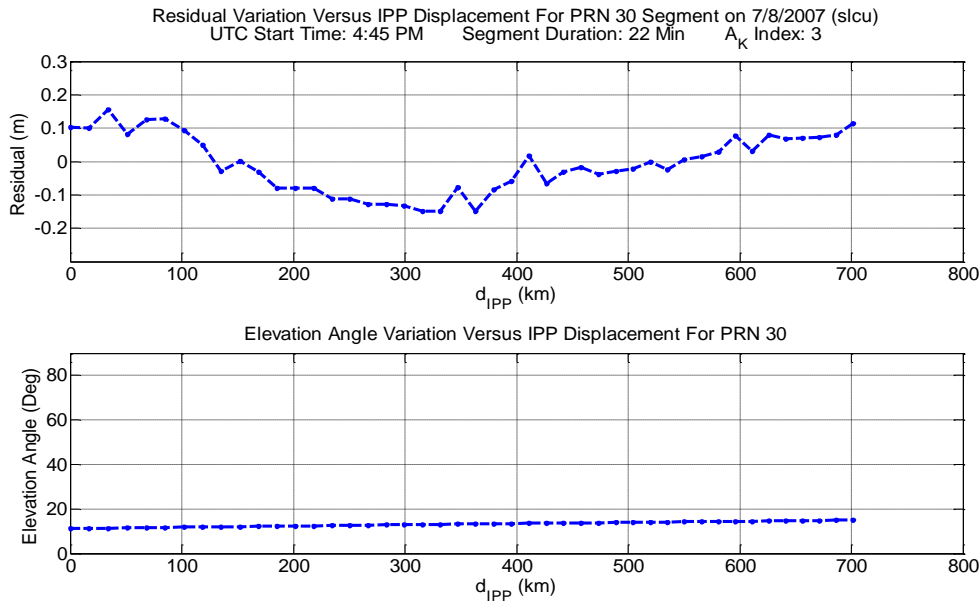


Figure 5.10. Model Analysis for 700-800 km Segment at Salt Lake City, Utah

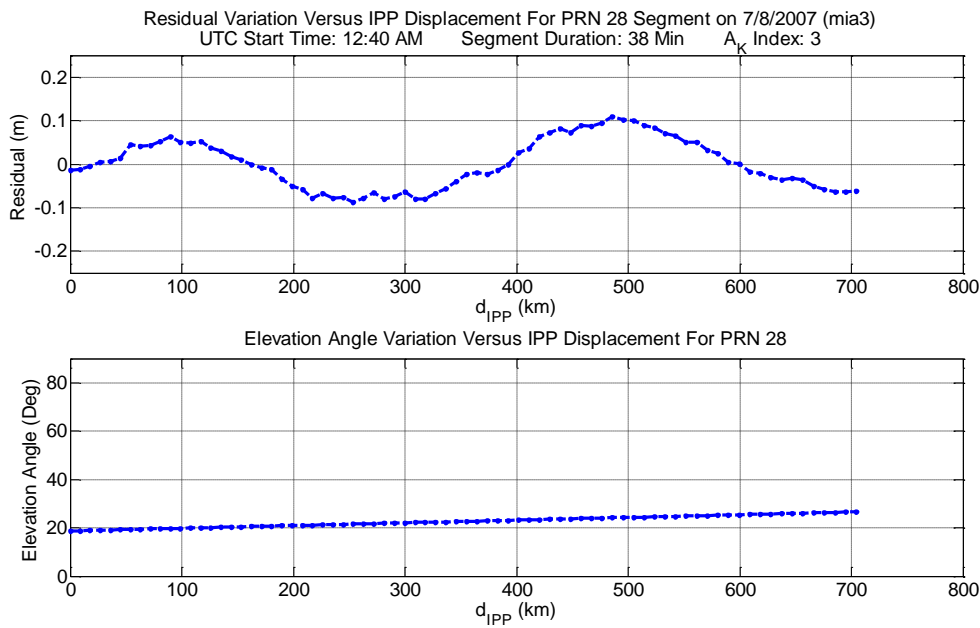


Figure 5.11. Model Analysis for 700-800 km Segment at Miami, Florida

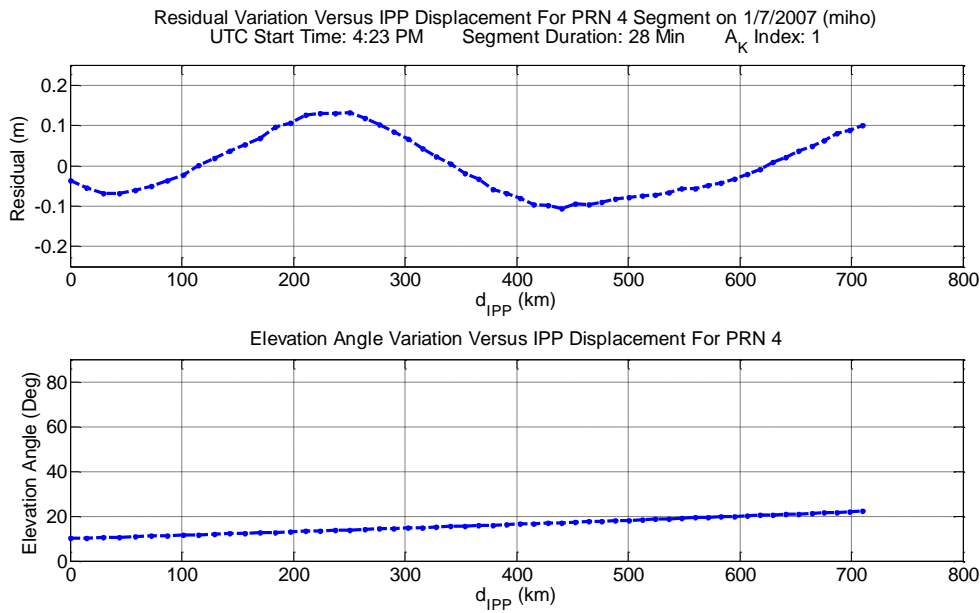


Figure 5.12. Model Analysis for 700-800 km Segment at Holland, Michigan

Many such segments must be considered in order to quantify the potential range of residual magnitudes produced by the model. When performing this analysis, the resulting residual error probability distribution is of interest.

A visual representation of the residual error distribution is obtained through the cumulative distribution function (CDF). Folded CDF plots constructed in this analysis are generated in the following manner. For cumulative probabilities greater than one half, the value of one minus the probability is plotted. This leads to the symmetry about zero. The y-axis (cumulative probability) is plotted on a logarithmic scale in order to more easily see the tails of the residual error distribution. In the context of this analysis, the tails of the residual error distribution are of significance since these inflate the standard deviation of the over-bounding Gaussian distribution, which will be discussed in the following paragraph. The sizes of the tails are driven by the amplitudes of the waves in the residual variations. This means that the impact of the wave-like structures on the model's ability to produce centimeter-level residuals can be determined through the folded CDF.

Plotted along with the folded residual CDF is the theoretical over-bounding Gaussian distribution. Over-bounding the folded residual error CDF with another distribution (here, a Gaussian distribution) ensures that all residual magnitudes are conservatively accounted for. A Gaussian distribution is used because it can be described with only two parameters, namely a mean and standard deviation. This makes a Gaussian distribution attractive for navigation purposes because fewer parameters need to be broadcast to users as compared to other types of distributions. A more thorough discussion of the meaning and sufficiency of CDF over-bounding can be found in [8].

To construct the folded residual CDF, the model is applied to all 700-800 km segments from all satellite passes on quiet days at the seven CORS sites listed in table 5.1. Performing this analysis leads to the folded CDF plot shown below in figure 5.13. The CDF in this figure contains the results from applying the model to 57,478 individual

segments. There are over 3.7 million residuals used in the construction of this folded CDF. The standard deviation of the over-bounding Gaussian distribution is 8.2 cm.

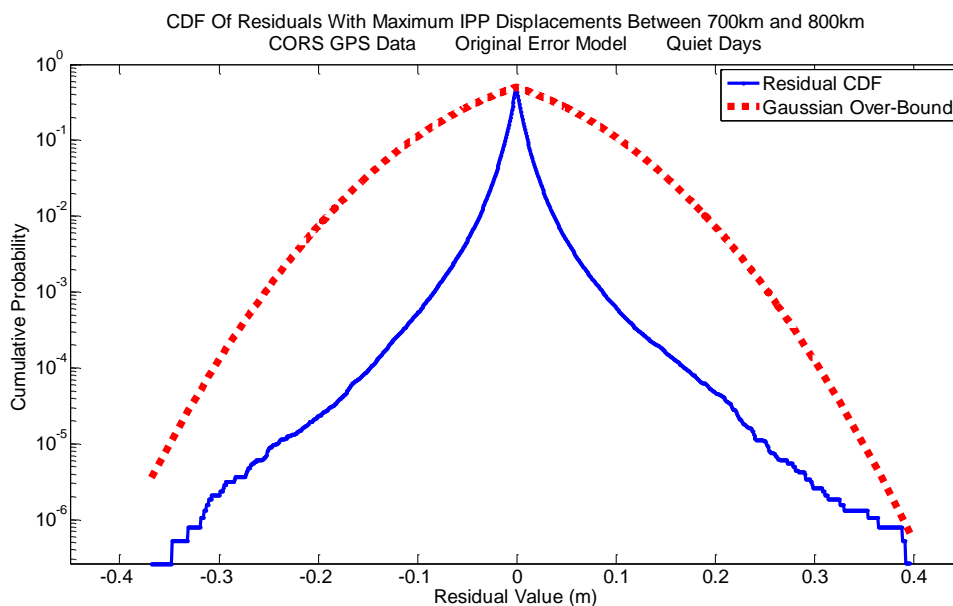


Figure 5.13. Folded Residual CDF for Quiet Ionospheric Days

The result of figure 5.13 shows the error model produces large residuals. This is evidenced by the tails of the residual distribution. These decimeter-level residuals have a lower probability of occurrence than centimeter-level residuals. The maximum residual values approach 40 cm and cause a large standard deviation of the over-bounding Gaussian distribution.

Cases for which the maximum residuals were observed are shown in figures 5.14 and 5.15. As expected, these cases exhibit wave-like structures. Since these waves in the residual variations increase the over-bounding standard deviation, it is important to understand the mechanisms for this behavior. Having a physical understanding of these waves is necessary for improving the model. Determining the driving forces behind these waves is the subject of the next sub-section.

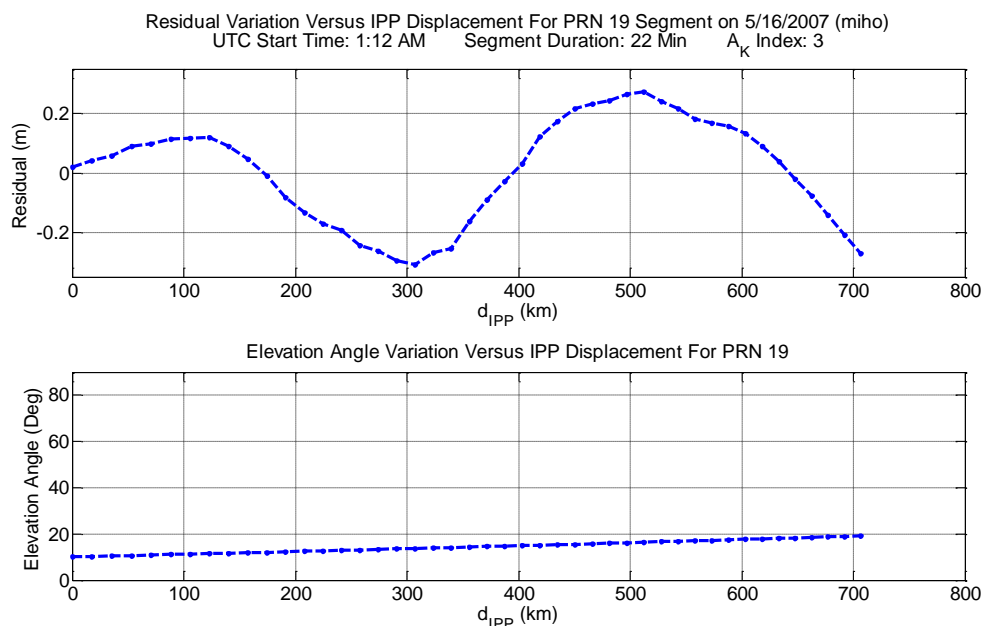


Figure 5.14. Worst Case Residual Example for Holland, Michigan

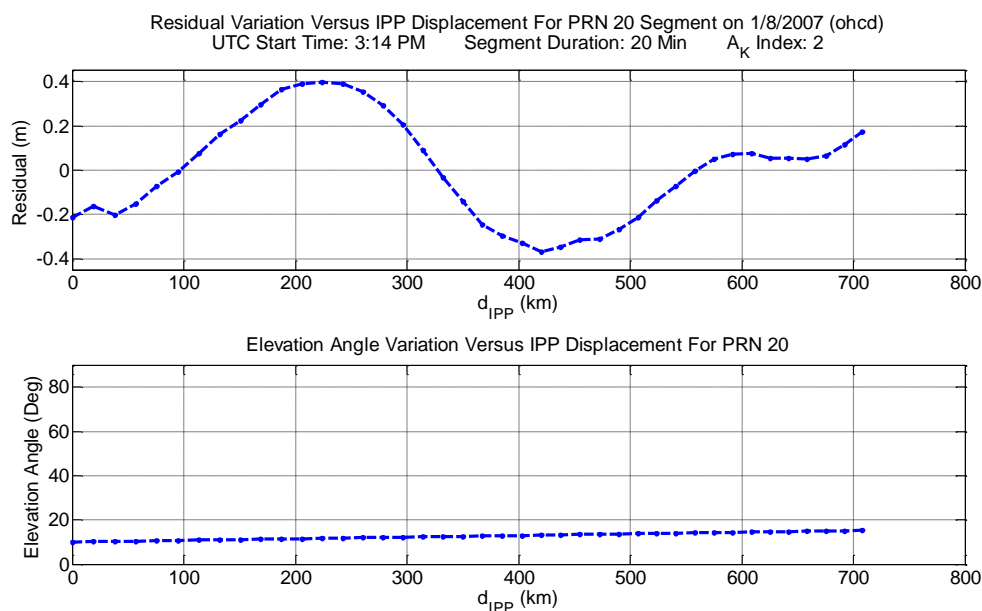


Figure 5.15. Worst Case Residual Example for Cleveland, Ohio

Estimated parameter values for the  $b_{VI}$  and  $g_{VI}$  terms have also been determined using the data from the seven CORS sites for quiet days and the methods described in sections 4.3.1 and 4.3.3. For each 700-800 km segment considered, an estimate of each parameter is obtained. The mean and standard deviation for each parameter are obtained

based on the 57,478 segments considered. Results from these computations are shown in table 5.3.

Table 5.3. Estimated Parameter Values for Quiet Ionospheric Days with Original Error Model

State	Mean Value	Standard Deviation
$b_{VI}(\text{m})$	1.38	3.71
$g_{VI}(\text{m/km})$	$1.99 \times 10^{-5}$	$1.20 \times 10^{-3}$

**5.1.3 Determining the Origin of the Wave-Like Structures.** There are a few possible causes for the existence of the wave structures. Multipath is one possible source, but it can quickly be ruled out. The sites chosen for this analysis are mostly free of obstacles in the vicinity of the receiver antenna and have a clear view of the sky in all directions. Another reason for excluding multipath is the amplitude of the waves. The amplitudes of these waves surpass 30 cm in several cases. This greatly exceeds the magnitude of error introduced by carrier phase multipath (usually on the order of a few centimeters).

Another possible source of these waves could be a malfunction in one of the receivers or antennas at the CORS sites. This hypothesis can also be ruled out after researching the receivers present at each site. It is found that each site used in this work is equipped with different receiver types and manufacturers. Since these waves are observed at all sites over many days, it is highly unlikely that these structures are caused by a specific receiver malfunction.

Ruling out multipath and receiver malfunctions as plausible causes for the waves leaves the ionosphere itself as the only possible cause. Based on the discussion of TIDs in chapter 3, wave-like behavior in the ionosphere is known to be associated with these phenomena. This means that TIDs could be the origin for these wave-like structures. To

test this hypothesis, quiet days over one winter month and one summer month are analyzed. The motivation for this analysis is based on the known characteristics of TIDs. TIDs have been found to occur more often during the daytime in the winter and in the night during the summer [16]. In addition, waves normally occur more often during the winter than in the summer. Showing that the occurrences of these waves follow similar patterns will be strong evidence for linking TIDs to these observed structures.

A residual threshold of 10 cm is used to detect waves. Each segment is screened to see if any residual exceeds this threshold value. The threshold is chosen to be 10 cm based on the analysis of individual segments where these waves are known to exist. It has been verified that the vast majority of segments whose residuals exhibit a wave-like shape have at least one residual which exceeds 10 cm, although there are a few cases with residuals exceeding 10 cm where the residual variation cannot be described as wave-like (examples of these will be shown in chapter 6). A 10 cm threshold enables waves to be identified without including segments that are only affected by multipath and receiver noise.

The error model is applied to all 700-800 km-long segments of all satellite passes from one winter and one summer month from the seven CORS sites. Residual errors are computed for each segment and compared to the 10 cm threshold. Figure 5.16 shows segments that exhibit waves in the residual variation on quiet days in January 2007, while segments exhibiting waves in July 2007 are depicted in figure 5.17. The segments in these figures are represented by the trace of their GSM latitude and longitude.

Daytime hours for this analysis are set to be between 7AM and 7PM local time, while nighttime hours are between 7PM and 7AM local time. These times are based on

the average sunrise and sunset times for the sites and months considered in this analysis as determined from the Astronomical Applications Department of the United States Naval Observatory [2]. This also ensures that an equal amount of time (12 hours) is allotted to day and night.

In figures 5.16 and 5.17, zero degrees longitude corresponds to local noon time. Since the earth rotates through fifteen degrees of longitude per hour and time on the ionosphere increases going from left to right in the figures, indicated by the arrow below each figure, 7AM corresponds to 75 degrees longitude and 7PM corresponds to -105 degrees longitude. Flags indicating these times are shown in figures.

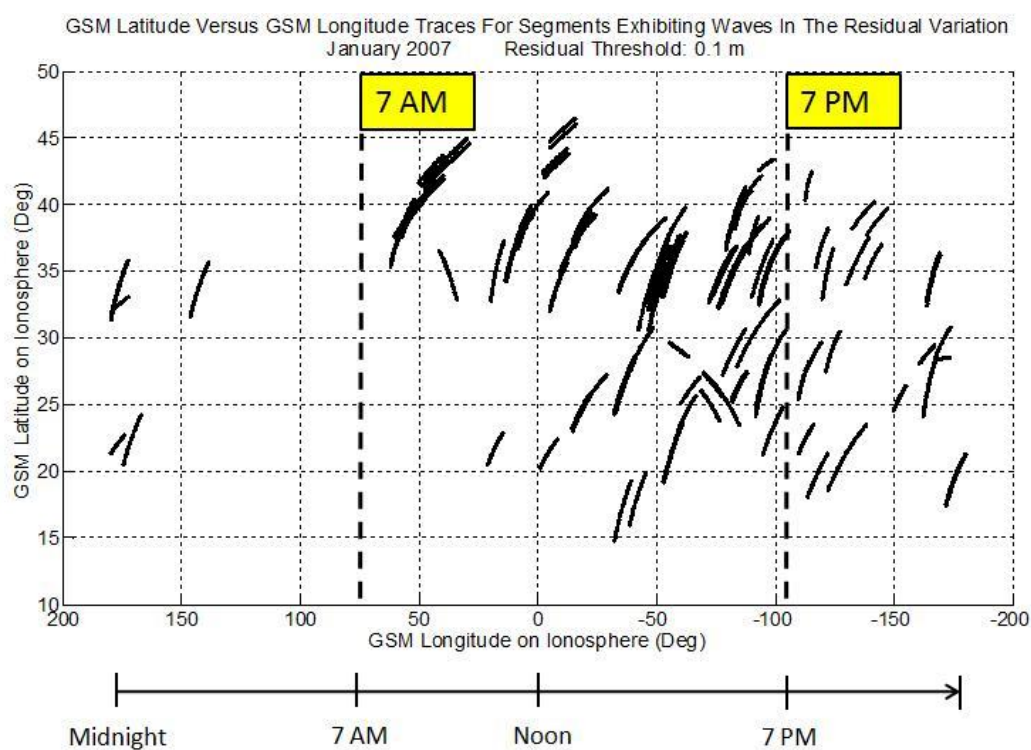


Figure 5.16. Segments Exhibiting Wave Events in January 2007

Figure 5.16 demonstrates that the majority of the traces with a residual exceeding 10 cm during January lie between 7AM and 7PM (daytime hours). Similarly, most of the

traces with residuals greater than 10 cm during July (Figure 5.17) are observed during nighttime hours (7PM and 7AM).

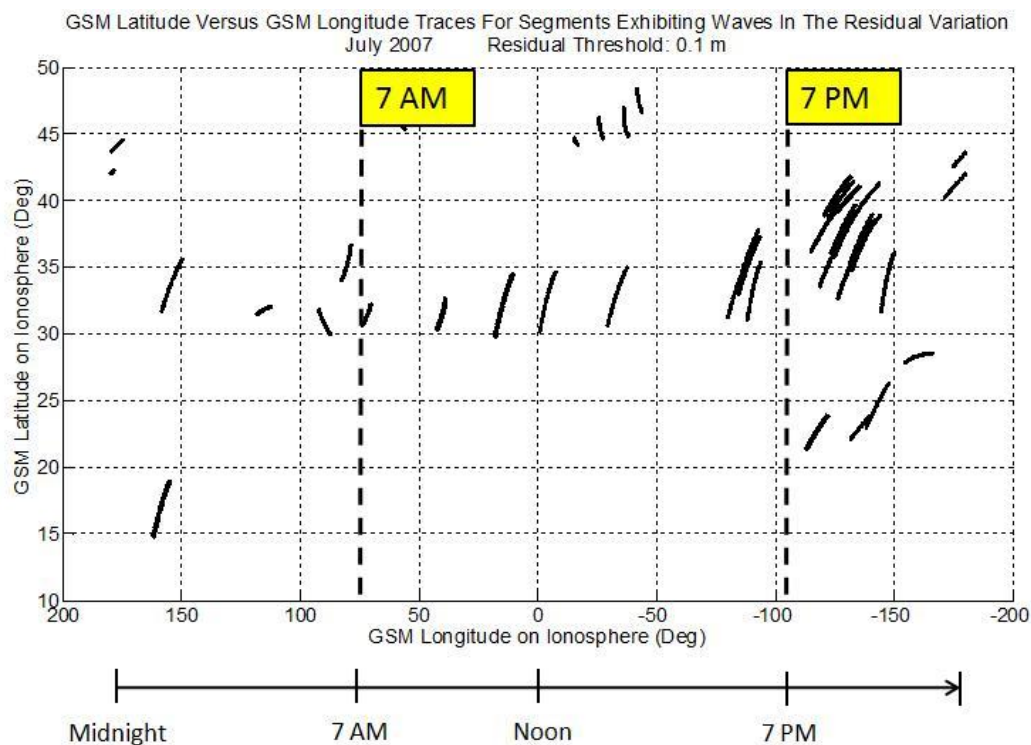


Figure 5.17. Segments Exhibiting Wave Events in July 2007

Table 5.4 displays the results of characterizing the occurrence of these wave structures. The results in the table show that during January, these waves occur more often during the daytime as compared to the nighttime. During July, these waves appear more during the nighttime than the daytime. In addition, there are more wave events that happen during the winter than in the summer. These conclusions agree with the known behavior of TIDs. In addition, these events also have characteristics in common with both LSTIDs and MSTIDs. Amplitudes for LSTIDs are usually between 15 cm and 20 cm [7]. This corresponds to the range of amplitudes observed for the wave structures in the residual error variations. MSTIDs have wavelengths between 100 km and 300 km and a

period between 10 and 30 minutes [16]. The structures observed in this analysis fit the MSTID wavelength and period ranges.

Table 5.4. Summary of Winter and Summer Wave Analysis

Month	Total Number of Events	Number of Daytime Events	Number of Nighttime Events	Percentage of Daytime Events	Percentage of Nighttime Events
January 2007	266	159	107	59.77%	40.23%
July 2007	78	19	59	24.36%	75.64%

Table 5.5 lists the number of segments considered for each month, the number of segments with waves, and the percentage of occurrence of the waves. Based on the requirements for integrity risk (between  $1 \times 10^{-7}$  and  $2 \times 10^{-7}$  in any 150 seconds of an aircraft precision approach) and continuity risk (between  $1 \times 10^{-6}$  and  $8 \times 10^{-6}$  in any 15 seconds of an aircraft precision approach) for civil aviation [30], these waves cannot be treated as rare events, meaning the model needs to account for them. Incorporating wave-like structures into the model will help to decrease the magnitude and likelihood of occurrence of wave-like residual errors. This will be addressed in the next chapter.

Table 5.5. Wave Occurrences in Winter and Summer

Month	Number of Segments	Number of Wave Segments	Percentage of Occurrence of Waves
January 2007	22,035	266	1.21%
July 2007	24,917	78	0.313%

## 5.2 Unsettled Day Analysis

Unsettled days (and active days in section 5.3) are investigated to see how increased ionospheric activity affects residual error variations. These residual profiles can provide additional knowledge on how to best modify the model to capture most of the residual variations. This unsettled and active day analysis will also give information on the largest residual magnitudes that can be present on these types of days.

Unsettled days between January and August of 2007 at the Holland, Michigan CORS site are considered. These 126 days include 27,279 segments from which over two million residuals have been computed. Similar to the quiet day analysis, there are segments where all residuals are at the centimeter-level (near-zero residual variation) and others which have decimeter-level residuals.

Figure 5.18 shows the data and model fit for an example where decimeter-level residuals exist. From this figure it is observed that the variation in ionospheric error is nearly two meters in the absence of an error model. As will be seen in figure 5.19, the error model removes much of this error, leaving residuals on the order of 20 cm.

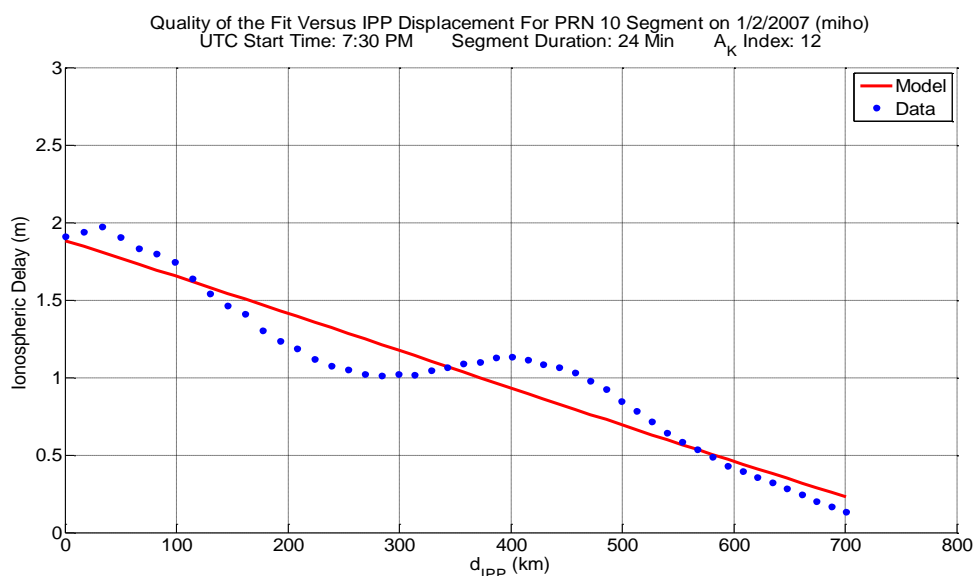


Figure 5.18. Data and Model for Unsettled Day Example at Holland, Michigan

Figures 5.19 and 5.20 show examples of individual cases where residuals exceed 20 cm. The residual variation in figure 5.19 has a wake-like structure similar to those found on quiet days (the data and fit for this example are shown in figure 5.18). Figure 5.20 shows an example which looks like a combination of two waves with different frequencies. These examples show the insufficiency of the original vertical delay model to capture the wide variety of structures that are present in the data on unsettled days.

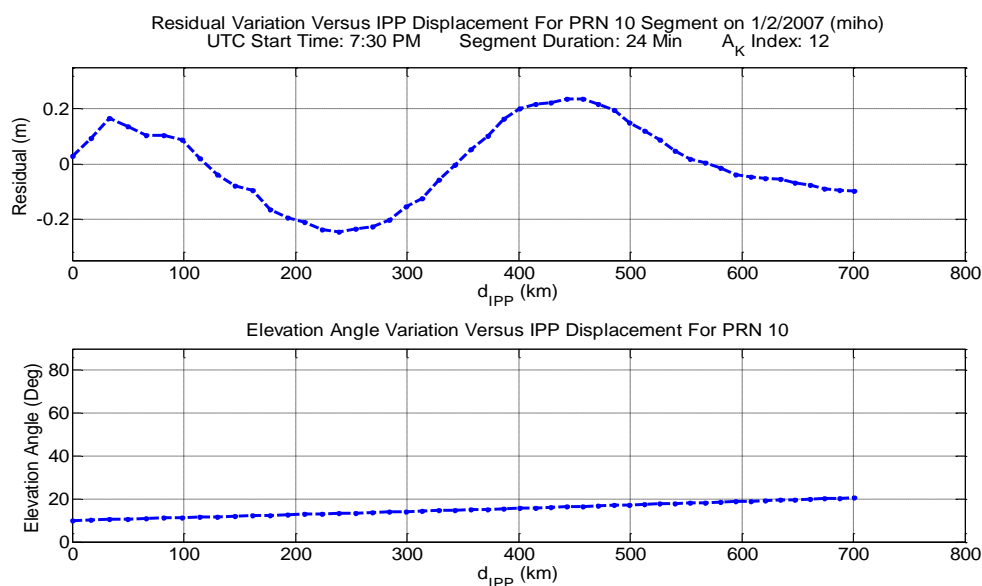


Figure 5.19. Unsettled Day Example at Holland, Michigan (1/2/07)

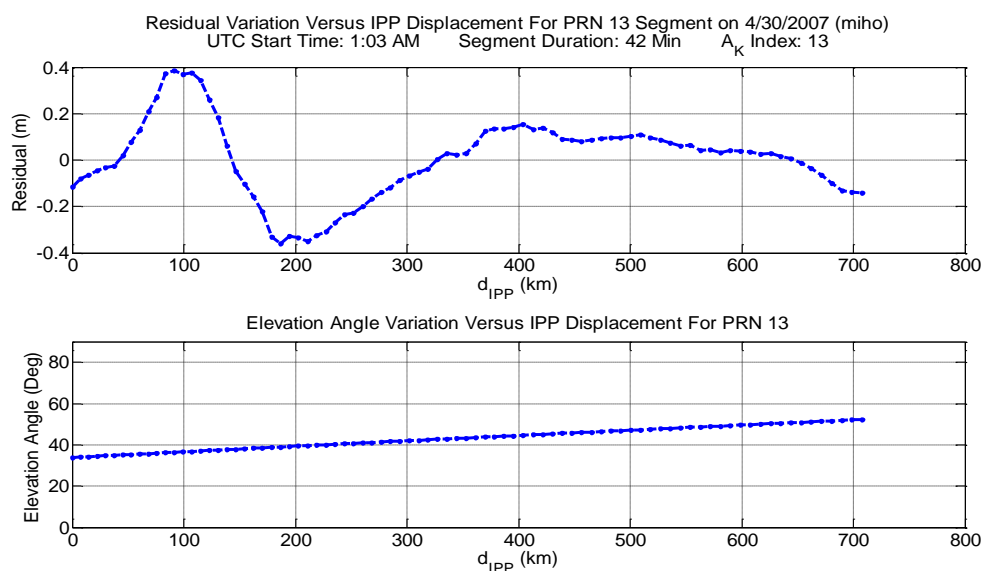


Figure 5.20. Unsettled Day Example at Holland, Michigan (4/30/07)

The insufficiency of the error model on unsettled days can be further seen in the folded residual CDF plot of figure 5.21. This plot is generated from the residuals after applying the model to all 27,279 segments for the 126 unsettled days considered. It shows the folded residual CDF along with the over-bounding Gaussian distribution.

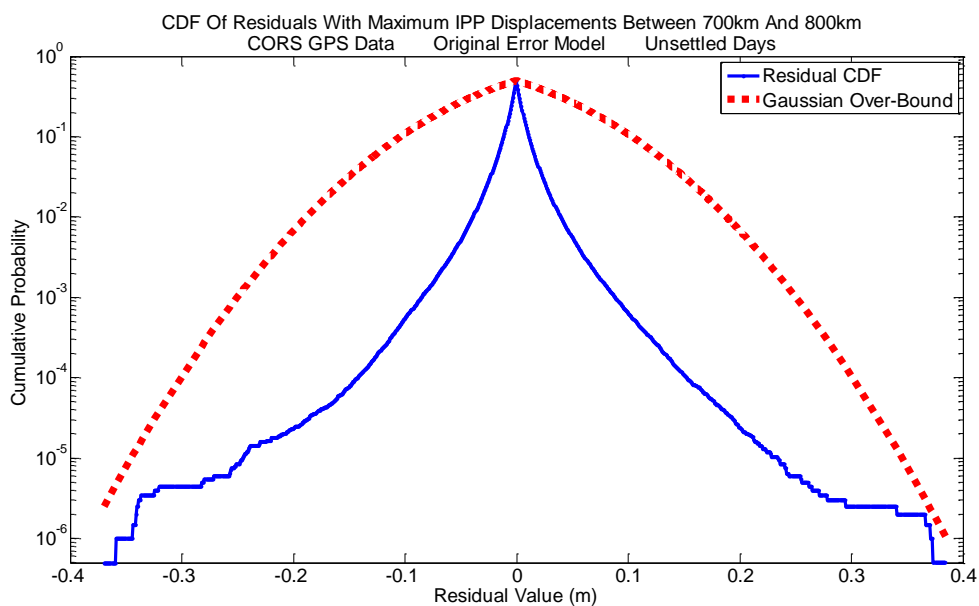


Figure 5.21. Folded Residual CDF for Unsettled Ionospheric Days

The standard deviation of the over-bounding Gaussian distribution in figure 5.21 is 8.1 cm. This standard deviation is nearly identical to that obtained for quiet days. Although residual magnitudes are similar on quiet and on unsettled days, there is a larger variety of shapes of residual variations during unsettled days. As evidenced above in figure 5.20, some of these variations do not look like a single-wave structure, but rather a combination of multiple waves.

Table 5.6 displays the mean and standard deviation of the estimated  $b_{VI}$  and  $g_{VI}$  parameters from the unsettled day segments. The standard deviations of these values are higher than those for quiet days. This can be attributed to the fact that there is greater

variability in the data. Also, the sample size is not as large as for quiet days since only one site is considered.

Table 5.6. Estimated Parameter Values for Unsettled Ionospheric Days with Original Error Model

State	Mean Value	Standard Deviation
$b_{VI}(m)$	1.34	4.21
$g_{VI}(m/km)$	$-9.2 \times 10^{-6}$	$1.36 \times 10^{-3}$

### 5.3 Active Day Analysis

The 16 active days between January and August of 2007 at the Holland site are considered next. For this analysis, 3,425 segments have been considered, and from these segments, over 247,000 residuals are computed.

In order to show that the model removes most of the ionospheric error even on active days, the example in figure 5.22 is shown. This figure depicts the variation in the ionospheric error and the model's fit to these errors. In the absence of the error model, the error will be greater than 1.2 m. Application of the model to this data reduces the errors to 15 cm or less (this is shown in figure 5.23).

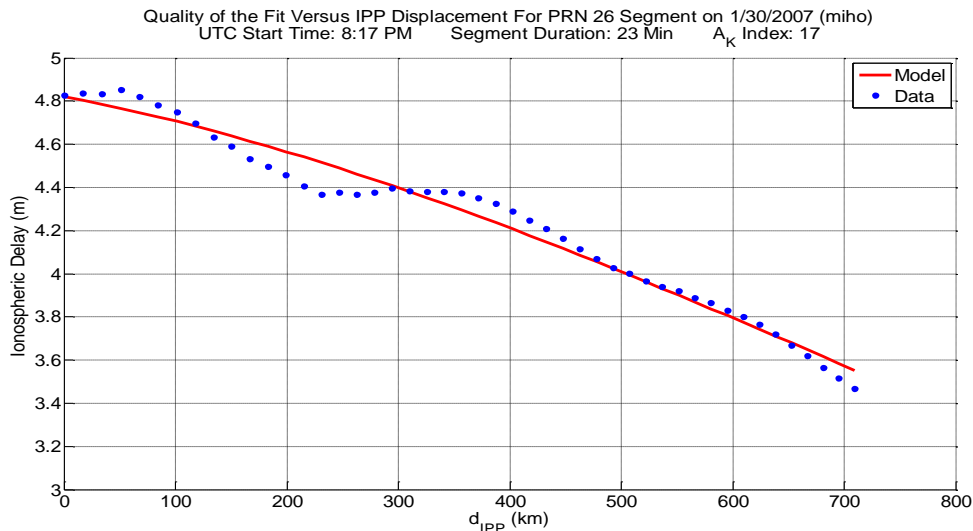


Figure 5.22. Data and Model for Active Day Example at Holland, Michigan

Figures 5.23 and 5.24 show two segments where some of the largest residual magnitudes were found during these active days. The residual variations in these figures cannot be categorized as single-wave type structures. In both of these examples, the structure appears to change its frequency as elevation angle is increased. As with unsettled days, the original model is not capable of accounting for all of the extreme variations in the data.

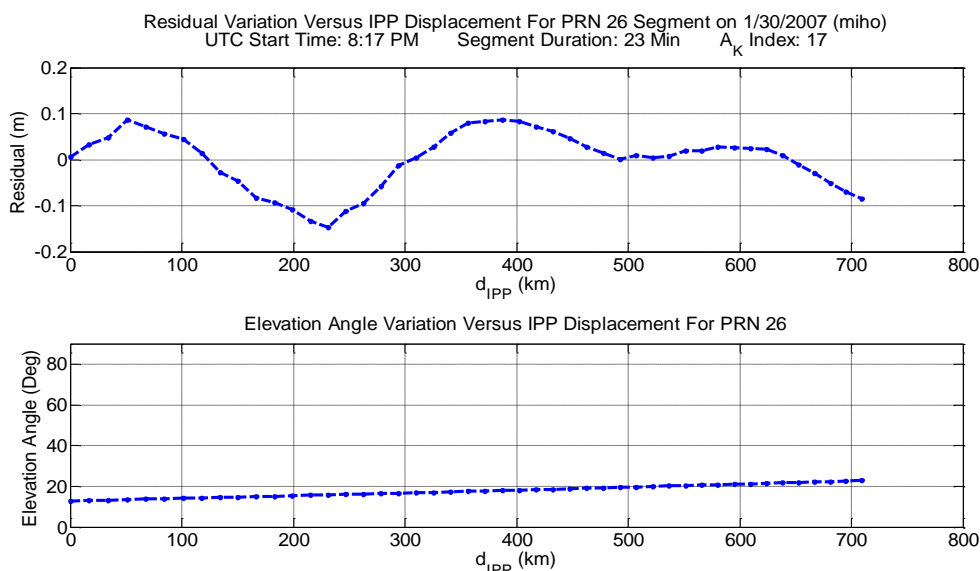


Figure 5.23. Active Day Example at Holland, Michigan (1/30/07)

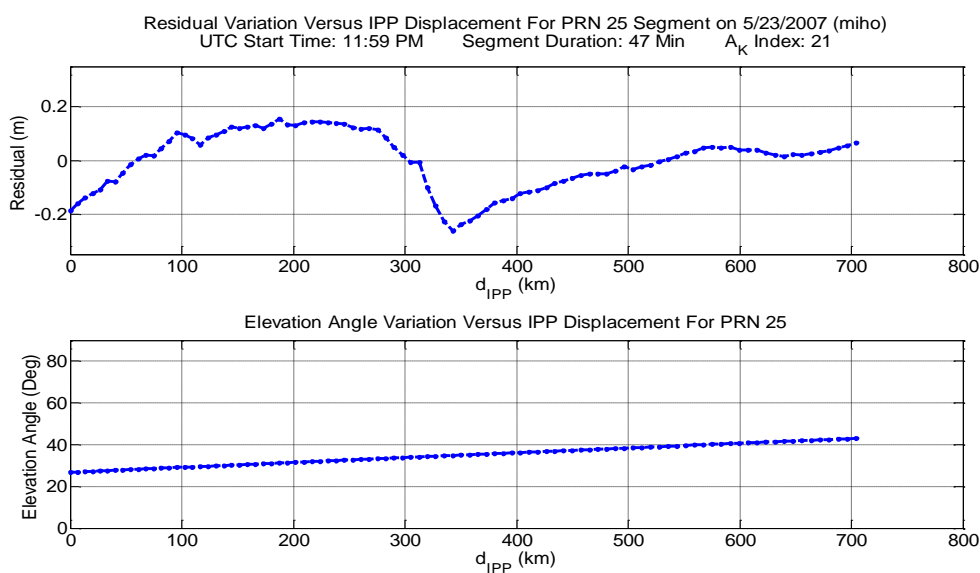


Figure 5.24. Active Day Example at Holland, Michigan (5/23/07)

The folded residual CDF and corresponding Gaussian over-bound generated from the 3,425 active day segments are shown in figure 5.25. For the over-bounding Gaussian, the standard deviation is 6.3 cm.

The residual error distribution is not as wide as the quiet and unsettled day distributions. This is due to the smaller sample size of available residuals because active days do not occur as frequently as unsettled days. Even with the smaller data set, evidence is provided that residual magnitudes exceed the centimeter-level (some residuals exceed 25cm). The original vertical delay model does not robustly account for ionospheric error variations.

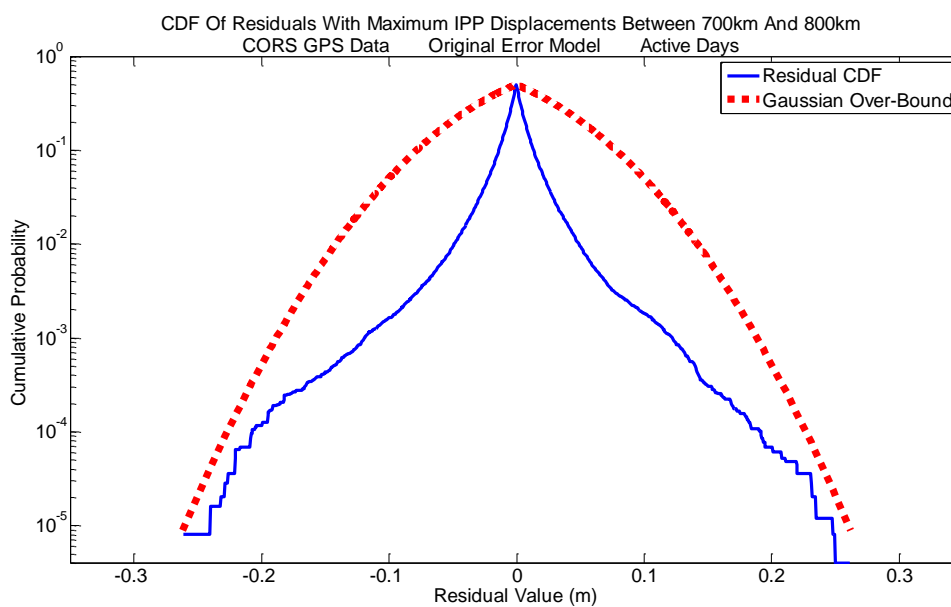


Figure 5.25. Folded Residual CDF for Active Ionospheric Days

Estimated parameter values for  $b_{VI}$  and  $g_{VI}$  computed from the active day segments are shown in table 5.7. The larger standard deviations of these estimates can be attributed to the fact that the bias and slope distributions exhibit greater variability during active days.

Table 5.7. Estimated Parameter Values for Active Ionospheric Days with Original Error Model

State	Mean Value	Standard Deviation
$b_{VI}(\text{m})$	1.34	6.35
$g_{VI}(\text{m/km})$	$1.34 \times 10^{-5}$	$2.01 \times 10^{-3}$

Results from quiet, unsettled and active days provide evidence that the model must be improved. The over-bounding Gaussian distributions for quiet, unsettled, and active days all have standard deviations of greater than five centimeters. The values of these standard deviations are driven by the amplitudes of TIDs. These decimeter-level TID amplitudes and the fact that these waves cannot be considered as rare events means that the model needs to incorporate TIDs in an effort to decrease the size of the largest residual magnitudes. Accounting for TIDs is addressed in the next chapter.

## CHAPTER 6

### MODEL MODIFICATION TO ACCOUNT FOR TRAVELING IONOSPHERIC DISTURBANCES

The TID wave structures in the residual error variations shown in chapter 5 are observed more than 1.2% of the time during the winter and more than 0.3% of the time during the summer. As mentioned in the previous chapter, these percentages of occurrence are much greater than the requirements for integrity risk (between  $1 \times 10^{-7}$  and  $2 \times 10^{-7}$  in any 150 seconds of an aircraft precision approach) and continuity risk (between  $1 \times 10^{-6}$  and  $8 \times 10^{-6}$  in any 15 seconds of an aircraft precision approach) requirements for civil aviation [30]. This means that these waves cannot be treated as rare events and must be accounted for in the ionospheric error model.

Modifying the model must be done with validation objectives in mind, namely to examine residual magnitudes after applying the model and to obtain estimated parameter values for the states within the model. Additional terms can be added to the model to account for the wave structures and, therefore, reduce the largest residual magnitudes. Unfortunately, determining the structure of and parameter values for these extra model terms is not straightforward. Furthermore, as will be discussed later in this chapter, inclusion of additional ionospheric state parameters will ultimately result in a reduction in availability of high accuracy positioning.

#### **6.1 Quadratic Model**

The results presented in the previous chapter show that a wide range of shapes in the residual variations exists. The addition of a quadratic term to the model is investigated first, with the motivation that it may help to reduce residual magnitudes by

accounting for observed bows in the vertical ionospheric errors (Figures 5.9 and 5.10).

The use of a quadratic term also provides two additional benefits. First, it only introduces one additional term to the model. This means that only one more parameter needs to be included in the iGPS estimation algorithm, thereby maintaining higher system availability. Secondly, the error model is kept linear with respect to the states within it.

The quadratic error model is given by the following:

$$\epsilon_{I,k} = c_{OB,k}(b_{VI} + d_{IPP,k} \cdot g_{VI} + q_{VI} \cdot d_{IPP,k}^2) \quad (6.1)$$

where  $q_{VI}$  is the quadratic coefficient. Since equation 6.1 is linear with respect to the parameters to be estimated, model evaluation follows the same procedure as the original vertical delay model in the previous chapter.

Stacking measurements over the sampling period yields a system similar to the one given in equation 4.16:

$$\begin{bmatrix} z_1 \\ \vdots \\ z_n \end{bmatrix} = \begin{bmatrix} c_{OB,1} & c_{OB,1} \cdot d_{IPP,1} & c_{OB,1} \cdot d_{IPP,1}^2 & 1 \\ \vdots & \vdots & \vdots & \vdots \\ c_{OB,n} & c_{OB,n} \cdot d_{IPP,n} & c_{OB,n} \cdot d_{IPP,n}^2 & 1 \end{bmatrix} \begin{bmatrix} b_{VI} \\ g_{VI} \\ q_{VI} \\ b \end{bmatrix} + \begin{bmatrix} v_1 \\ \vdots \\ v_n \end{bmatrix} \quad (6.2)$$

where  $z_k$ ,  $b$ , and  $v_k$  are defined in chapter 4.

Prior knowledge on the  $b_{VI}$  and  $g_{VI}$  states is incorporated by pseudo-measurement augmentation using the same values as given in table 5.2. Since no information on  $b$  or  $q_{VI}$  is available, no prior knowledge is given for these states.

The results of the quadratic model analysis are presented in comparison with the original model. This analysis is carried out on the same quiet day data as the original model in chapter 5 (i.e., using data collected over eight months from the seven CORS sites listed in table 5.1 with a ten degree elevation mask).

Figure 6.1 shows a comparison between the original and quadratic models for a case where no TID wave exists in the residual variation of the original model, and all residual magnitudes are below two centimeters. This figure shows that the quadratic model matches the results of the original model in this case.

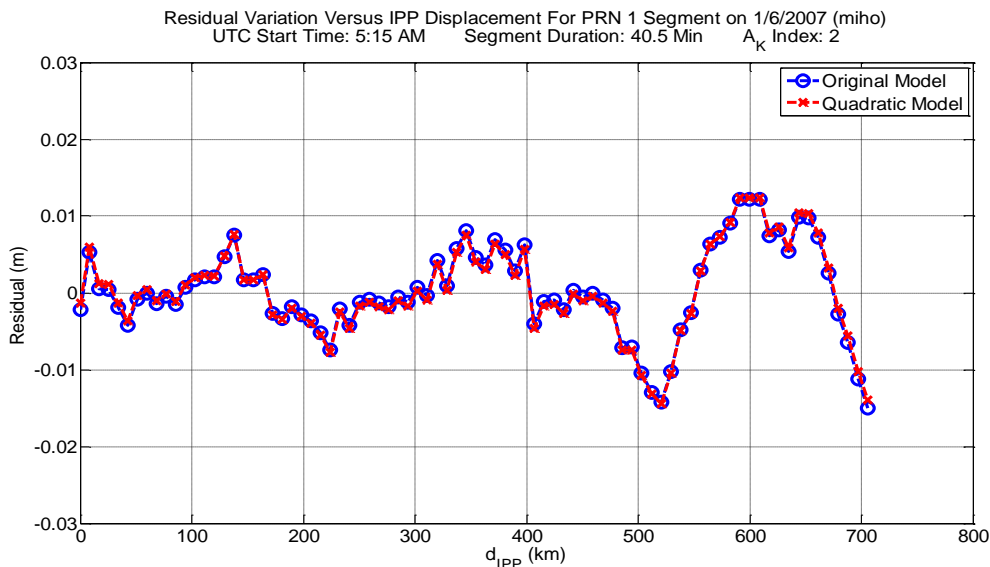


Figure 6.1. Original and Quadratic Model Comparison at Holland, Michigan

Figures 6.2 and 6.3 depict the comparison between the original and quadratic models for instances where bow shapes with decimeter-level residuals are present in the residual variation of the original model (Figures 5.9 and 5.10). These examples show that the quadratic model effectively reduces all residuals to below 10 cm in these cases.

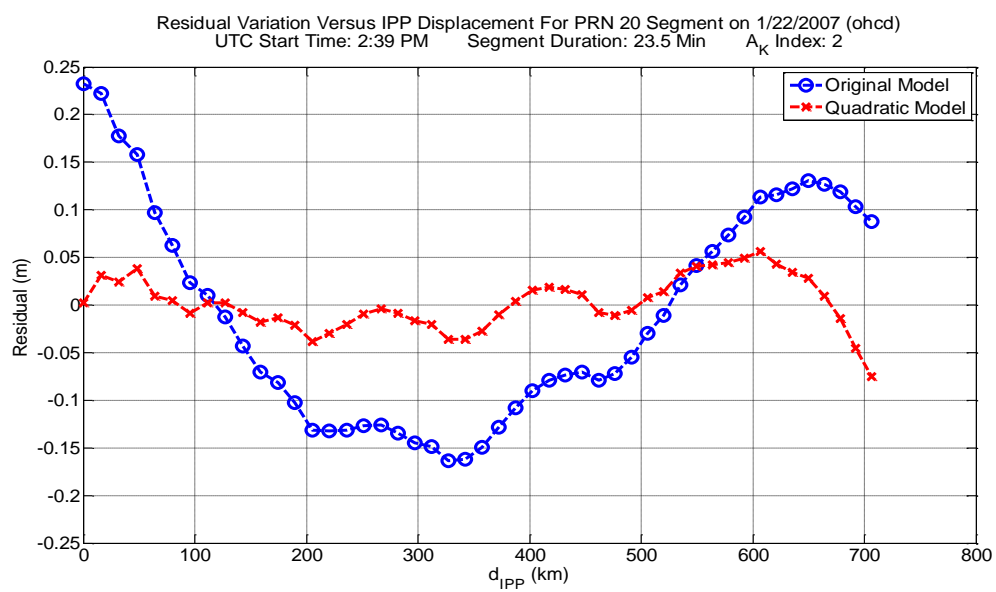


Figure 6.2. Original and Quadratic Model Comparison at Cleveland, Ohio

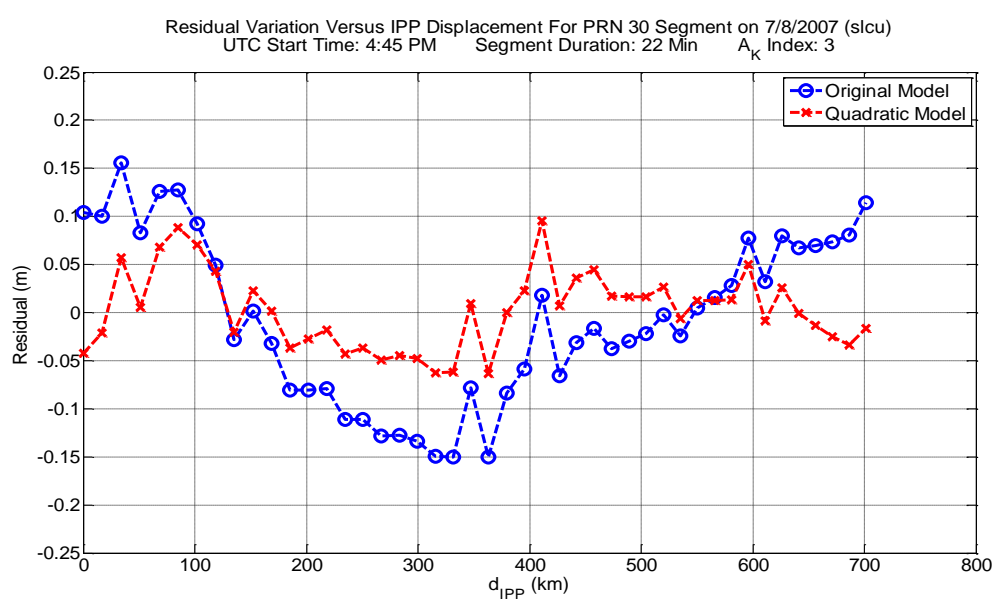


Figure 6.3. Original and Quadratic Model Comparison at Salt Lake City, Utah

A comparison between the original and quadratic models for an example with a TID wave in the residual variation of the original model is shown in figure 6.4. It is clear from this figure that the quadratic model does not substantially reduce the largest residual magnitudes.

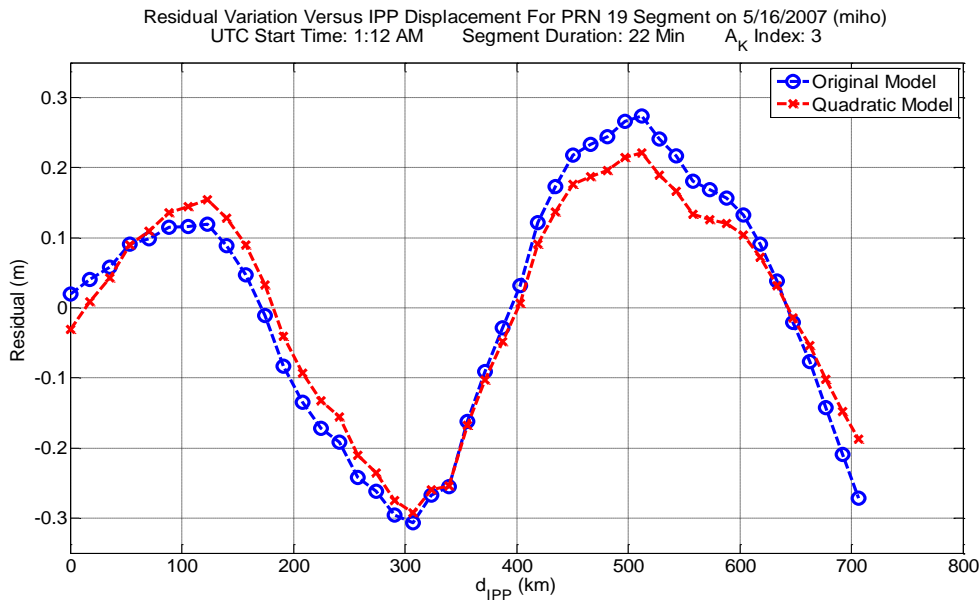


Figure 6.4. Original and Quadratic Model Comparison at Holland, Michigan

To see the overall impact of the quadratic term, the folded residual CDF (introduced in chapter 5) is constructed and plotted in figure 6.5. The folded residual CDF for the original vertical delay model is also plotted in figure 6.5. This is done to make a direct comparison between the two models.

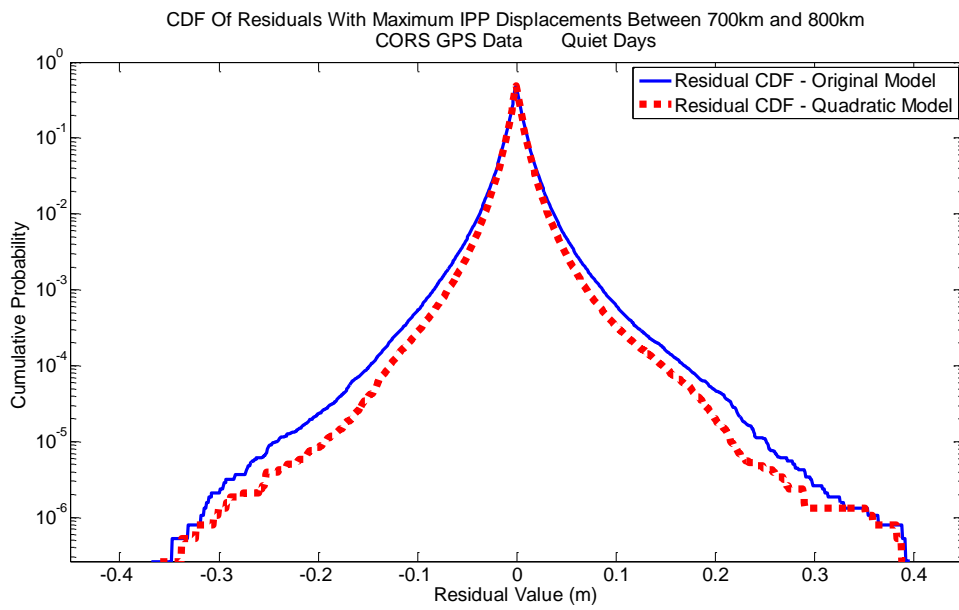


Figure 6.5. Folded Residual CDF Comparison between Original and Quadratic Models

From figure 6.5, it is apparent that the quadratic model provides little benefit for cases that impact the tails of the residual error distribution, although it does provide benefit in other cases (Figures 6.2 and 6.3). This conclusion is expected given the results of figure 6.4, which shows that the quadratic model does not significantly reduce the largest residual magnitudes from the original model. This result also means that the standard deviation of the over-bounding Gaussian distribution is not significantly decreased. In the previous chapter, it was determined the standard deviation of the Gaussian distribution for quiet days is 8.2 cm. The quadratic model's over-bounding standard deviation is 8.0 cm, which is clearly much larger than the underlying centimeter-level measurement noise.

Estimated parameter values for the states in the quadratic model have been determined, and are provided in table 6.1.

Table 6.1. Estimated Parameter Values for Quiet Ionospheric Days with Quadratic Error Model

State	Mean Value	Standard Deviation
$b_{VI}(m)$	1.85	2.75
$g_{VI}(m/km)$	$5.2 \times 10^{-5}$	$1.05 \times 10^{-3}$
$q_{VI}(10^{-3} /km)$	$-4.3 \times 10^{-5}$	$5.71 \times 10^{-4}$

## 6.2 Sinusoidal Model

The quadratic model does not provide a significant decrease in magnitude of the largest residuals. Since a majority of the observed TIDs are cyclic in nature, a sinusoidal term will be added to the model in an effort to reduce residual magnitudes. Moreover, because the quadratic model offers little improvement and in order to minimize the

number of parameters in the model, adding both quadratic and sinusoidal terms at the same time will not be considered.

A problem with adding a sinusoid is that two nonlinear parameters will be introduced, namely the sine wave frequency and phase. The nonlinear phase parameter can be eliminated if trigonometric identities are used. For instance, the sinusoidal term to be added can be written as:

$$a \cos(2\pi f d_{IPP} + \psi) \quad (6.3)$$

where  $a$  is the amplitude,  $\psi$  is the phase, and  $f$  is the frequency. If the phase and frequency are held constant, equation 6.3 can be recast as:

$$\begin{aligned} a \cos(\psi) \cdot \cos(2\pi f d_{IPP}) - a \sin(\psi) \cdot \sin(2\pi f d_{IPP}) \\ = a_C \cos(2\pi f d_{IPP}) + a_S \sin(2\pi f d_{IPP}) \end{aligned} \quad (6.4)$$

Using the result of equation 6.4, the error model with the addition of the sinusoidal term will have the form of:

$$\epsilon_{l,k} = c_{OB,k} (b_{VI} + d_{IPP,k} \cdot g_{VI} + a_C \cos(2\pi f_{TID} d_{IPP,k}) + a_S \sin(2\pi f_{TID} d_{IPP,k})) \quad (6.5)$$

where  $a_C$  and  $a_S$  are the amplitudes of the cosine and sine terms, and  $f_{TID}$  is the frequency of the TID wave. This means that three additional parameters must be estimated, but the only nonlinear parameter is the frequency term,  $f_{TID}$ . The  $f_{TID}$  term is not a time-based frequency, but a frequency based on IPP displacement. Therefore, it has units of 1/km.

Throughout the rest of this work, the model given in equation 6.5 will be referred to as the sinusoidal model even though, like the original linear vertical delay model of equation 3.1, it is a vertical delay model that is further modulated by the obliquity factor.

The presence of the frequency parameter means that nonlinear estimation must be performed. The estimation will be carried out through the Newton-Raphson method, which provides a way to iteratively converge to a solution. The first step is to take equation 6.5 and convert it into a linearized model. This is achieved by expanding equation 6.5 into a first order Taylor series, yielding:

$$\epsilon_{I,k} = (\epsilon_{I,k})_0 + \Delta\epsilon_{I,k} \quad (6.6)$$

where the term  $(\epsilon_{I,k})_0$  is obtained by evaluating the nonlinear model given in equation 6.5 using the best available estimate of the state vector,  $\mathbf{x}$ , and  $\Delta\epsilon_{I,k}$  is given as:

$$\Delta\epsilon_{I,k} = \frac{\partial\epsilon_{I,k}}{\partial b_{VI}}\Delta b_{VI} + \frac{\partial\epsilon_{I,k}}{\partial g_{VI}}\Delta g_{VI} + \frac{\partial\epsilon_{I,k}}{\partial a_C}\Delta a_C + \frac{\partial\epsilon_{I,k}}{\partial a_S}\Delta a_S + \frac{\partial\epsilon_{I,k}}{\partial f_{TID}}\Delta f_{TID} + \frac{\partial\epsilon_{I,k}}{\partial b}\Delta b \quad (6.7)$$

where  $\Delta$  represents the difference between a parameter's true and nominal values. As an example,  $\Delta b_{VI} = b_{VI} - b_{VI,0}$  (where  $b_{VI}$  is the true value and  $b_{VI,0}$  is the nominal, or estimated, value that will be refined throughout the estimation).

The partial derivatives given in equation 6.7 for the  $i^{th}$  iteration of the Newton-Raphson method at epoch  $k$  are as follows:

$$\begin{aligned} \frac{\partial\epsilon_{I,k}}{\partial b_{VI}} &= c_{OB,k} & \frac{\partial\epsilon_{I,k}}{\partial g_{VI}} &= c_{OB,k} \cdot d_{IPP,k} & \frac{\partial\epsilon_{I,k}}{\partial b} &= 1 \\ \frac{\partial\epsilon_{I,k,i}}{\partial a_C} &= c_{OB,k} \cos(2\pi \cdot f_{TID,i} \cdot d_{IPP,k}) & \frac{\partial\epsilon_{I,k,i}}{\partial a_S} &= c_{OB,k} \sin(2\pi \cdot f_{TID,i} \cdot d_{IPP,k}) \\ \frac{\partial\epsilon_{I,k,i}}{\partial f_{TID}} &= 2\pi c_{OB,k} a_{S,i} d_{IPP,k} \cos(2\pi \cdot f_{TID,i} \cdot d_{IPP,k}) \\ & & & - 2\pi c_{OB,k} a_{C,i} d_{IPP,k} \sin(2\pi \cdot f_{TID,i} \cdot d_{IPP,k}) \end{aligned}$$

For the first iteration of the method, the model is linearized about a nominal state vector,  $\mathbf{x}_0$ . This vector contains the initial guesses for the states to be estimated, which will be updated throughout the estimation procedure. These initial guesses are denoted as

$b_{VI,0}$ ,  $g_{VI,0}$ ,  $a_{C,0}$ ,  $a_{S,0}$ , and  $f_{TID,0}$  (these values are defined in table 6.2). This gives  $\mathbf{x}_0$  the form:

$$\mathbf{x}_0 = [b_{VI,0} \quad g_{VI,0} \quad a_{C,0} \quad a_{S,0} \quad f_{TID,0} \quad b_0]^T$$

Equations 6.6 and 6.7 constitute a linear model for the ionospheric delay term which is inserted into last term on the right hand side of equation 4.14.

Stacking measurements collected every 30 seconds over the sample period yields the system given by equation 6.8 (considering epochs 1 to  $n$  at iteration  $i$ ). Equation 6.8 is used to evaluate the change in the estimates of the model parameters from one iteration to the next. For instance, at iteration  $i$ :

$$\Delta b_{VI,i} = b_{VI,i} - b_{VI,i-1}$$

Equation 6.8 follows as:

$$\begin{bmatrix} z_{1,i} \\ \vdots \\ z_{n,i} \end{bmatrix} = \begin{bmatrix} z_1(\mathbf{x}_{i-1}) \\ \vdots \\ z_n(\mathbf{x}_{i-1}) \end{bmatrix} + \begin{bmatrix} \frac{\partial \epsilon_{I,1}}{\partial b_{VI}} & \frac{\partial \epsilon_{I,1}}{\partial g_{VI}} & \frac{\partial \epsilon_{I,1,i}}{\partial a_C} & \frac{\partial \epsilon_{I,1,i}}{\partial a_S} & \frac{\partial \epsilon_{I,1,i}}{\partial f_{TID}} & \frac{\partial \epsilon_{I,1}}{\partial b} \\ \vdots & \vdots & \vdots & \vdots & \vdots & \vdots \\ \frac{\partial \epsilon_{I,n}}{\partial b_{VI}} & \frac{\partial \epsilon_{I,n}}{\partial g_{VI}} & \frac{\partial \epsilon_{I,n,i}}{\partial a_C} & \frac{\partial \epsilon_{I,n,i}}{\partial a_S} & \frac{\partial \epsilon_{I,n,i}}{\partial f_{TID}} & \frac{\partial \epsilon_{I,n}}{\partial b} \end{bmatrix} \begin{bmatrix} \Delta b_{VI,i} \\ \Delta g_{VI,i} \\ \Delta a_{C,i} \\ \Delta a_{S,i} \\ \Delta f_{TID,i} \\ \Delta b_i \end{bmatrix} + \begin{bmatrix} v_1 \\ \vdots \\ v_n \end{bmatrix} \quad (6.8)$$

where:

$$\Delta b_i = f_p \cdot \Delta b'_i$$

$$v_k = f_p \cdot v'_k$$

The coefficient  $f_p$  is defined by equation 4.13. The variables  $b'$  and  $v'_k$  are also defined in chapter 4.

It is to be noted that the vector  $[z_1(\mathbf{x}_{i-1}) \quad \cdots \quad z_n(\mathbf{x}_{i-1})]^T$  is not a vector of measurements. Each element of this vector results from substituting the previous state estimates ( $\mathbf{x}_{i-1}$ ) into the sinusoidal model of equation 6.5, such that:

$$z_k(\mathbf{x}_{i-1}) = c_{OB,k}(b_{VI,i-1} + d_{IPP,k} \cdot g_{VI,i-1} + a_{C,i-1} \cos(2\pi f_{TID,i-1} d_{IPP,k}) \\ + a_{S,i-1} \sin(2\pi f_{TID,i-1} d_{IPP,k})) + b_{i-1}$$

where  $k$  varies from 1 to  $n$ , the total number of epochs.

Since the first vector on the right hand side of equation 6.8 is entirely known, it can be brought to the left hand side and absorbed into the measurement vector, yielding the system:

$$\begin{bmatrix} \Delta z_{1,i} \\ \vdots \\ \Delta z_{n,i} \end{bmatrix} = \begin{bmatrix} \frac{\partial \epsilon_{I,1}}{\partial b_{VI}} & \frac{\partial \epsilon_{I,1}}{\partial g_{VI}} & \frac{\partial \epsilon_{I,1,i}}{\partial a_C} & \frac{\partial \epsilon_{I,1,i}}{\partial a_S} & \frac{\partial \epsilon_{I,1,i}}{\partial f_{TID}} & \frac{\partial \epsilon_{I,1,i}}{\partial b} \\ \vdots & \vdots & \vdots & \vdots & \vdots & \vdots \\ \frac{\partial \epsilon_{I,n}}{\partial b_{VI}} & \frac{\partial \epsilon_{I,n}}{\partial g_{VI}} & \frac{\partial \epsilon_{I,n,i}}{\partial a_C} & \frac{\partial \epsilon_{I,n,i}}{\partial a_S} & \frac{\partial \epsilon_{I,n,i}}{\partial f_{TID}} & \frac{\partial \epsilon_{I,n,i}}{\partial b} \end{bmatrix} \begin{bmatrix} \Delta b_{VI,i} \\ \Delta g_{VI,i} \\ \Delta a_{C,i} \\ \Delta a_{S,i} \\ \Delta f_{TID,i} \\ \Delta b_i \end{bmatrix} + \begin{bmatrix} v_1 \\ \vdots \\ v_n \end{bmatrix} \quad (6.9)$$

where:

$$\Delta z_{k,i} = f_p \cdot (\lambda_{L1} \phi_{L1,k} - \lambda_{L2} \phi_{L2,k}) - z_k(\mathbf{x}_{i-1})$$

Equation 6.9 is the measurement system as given by equations 4.16 and 4.17 (i.e.,  $\mathbf{z}_{Meas} = \mathbf{H}_{Meas}\mathbf{x} + \mathbf{v}_{Meas}$ ). The measurement noise covariance matrix,  $\mathbf{V}_{Meas}$ , for this system is identical to the one given in equation 4.23.

Augmentation of the measurement vector  $\mathbf{z}_{Meas}$  with pseudo-observations is employed for all states except the inter-frequency and cycle ambiguity bias term,  $b$ . This is because no prior knowledge is available for this state. Measurement augmentation is performed in the same way as described in chapter 4 except that now changes in the states are estimated (denoted as  $\Delta$ ). This leads to the system below:

$$\begin{bmatrix} 0 \\ 0 \\ 0 \\ 0 \\ 0 \end{bmatrix} = \begin{bmatrix} 1 & 0 & 0 & 0 & 0 & 0 \\ 0 & 1 & 0 & 0 & 0 & 0 \\ 0 & 0 & 1 & 0 & 0 & 0 \\ 0 & 0 & 0 & 1 & 0 & 0 \\ 0 & 0 & 0 & 0 & 1 & 0 \end{bmatrix} \begin{bmatrix} \Delta b_{VI,i} \\ \Delta g_{VI,i} \\ \Delta a_{C,i} \\ \Delta a_{S,i} \\ \Delta f_{TID,i} \\ \Delta b_i \end{bmatrix} + \begin{bmatrix} v_{b_{VI,0}} \\ v_{g_{VI,0}} \\ v_{a_{C,0}} \\ v_{a_{S,0}} \\ v_{f_{TID,0}} \end{bmatrix} \quad (6.10)$$

Equation 6.10 is the pseudo-measurement system given by equations 4.18 and 4.19 (i.e.,  $\mathbf{z}_{Aug} = \mathbf{H}_{Aug}\mathbf{x} + \mathbf{v}_{Aug}$ ) for the original linear vertical delay model. Since the values of the states used as prior knowledge (Table 6.2) are assumed to be the best available values for the states, the pseudo-measurements of the states errors on the left hand side of equation 6.10 are zero. The uncertainty in these values is captured in the pseudo-measurement error vector (i.e., the second term on the right hand side of equation 6.10).

The measurement noise covariance matrix,  $\mathbf{V}_{Aug}$ , for the system of equation 6.10 is given by:

$$\mathbf{V}_{Aug} = \begin{bmatrix} \sigma_{b_{VI,0}}^2 & 0 & 0 & 0 & 0 \\ 0 & \sigma_{g_{VI,0}}^2 & 0 & 0 & 0 \\ 0 & 0 & \sigma_{a_{C,0}}^2 & 0 & 0 \\ 0 & 0 & 0 & \sigma_{a_{S,0}}^2 & 0 \\ 0 & 0 & 0 & 0 & \sigma_{f_{TID,0}}^2 \end{bmatrix} \quad (6.11)$$

Equations 6.9 and 6.10 are combined to produce the final system needed for model validation as given by equation 4.20:

$$\mathbf{z} = \begin{bmatrix} \mathbf{z}_{Aug} \\ \mathbf{z}_{Meas} \end{bmatrix} = \begin{bmatrix} \mathbf{H}_{Aug} \\ \mathbf{H}_{Meas} \end{bmatrix} \mathbf{x} + \begin{bmatrix} \mathbf{v}_{Aug} \\ \mathbf{v}_{Meas} \end{bmatrix} = \mathbf{H}\mathbf{x} + \mathbf{v}$$

The measurement noise covariance matrix,  $\mathbf{V}$ , for this system is the same as given in equation 4.21, namely,

$$\mathbf{V} = \begin{bmatrix} \mathbf{V}_{Aug} & \mathbf{0} \\ \mathbf{0} & \mathbf{V}_{Meas} \end{bmatrix}$$

Table 6.2 contains the prior knowledge on the states which is given to the system. The mean and standard deviation values for  $b_{VI}$  and  $g_{VI}$  are the same as those used in the analysis of quiet days with the original model (Chapter 5).

The amplitudes of the cosine and sine terms,  $a_C$  and  $a_S$ , are set to zero since these values can be positive or negative. In addition, these values are not expected to exceed the decimeter-level based on the observed residual error results using the original model. A conservative standard deviation of one meter is used for the amplitudes.

The initial TID frequency term,  $f_{TID}$ , is obtained by examining segments exhibiting residual waves with the original model. An average IPP displacement for the period of the TID wave is determined from these segments. The standard deviation for the prior knowledge on the frequency term is deliberately set small. This forces the estimator to converge on a value near the initial guess. The frequency value is constrained to be near the initial guess due to observability issues. This is because convergence of the sine wave to multipath (at higher frequencies) or to biases (at lower frequencies) must be avoided.

Since no prior knowledge about the inter-frequency and cycle ambiguity bias term,  $b$ , is available, this value is initially set to zero.

Table 6.2. Prior Knowledge for Sinusoidal Model States

State	Value	Standard Deviation
$b_{VI,0}$ (m)	2	3
$g_{VI,0}$ (m/km)	0	$5 \times 10^{-3}$
$a_{C,0}$ (m)	0	1
$a_{S,0}$ (m)	0	1
$f_{TID,0}$ (1/km)	$3.33 \times 10^{-3}$	$5 \times 10^{-4}$
$b_0$ (m)	0	N/A

As mentioned earlier, the  $b_{VI,0}$ ,  $g_{VI,0}$ ,  $a_{C,0}$ ,  $a_{S,0}$ ,  $b_0$ , and  $f_{TID,0}$  values given in table 6.2 are the quantities for each state about which the model is linearized for the first iteration of the Newton-Raphson method.

For the  $i^{th}$  iteration of the Newton-Raphson method, the residual measurement vector,  $\mathbf{r}_i$ , is computed from:

$$\mathbf{r}_i = [\Delta b_{VI,i} \quad \Delta g_{VI,i} \quad \Delta a_{C,i} \quad \Delta a_{S,i} \quad \Delta f_{TID,i} \quad \Delta z_{1,i} \quad \dots \quad \Delta z_{n,i}]^T \quad (6.12)$$

The current state estimates (values about which the system is linearized),  $\mathbf{x}_i$ , are updated according to:

$$\mathbf{x}_i = \mathbf{x}_{i-1} + \Delta \mathbf{x}_i \quad (6.13)$$

with:

$$\Delta \mathbf{x}_i = (\mathbf{H}_i^T \mathbf{V}^{-1} \mathbf{H}_i)^{-1} \mathbf{H}_i^T \mathbf{V}^{-1} \mathbf{r}_i \quad (6.14)$$

The residual measurement vector is also used to calculate the normalized residual:

$$J_i = \mathbf{r}_i^T \mathbf{V}^{-1} \mathbf{r}_i \quad (6.15)$$

Convergence is attained if the difference between the quantity of equation 6.15 for successive iterations does not exceed a convergence threshold,  $\epsilon$ . In other words, convergence is achieved if:

$$|J_{i+1} - J_i| < \epsilon \quad (6.16)$$

For this analysis, the value of  $\epsilon$  is 0.007. This convergence threshold has been evaluated considering the following tradeoff: It must be loose enough to ensure convergence for cases where TIDs do not exist (i.e., in the presence of measurement noise), but it must also be tight enough to ensure reasonable state estimates.

The process described above is repeated until convergence is reached. If convergence is not achieved for a segment within a certain number of iterations, the

estimation is stopped and the information about the segment is stored before moving to the next segment. These non-converging segments will be analyzed to see what the residual variation looks like after all segments have been evaluated.

The maximum number of iterations for the estimation procedure is set at 300 based on observations from the data. In determining the number of iterations that should be used, it has been observed that there exist cases where only measurement noise is present that require many more iterations to converge as compared to those where a TID wave exists in the data (the maximum number of iterations found for 700-800 km-long segments is 289). It has also been determined that increasing the number of iterations above 300 does not achieve a greater percentage of converging segments. Therefore, although this large number of iterations is computationally inefficient, it helps to ensure that convergence is obtained for as many segments as possible for the purposes of model evaluation.

**6.2.1 Results with the Sinusoidal Model.** In the same way as the quadratic model, the results of applying the sinusoidal model will be presented in comparison to the results with the original model for quiet days. This allows for a direct assessment between the largest residual magnitudes between the original and sinusoidal vertical delay models.

The sinusoidal model is applied to 57,478 segments with maximum IPP displacements between 700 km and 800 km. It is found that 168 (0.29%) of these segments do not converge. These non-converging segments will be discussed later. First, the results of the 57,310 converging segments will be studied.

Several example cases are shown below which compare the residual variations generated by the original and sinusoidal models. Figures 6.6, 6.7, and 6.8 show instances

where wave amplitudes exceed 10 cm in the residual variation using the original vertical delay model. Residuals in figures 6.7 and 6.8 are among the largest observed with the original model. It is obvious in these figures that after applying the sinusoidal vertical delay model, residual magnitudes are significantly reduced.

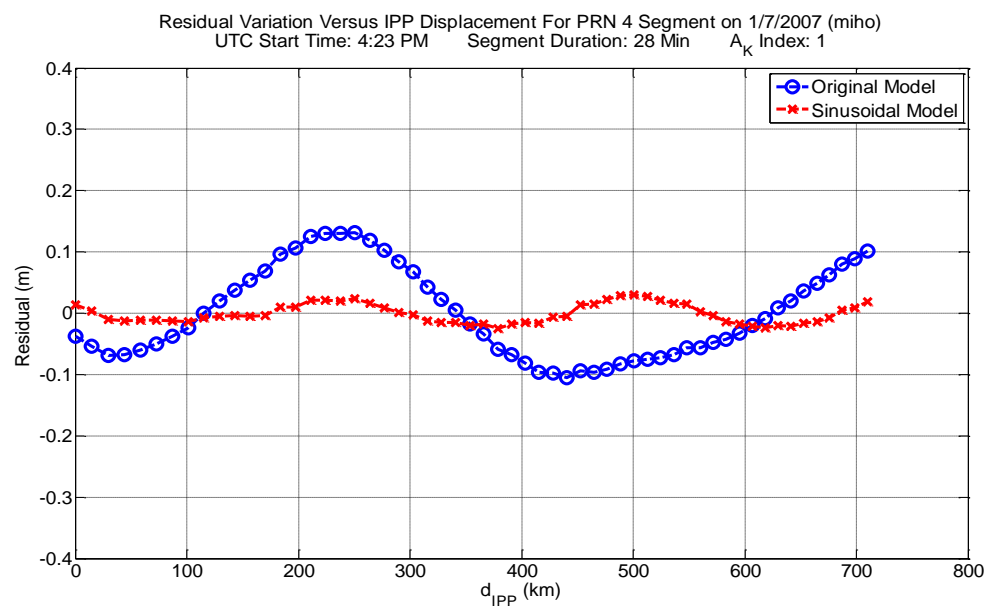


Figure 6.6. Original and Sinusoidal Model Comparison at Holland, Michigan

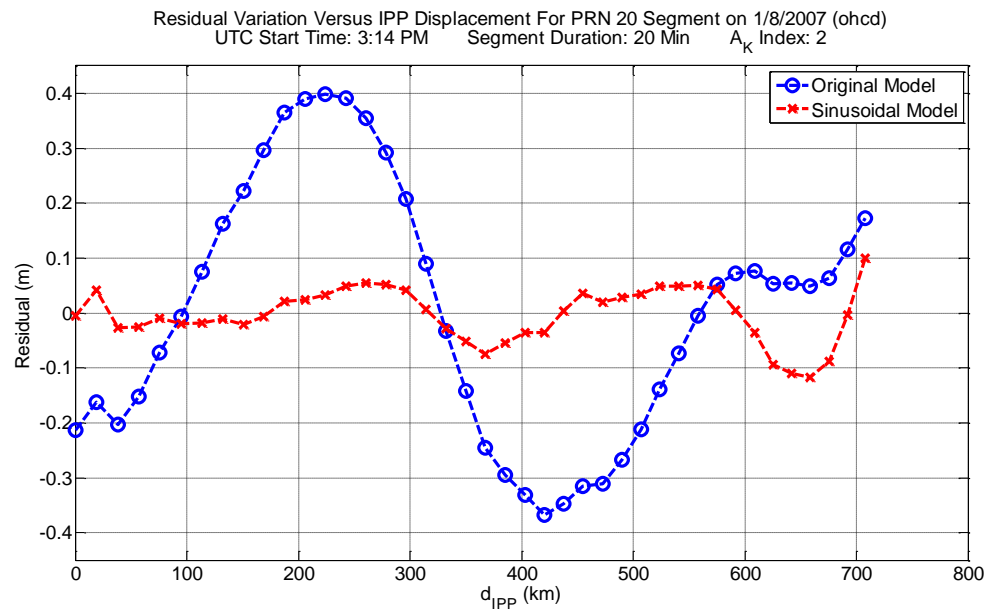


Figure 6.7. Original and Sinusoidal Model Comparison at Cleveland, Ohio

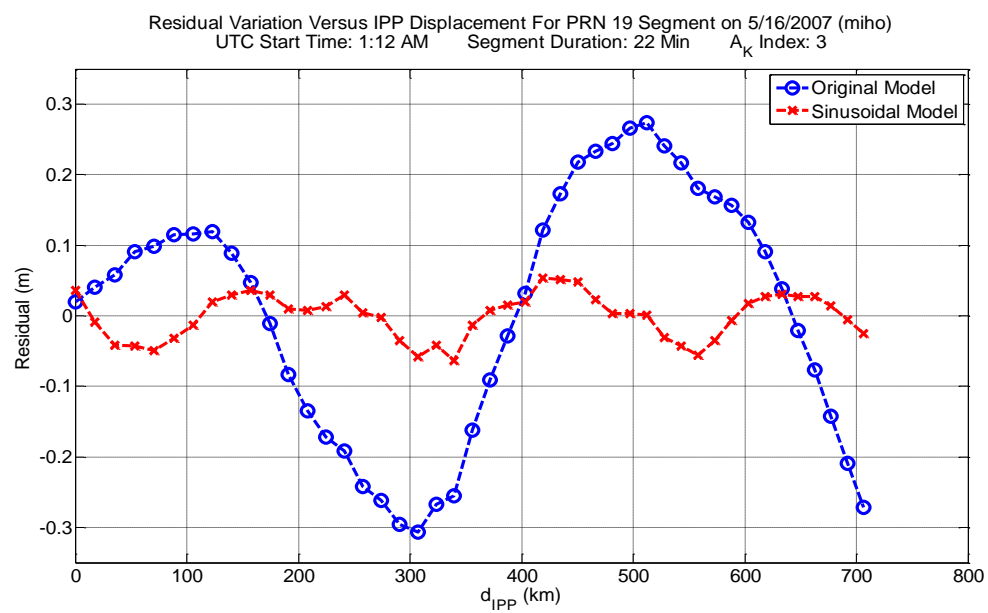


Figure 6.8. Original and Sinusoidal Model Comparison at Holland, Michigan

Examples shown in figures 6.9 and 6.10 verify that the sinusoidal model matches the results of the original model when TID waves are not present.

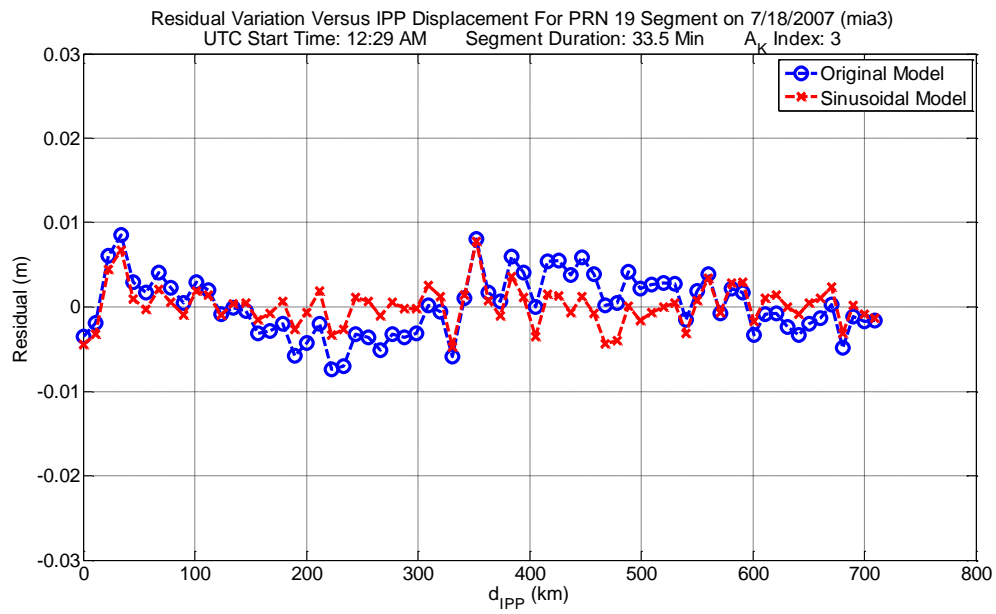


Figure 6.9. Original and Sinusoidal Model Comparison at Miami, Florida

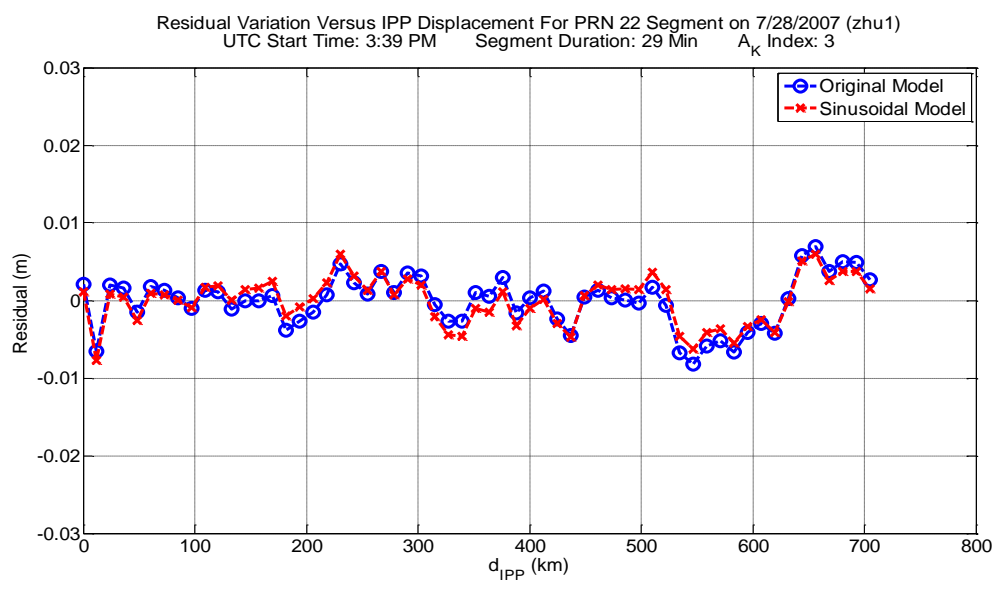


Figure 6.10. Original and Sinusoidal Model Comparison at Houston, Texas

Figure 6.11 displays an instance where a TID wave exists in the residual variation of the original model. The single sinusoid model does not offer much improvement in this case because the error variations exhibit multiple frequencies and amplitudes. As a result, the maximum residual magnitudes with the sinusoidal model are nearly identical to that of the original model.

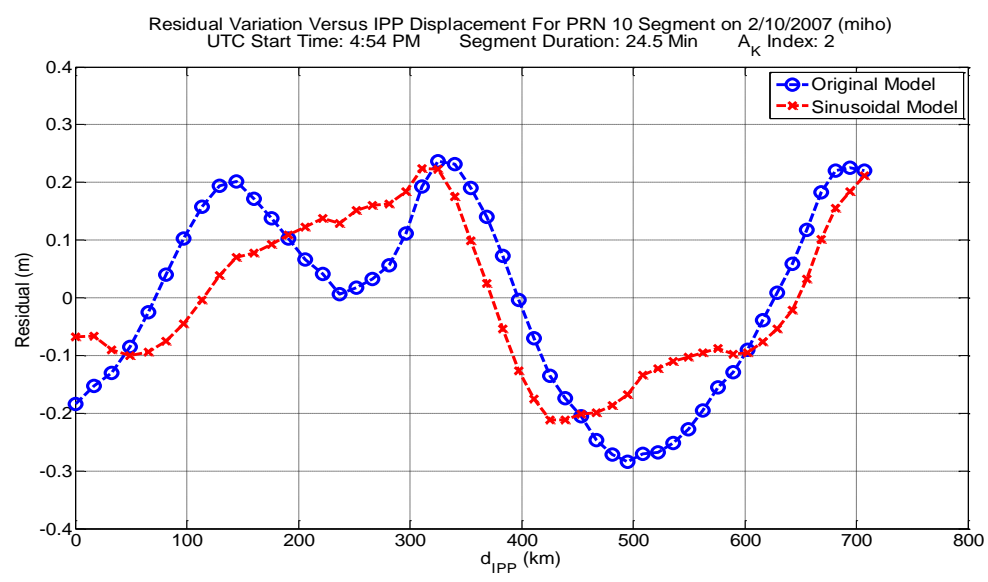


Figure 6.11. Original and Sinusoidal Model Comparison at Holland, Michigan

The folded residual error CDF for the sinusoidal model is constructed for comparison with that of the original model. Figure 6.12 displays the folded residual CDFs for both the original and sinusoidal vertical delay models.

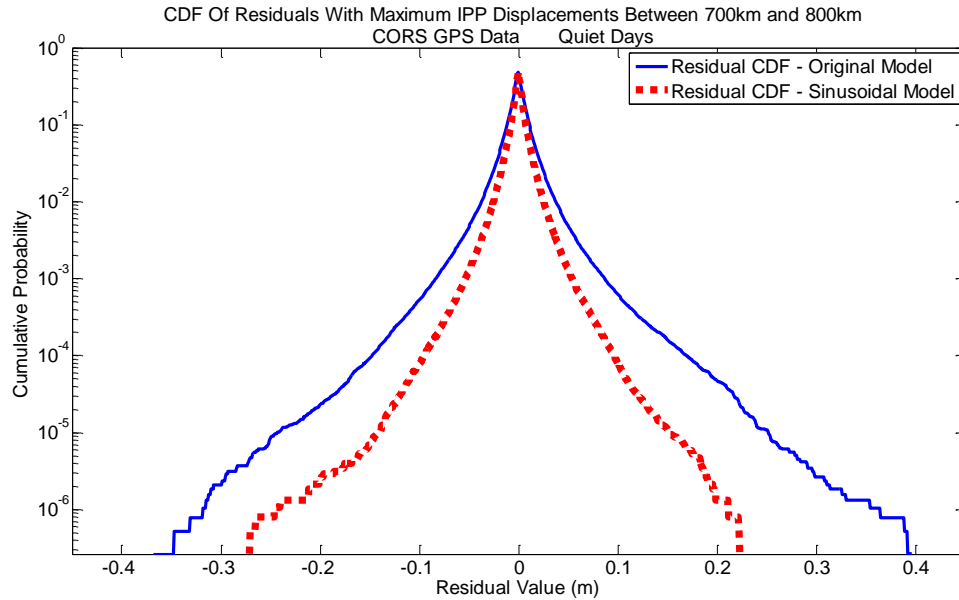


Figure 6.12. Comparison of Folded Residual CDFs for Original and Sinusoidal Models

The result of figure 6.12 shows that the sinusoidal model tightens the tails of the residual error distribution. For the original model, the maximum residual is 39.76 cm while the sinusoidal model yields a maximum residual of 27.43 cm. The standard deviation of the Gaussian distribution over-bounding the residuals is also improved by the sinusoidal model. This standard deviation is reduced from 8.2 cm with the original model to 5.7 cm with the sinusoidal model.

Estimated parameter values for the states of the sinusoidal model are shown in table 6.3. These values are based on results with converging segments. The values obtained for  $b_{VI}$  and  $g_{VI}$  are comparable with the ones computed with the original model (Table 5.3). Estimated values and standard deviations of the TID state ( $a_C$ ,  $a_S$ , and  $f_{TID}$ ) values are reasonable based on observations of the data.

Table 6.3. Estimated Parameter Values for Quiet Ionospheric Days with Sinusoidal Error Model

State	Mean Value	Standard Deviation
$b_{VI}$ (m)	1.27	6.45
$g_{VI}$ (m/km)	$2.5 \times 10^{-6}$	$1.99 \times 10^{-3}$
$a_C$ (m)	$-1.34 \times 10^{-4}$	0.0385
$a_S$ (m)	$2.28 \times 10^{-4}$	0.0371
$f_{TID}$ (1/km)	$3.19 \times 10^{-3}$	$5.11 \times 10^{-4}$

Although the sinusoidal model offers improvement in terms of residual magnitudes and the over-bounding standard deviation, there still exist residuals greater than 20 cm. In addition, the over-bounding standard deviation with the sinusoidal model is more than twice the measurement noise standard deviation of 2.3 cm. This means both the residual magnitudes and over-bounding standard deviation need to be reduced much further in order to produce a good match with the data. This could be accomplished in a number of ways.

One approach to account for these large residual magnitudes is to employ an error model with other basis functions. Examples of possible basis functions include adding two sinusoids with different frequencies, an exponentially-modulated sinusoid, or more generally, a series of orthogonal basis functions, such as a Fourier series. However, using these more elaborate basis functions might still not be sufficient. Although it is true that by adding enough terms to the model it can be made to fit the data nearly perfectly, there are consequences for adding these terms. While the addition of more terms means that high integrity can be achieved by accurately capturing the errors, these terms will make the model introduce more uncertainty into the positioning solution, thereby decreasing system availability.

In addition to adding more terms to the model, it can also be argued that applying the model over much smaller IPP displacements than the 700-800 km considered would significantly decrease residual magnitudes. There are consequences to this approach on positioning. From figure 5.2, is apparent that system availability decreases quickly if the model is applied over maximum IPP displacements of 600 km or less. This means that even though the model may fit the data well over smaller distances, it is done at the cost of reducing system availability and subsequently the ability of the navigation system to provide precise positioning.

The constraints of limiting the number of states in the error model and the IPP displacement over which the model can be applied point to the fact that it is a challenge to employ a single error model that will capture the variation in ionospheric errors effectively for all cases.

An alternative approach to account for large residual magnitudes is to use the original linear vertical delay model exclusively. This would eliminate the need to include additional parameters. The issue of non-convergence with the sinusoidal model would also be eliminated. However, since the residual errors are larger with the original model as compared to the sinusoidal model, their impact on positioning will have to be investigated more thoroughly in future work.

**6.2.2 Non-Converging Segments with the Sinusoidal Model.** As stated earlier, the sinusoidal model does not converge in 168 cases. Examples of the residual error variation for some of these non-converging cases are shown below in figures 6.13-6.15. The residual variations in the figures are generated with the original linear vertical delay model. This is done to show the shape of the residual variations that the sinusoidal model

is unable to track. Figure 6.15 contains the largest residual of the cases that do not converge. This maximum residual has a magnitude of 24.29 cm.

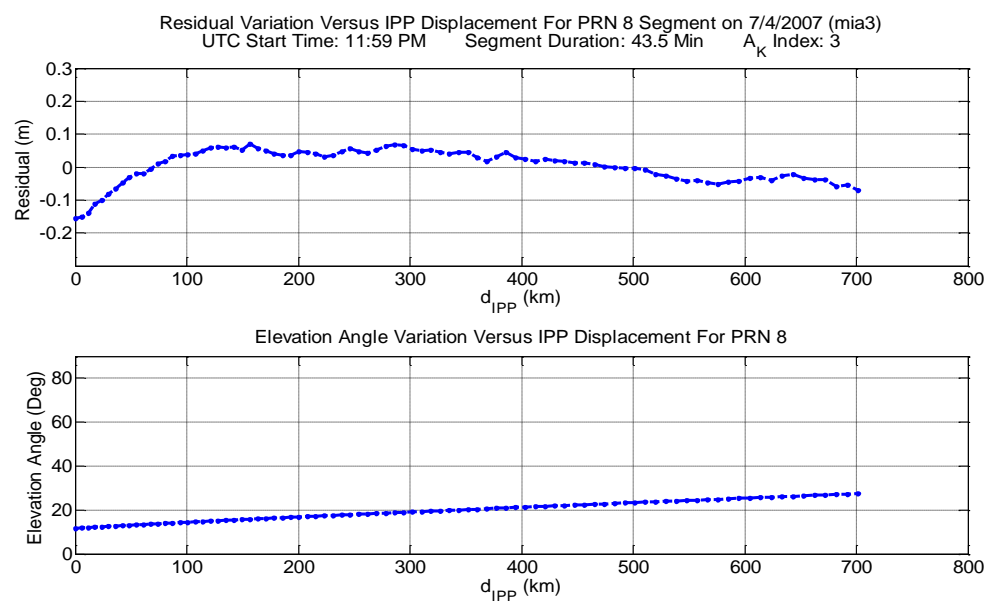


Figure 6.13. Non-Converging Segment at Miami, Florida

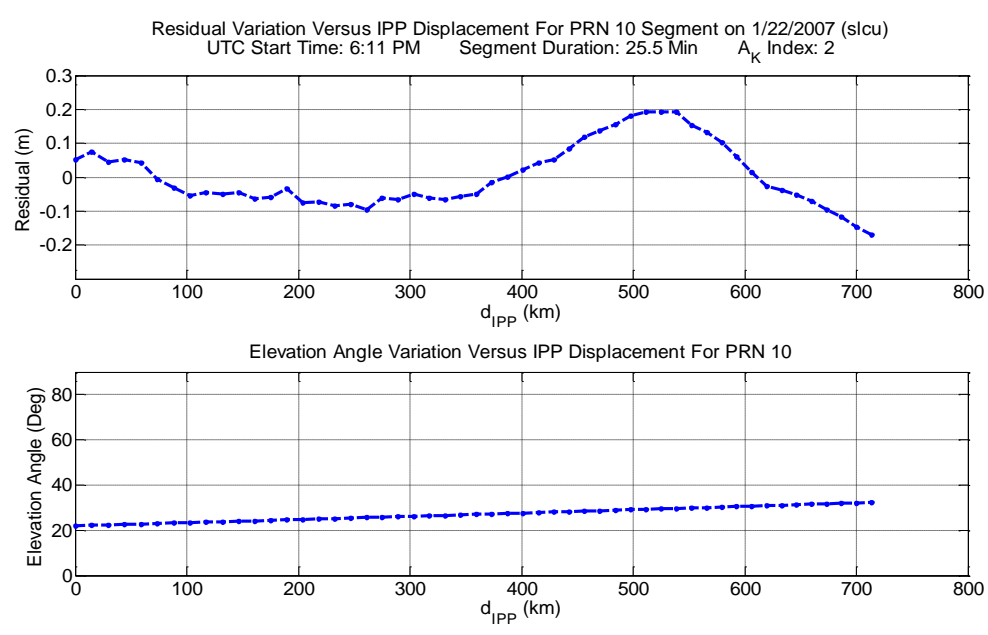


Figure 6.14. Non-Converging Segment at Salt Lake City, Utah

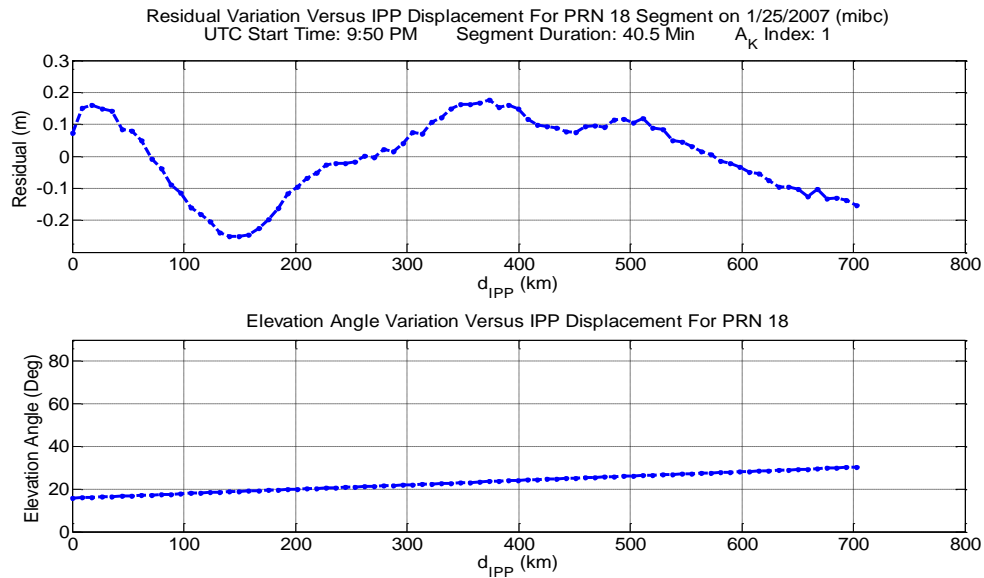


Figure 6.15. Non-Converging Segment at Battle Creek, Michigan

It is evident from these examples that a single sinusoid is not sufficient to capture all of the structures in these residual variations. This is observed not only in the non-converging segments, but also in converging cases where the sinusoidal model offers little or no improvement (Figure 6.11). There are cases for both converging and non-converging segments where residual magnitudes of 20 cm or more are present. These large magnitudes indicate that the sinusoidal model does not completely solve the issue of producing centimeter-level residuals.

Up to this point, only GPS data has been used to evaluate the model. Since the model is meant to be employed for GPS and LEO satellite measurements, it must also be evaluated with LEO data. This LEO analysis, which is carried out in the next chapter, will help to verify the results obtained with GPS data.

## CHAPTER 7

### MODEL EVALUATION USING LOW EARTH ORBIT DATA

The evaluation of the ionospheric error model, which is intended for both GPS and LEO satellite measurements, was based solely on GPS data in chapters 5 and 6. To verify the results obtained with GPS data, the model is tested using low earth orbit satellite data. Two different types of data are used: simulated ionospheric delays and actual delay measurements from a variety of LEO satellites currently in orbit.

#### 7.1 Simulated Data

Simulated ionospheric delays affecting Iridium signals have been provided by Dr. Seebany Datta-Barua of the Atmospheric and Space Technology Research Associates. These delays are simulated for Miami, Florida on August 5, 2009 using the International Reference Ionosphere (IRI) model.

The IRI model is a product of the Committee on Space Research and the International Union of Radio Science. Given a specific latitude, longitude, altitude range, and time, the IRI model provides information about the electron density and ion composition in the ionosphere. This model is based on data collected over many years through a wide array of ground and space based tools. More detailed information about the IRI model can be found in [19].

The ionospheric delays at the GPS L1 frequency generated with the IRI model are designated as  $z_{L1}$ . These L1 delays need to be converted to a delay for Iridium, denoted as  $z_{IRID}$ . The conversion is accomplished through the following:

$$z_{IRID,k} = \frac{f_{L1}^2}{f_{IRIDIUM}^2} \cdot z_{L1,k} \quad (7.1)$$

where  $f_{L1}$  is the frequency of the GPS L1 signal (1575.42 MHz) and  $f_{IRIDIUM}$  is the frequency of the Iridium signal (1624 MHz).

The  $z_{L1}$  measurements are obtained at 30 second intervals for times when the satellites are visible at the location of interest. Due to the short orbital periods of LEO spacecraft, data from each satellite is available multiple times throughout the day.

Model evaluation follows the same procedure as the original model of chapter 5 and the quadratic model of chapter 6, namely using least-squares estimation with pseudo-measurement augmentation to determine residual errors and parameter values. Since this data is simulated, the inter-frequency and cycle ambiguity bias term,  $b$ , does not need to be estimated. This is because the data is free of biases and other irregularities, such as TIDs, that are present in actual data. In addition, there are no multipath errors present in the data.

Another consequence of using this simulated data is that there is no measurement noise (and subsequently no measurement noise vector,  $\mathbf{v}$  and covariance matrix,  $\mathbf{V}$ ). This means that measurements are not weighted when computing the least-squares state estimate (equation 4.2).

Measurements obtained every 30 seconds (and converted to a delay on Iridium) are stacked until the IPP displacement reaches the desired range between 700 km and 800 km. Equation 7.2 shows the system of equations generated by stacking measurements.

$$\begin{bmatrix} z_{IRID,1} \\ \vdots \\ z_{IRID,n} \end{bmatrix} = \begin{bmatrix} c_{OB,1} & c_{OB,1} \cdot d_{IPP,1} \\ \vdots & \vdots \\ c_{OB,n} & c_{OB,n} \cdot d_{IPP,n} \end{bmatrix} \begin{bmatrix} b_{VI} \\ g_{VI} \end{bmatrix} \quad (7.2)$$

**7.1.1 Simulated Data Results.** The error model given in equation 3.1 is applied to segments with maximum IPP displacements between 700 km and 800 km. This

corresponds to 564 segments for the set of data used in this analysis. Due to the limited data available (one day) and the limited amount of time a satellite is visible over the location of interest, a five degree elevation mask is used in order to maximize the amount of data that can be processed. Due to the absence of multipath errors in this simulated data, a low elevation mask can be employed.

Figures 7.1 and 7.2 show examples of residual variations generated from the simulated data where all residuals are below 2.5 cm. These examples show that the model has the ability to produce centimeter-level residuals.

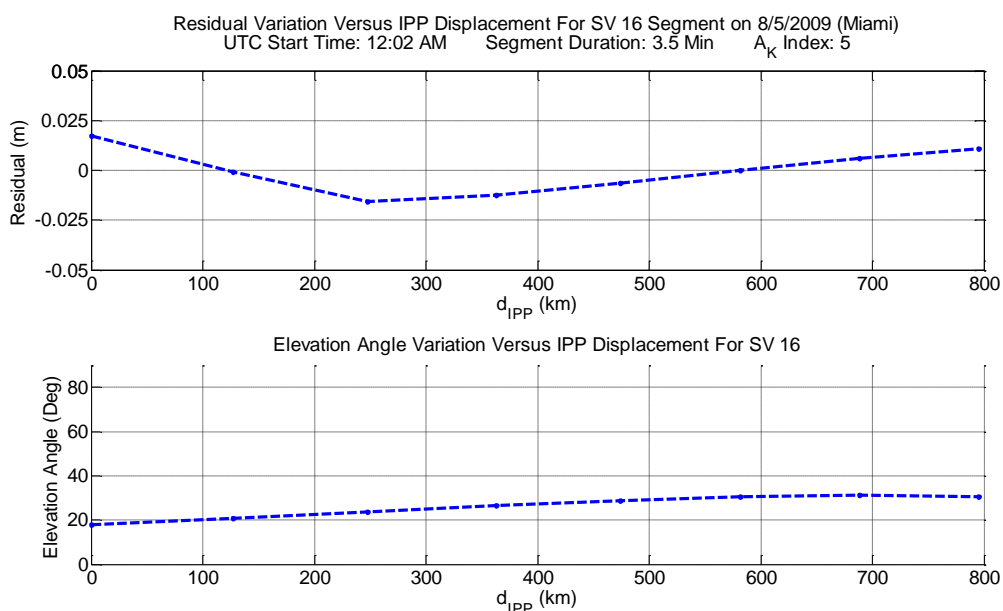


Figure 7.1. Simulated LEO Data Residual Variation - Example 1

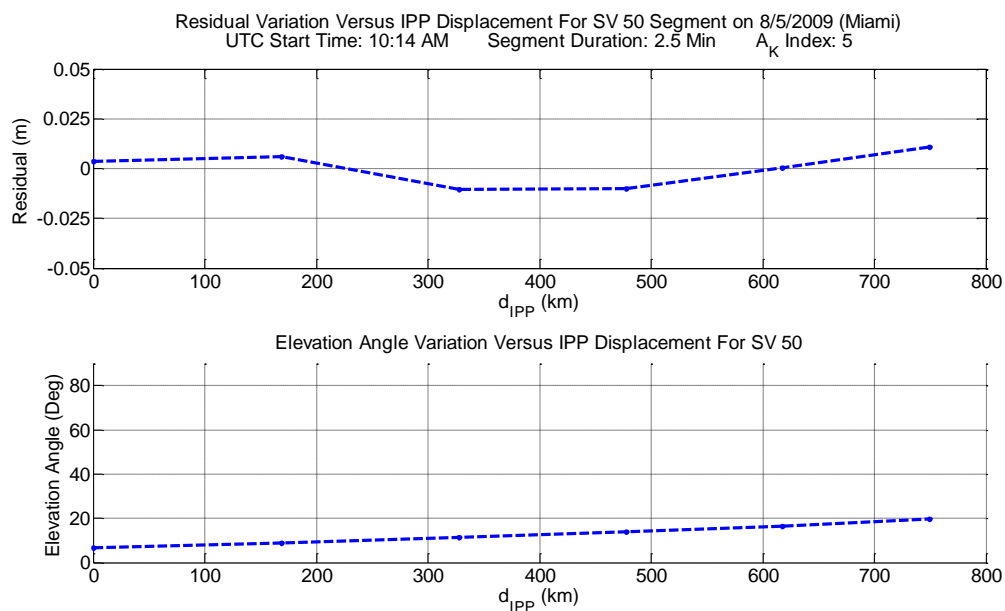


Figure 7.2. Simulated LEO Data Residual Variation - Example 2

A folded residual error CDF (explained in chapter 5) is constructed after applying the model to this simulated data. Figure 7.3 depicts this folded CDF along with the Gaussian function which over-bounds the residual error distribution. This folded CDF contains the 3,887 residuals generated from the 564 segments considered.

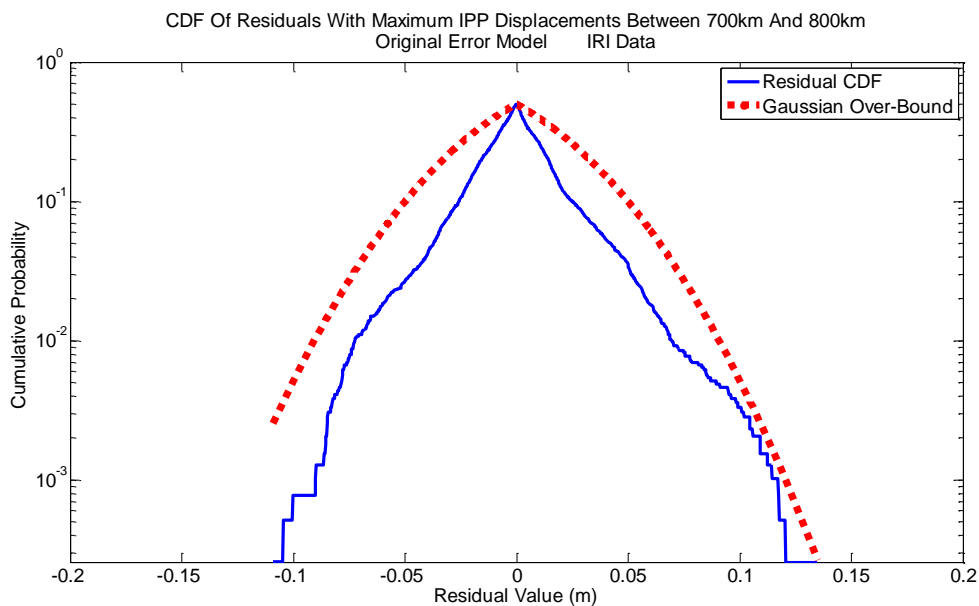


Figure 7.3. Folded Residual CDF for Original Model with Simulated LEO Data

The standard deviation of the Gaussian over-bound is 3.9 cm. Since there is no measurement noise, this value cannot be compared to the measurement noise standard deviation as with the GPS data. Therefore, the residuals obtained after applying the model to this simulated data can only be attributed to mis-modeling errors.

Estimated values and standard deviations of the parameters in the error model have been computed after applying the original model to this simulated data and are shown in table 7.1.

Table 7.1. Estimated Parameter Values for Simulated LEO Data with Original Error Model

State	Mean Value	Standard Deviation
$b_{VI}(\text{m})$	2.45	0.934
$g_{VI}(\text{m/km})$	$5.29 \times 10^{-4}$	$2.95 \times 10^{-4}$

To lower the over-bounding standard deviation (and largest residual magnitudes), segments which produce the largest residual errors are examined.

Figures 7.4 and 7.5 show cases where residual magnitudes exceed 10 cm. The case in figure 7.4 is the segment where the largest residual obtained with the original model is present. This residual profile reaches magnitudes of 13.5 cm.

The decimeter-level residuals observed in figures 7.4 and 7.5 can be attributed to the fact that the satellites from which these residuals are computed are at low elevation angles (below 10 degrees). This means that any mis-modeling of the vertical ionospheric delay is amplified by the large obliquity factor associated with the satellite's low elevation.

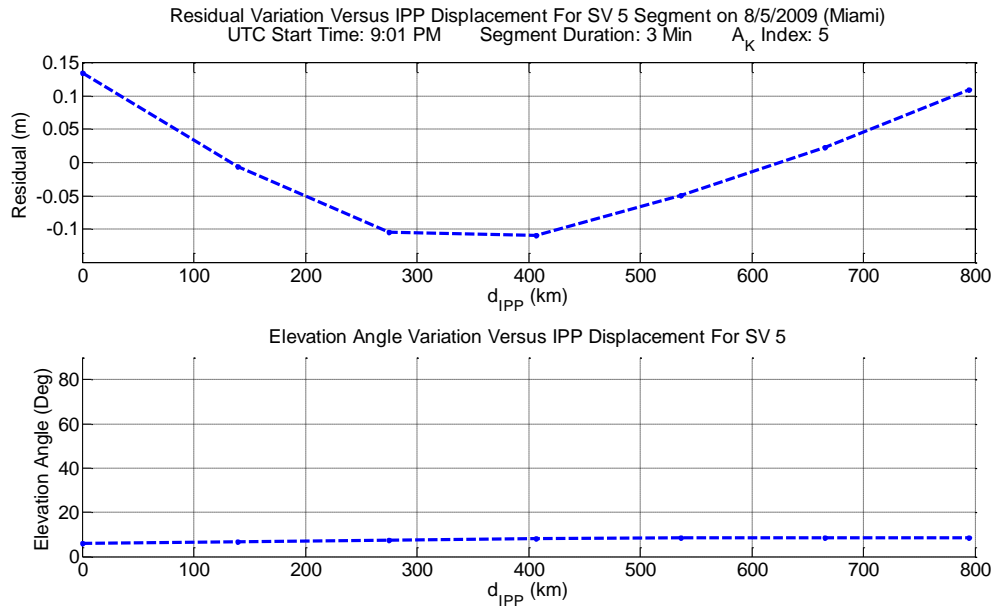


Figure 7.4. Simulated LEO Data Residual CDF Outlier - Example 1

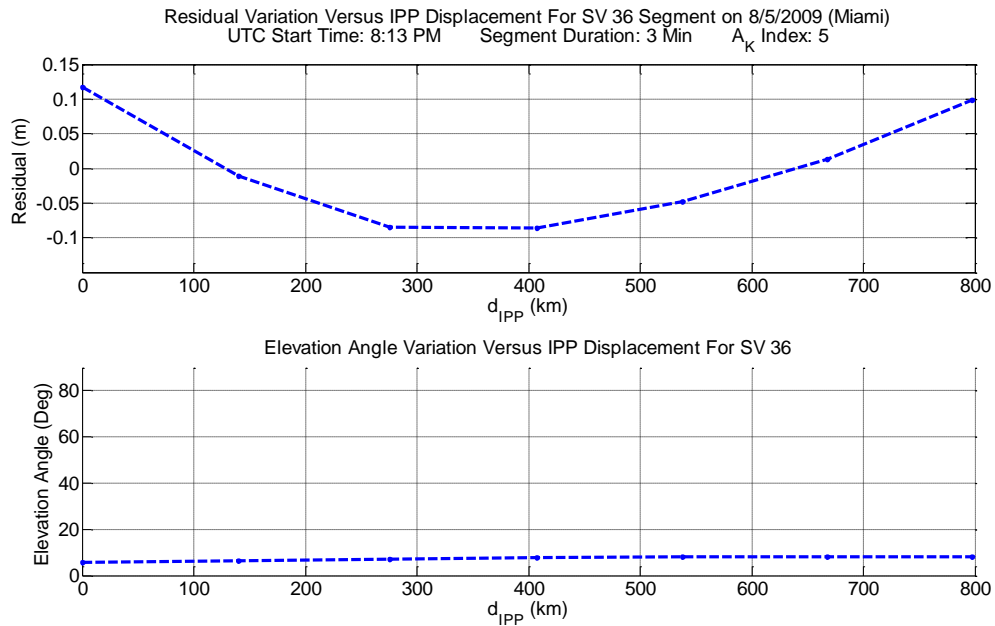


Figure 7.5. Simulated LEO Data Residual CDF Outlier - Example 2

The bow shapes in the residuals of these CDF outlier cases suggest that the quadratic model should be used. Implementation of the quadratic model is performed to determine if residual magnitudes can be reduced. Measurements will be of the form:

$$z_{IRID,k} = \frac{f_{L1}^2}{f_{IRIDIUM}^2} \cdot z_{L1,k} = c_{OB,k} (b_{VI} + d_{IPP,k} \cdot g_{VI} + d_{IPP,k}^2 \cdot q_{VI}) \quad (7.3)$$

where  $q_{VI}$  is the quadratic coefficient which will be estimated along with  $b_{VI}$  and  $g_{VI}$ .

The system of equations for the quadratic model follows as:

$$\begin{bmatrix} Z_{IRID,1} \\ \vdots \\ Z_{IRID,n} \end{bmatrix} = \begin{bmatrix} c_{OB,1} & c_{OB,1} \cdot d_{IPP,1} & c_{OB,1} \cdot d_{IPP,1}^2 \\ \vdots & \vdots & \vdots \\ c_{OB,n} & c_{OB,n} \cdot d_{IPP,n} & c_{OB,n} \cdot d_{IPP,n}^2 \end{bmatrix} \begin{bmatrix} b_{VI} \\ g_{VI} \\ q_{VI} \end{bmatrix} \quad (7.4)$$

The quadratic model is fitted to the simulated data using least-squares estimation in the same way as with the GPS data presented in chapter 6.

Figure 7.6 shows the variation of residuals that result from applying the quadratic model to the outlier case in figure 7.4 where the largest residuals are present. For comparison, the residual variation from the original model is also shown in this figure.

The quadratic model reduces the residuals down to two centimeters or less.

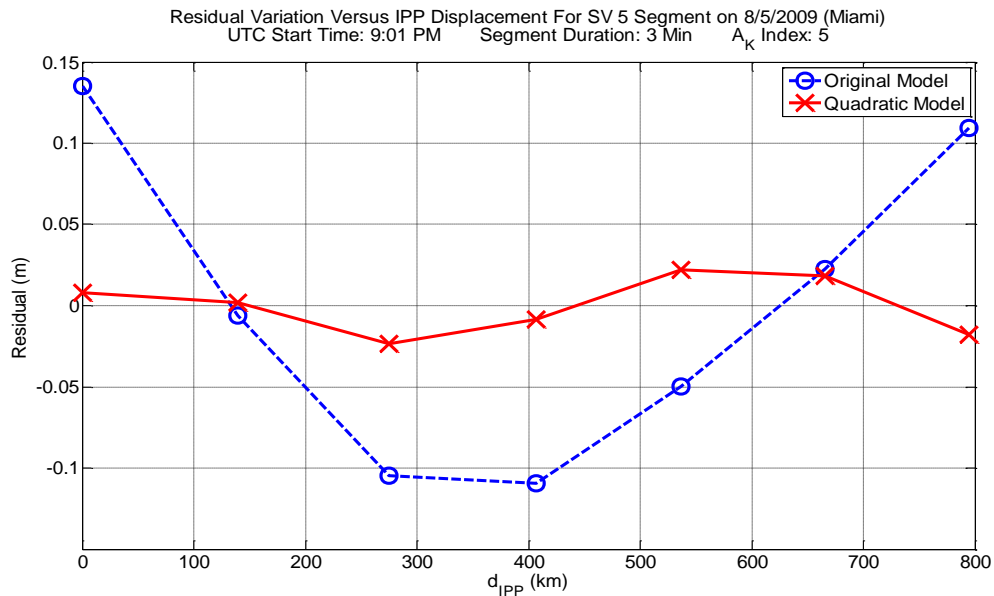


Figure 7.6. Original and Quadratic Model Comparison with Simulated LEO Data

Application of the quadratic model to all 700-800 km segments from all satellites provides the folded residual error CDF plotted in figure 7.7. In addition to the quadratic model folded residual CDF, the original model folded residual CDF is shown for comparison. From the figure, it is apparent that the quadratic model produces no residuals

larger than 10 cm (the maximum residual obtained is 8.3 cm). This decrease in residual magnitudes reduces the tail size of the distribution, compared to the original model. Improvement in the tails is also manifested in the standard deviation of the over-bounding Gaussian distribution. This value is reduced from 3.9 cm with the original model to 2.6 cm with the quadratic model. Although the over-bounding standard deviation has been reduced with the quadratic model, there are still mis-modeling errors since the largest residual magnitudes are greater than eight centimeters.

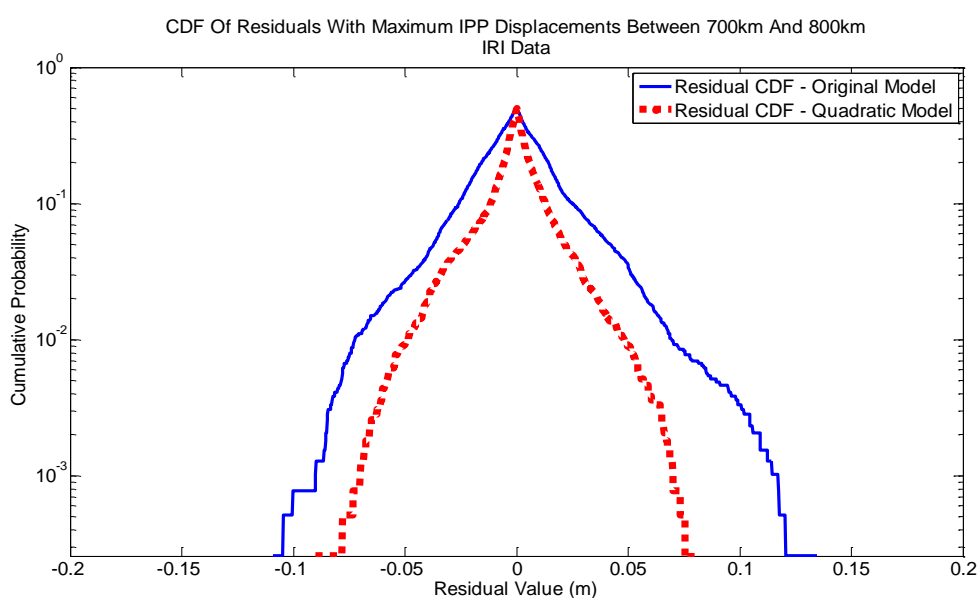


Figure 7.7. Folded Residual CDF Comparison for Original and Quadratic Models with Simulated LEO Data

This simulated data analysis shows that the quadratic model can effectively reduce residual magnitudes in the presence of bow-shaped residual variations.

The estimated parameter values for the states in the quadratic model are given in table 7.2. Mean values and standard deviations for the  $b_{VI}$  and  $g_{VI}$  terms are similar to those obtained with the original model applied to this simulated data.

Table 7.2. Estimated Parameter Values for Simulated LEO Data with Quadratic Error Model

State	Mean Value	Standard Deviation
$b_{VI}(\text{m})$	2.44	0.936
$g_{VI}(\text{m/km})$	$4.98 \times 10^{-4}$	$2.79 \times 10^{-4}$
$q_{VI}(10^{-3} /\text{km})$	$8.28 \times 10^{-11}$	$3.39 \times 10^{-10}$

Since the simulated data is free of biases and irregularities, such as TIDs, a sinusoidal model is not considered as it does not provide a significant benefit beyond that of the quadratic model.

## 7.2 Actual Low Earth Orbit Data

The actual LEO satellite ionospheric delay measurements are provided by Dr. Datta-Barua through Trevor Garner from the Applied Research Laboratory, the University of Texas at Austin. Data is taken by several ground stations across the United States using signals from a number of different LEO satellites. These satellites belong to different systems, including the Constellation Observing System for Meteorology, Ionosphere, and Climate (COSMIC), the Orbiting Satellite Carrying Amateur Radio (OSCAR), and the Radar Calibration (RADCAL) satellite.

Delay measurements are provided as a line-of-sight relative TEC delay, in meters at the L1 frequency. These delays, computed for January 7 and January 23 of 2007 (days of quiet ionospheric activity), are determined from CIDR (Coherent Ionospheric Doppler Receiver) receivers using the 150 MHz and 400 MHz radio beacons carried on these LEO satellites [10].

The ground stations where the data are collected are located over much of the United States. Table 7.3 lists the sites considered in this analysis. It is to be noted that there are two facilities in Austin, Texas where data is obtained.

Table 7.3. Sites used in Actual LEO Data Analysis

Site Location	Site	Site
	Latitude (deg N)	Longitude (deg E)
Boston, Massachusetts	42.35	-71.06
Westford, Massachusetts	42.57	-71.44
Oneonta, New York	42.45	-75.06
Wallops Island, Virginia	37.86	-75.46
Albany, New York	42.49	-76.43
Austin, Texas	30.26	-97.76

The original model (equation 3.1) is used to analyze this data, after applying a ten degree elevation mask and assuming a measurement noise standard deviation of 2.3 cm (caused by receiver noise and multipath). This measurement noise standard deviation is assumed to be the same as GPS data [10]. Evaluation of the model is performed using least-squares estimation with pseudo-measurement augmentation (using the values listed in table 5.2). The estimation procedure is carried out in the same way as with the GPS data in chapter 5, the only difference being that the delay measurements,  $\mathbf{z}_{Meas}$  (equations 4.16 and 4.17), are not multiplied by  $f_p$  (equation 4.13) since the measurements are already provided in terms of L1 delay (relative delay).

Figure 7.8 depicts an example where the residuals are the largest observed with the original model. Residuals in this example are at the decimeter-level (exceeding 25 cm in some cases) and resemble a wave-like structure. The example in figure 7.9 also exhibits a wave structure even though the amplitude is slightly less than 10 cm. These results point out that ionospheric structures are not fully captured by the original model even for short time periods. In most cases, the LEO satellites in this analysis achieve IPP displacements between 700 km and 800 km in three or four minutes. This is in contrast to GPS satellites which typically cover the same IPP displacements in 20 to 40 minutes.

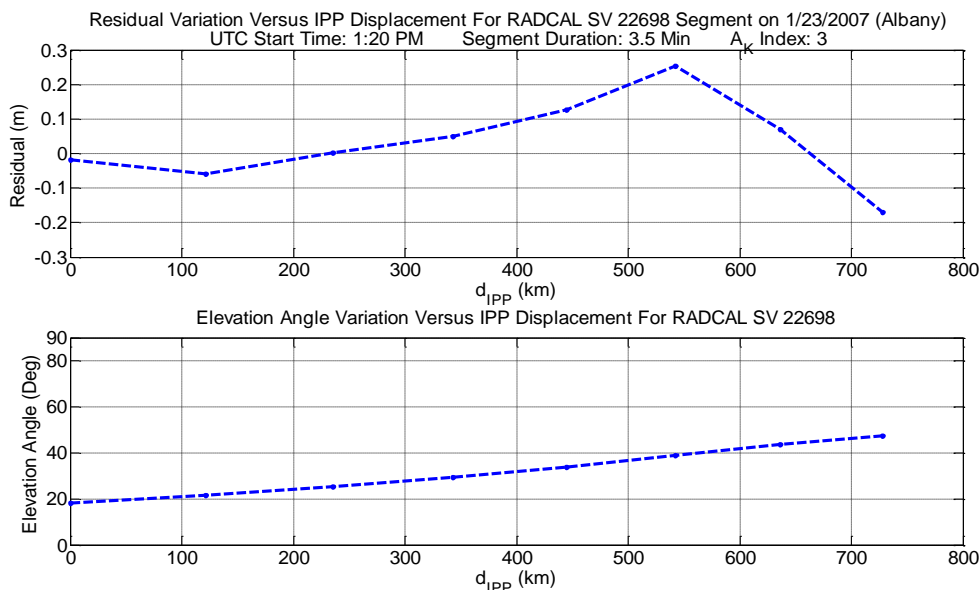


Figure 7.8. Original Model Applied to Actual LEO Data at Albany, New York

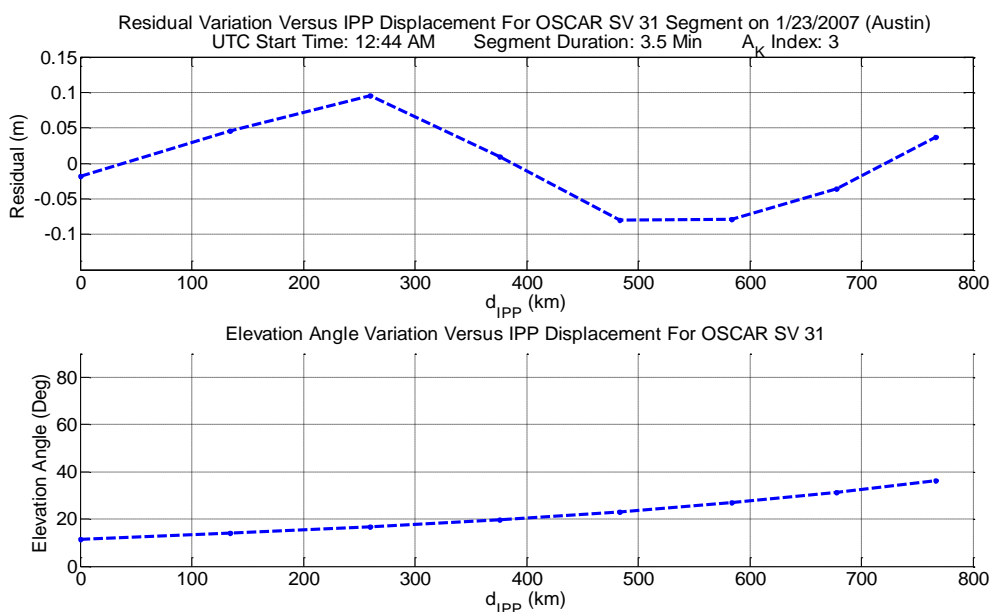


Figure 7.9. Original Model Applied to Actual LEO Data at Austin, Texas

Although there are few cases where decimeter-level residuals exist in the residual error variation (Figures 7.8 and 7.9), there is a large majority of cases where centimeter-level residuals are present. An example of such an instance is shown in figure 7.10.

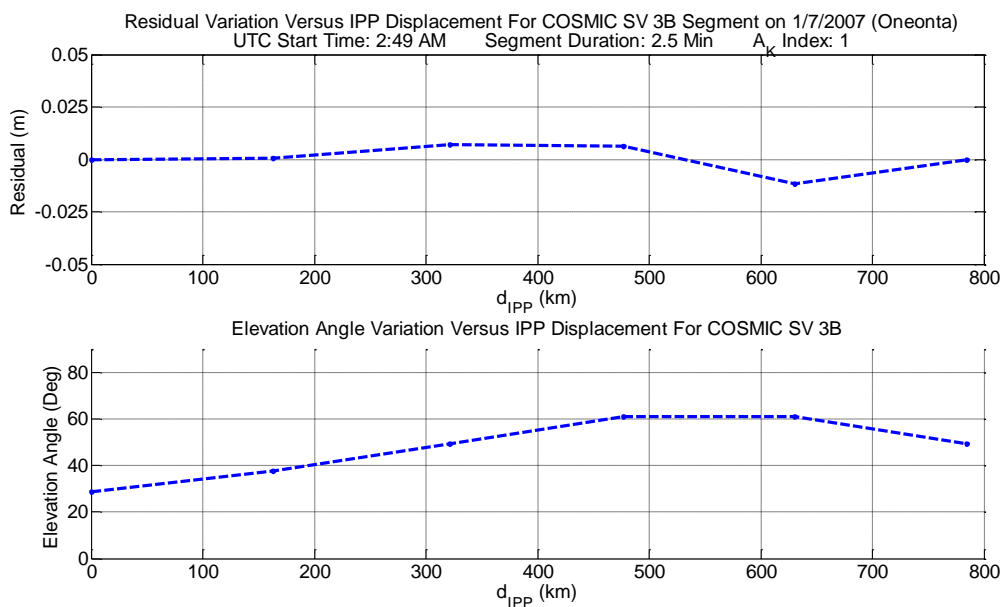


Figure 7.10. Original Model Applied to Actual LEO Data at Oneonta, New York

The folded residual error CDF plot provides visual evidence of the range of residual magnitudes generated from the application of the original vertical delay model to this LEO data. Using the two days of available data, all 700-800 km-long segments from all satellites and all sites are analyzed. This amounts to 92 segments and 778 residuals. These residuals are used to construct the plot in figure 7.11. Accompanying the folded residual CDF in the figure is the Gaussian over-bound whose standard deviation is 8.4 cm.

The residuals above 20 cm in magnitude in figure 7.8 are the ones which widen the residual error distribution of figure 7.11. This leads to the large over-bounding standard deviation since it must be inflated to account for these few points.

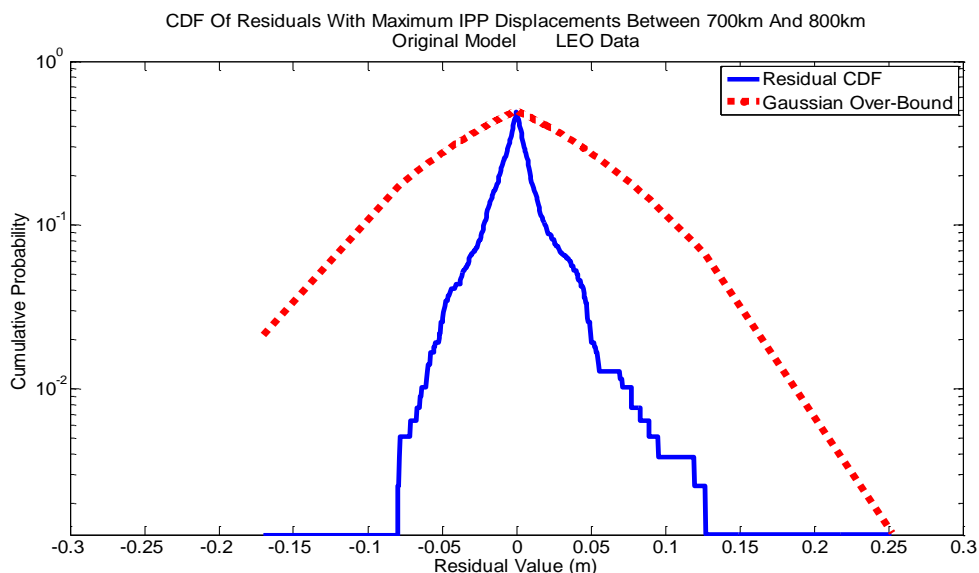


Figure 7.11. Folded Residual CDF for Original Model with Actual LEO Data

The weighted least-squares fit of the original model to this LEO data provides estimated parameter values for the bias and gradient states. Table 7.4 displays these values and their corresponding standard deviations. Since this actual data is available only as relative L1 delays, the mean  $b_{VI}$  value listed in the table is not absolute and therefore is not as significant as it is in the GPS data analysis. This also explains why the mean value is much smaller than the result obtained with GPS data.

Table 7.4. Estimated Parameter Values for Actual LEO Data with Original Error Model

State	Mean Value	Standard Deviation
$b_{VI}(\text{m})$	0.594	0.731
$g_{VI}(\text{m/km})$	$-9.34 \times 10^{-5}$	$3.35 \times 10^{-4}$

Based on the residual profiles where the largest residuals exist (Figures 7.8 and 7.9), it appears that the quadratic model may aid in reducing residual magnitudes. Implementing the quadratic model first also follows the logic presented in section 6.1 (i.e., it only introduces one additional term to the model and the error model is kept linear

with respect to its parameters). The quadratic model is applied to the data in same as way as shown in section 6.1.

Figures 7.12 and 7.13 show the comparison of the quadratic model applied to the cases producing the largest residuals with the original model (Figures 7.8 and 7.9). These figures show that the quadratic model does provide a reduction in residual magnitudes, as all residuals in both of these examples have been reduced to below 10 cm.

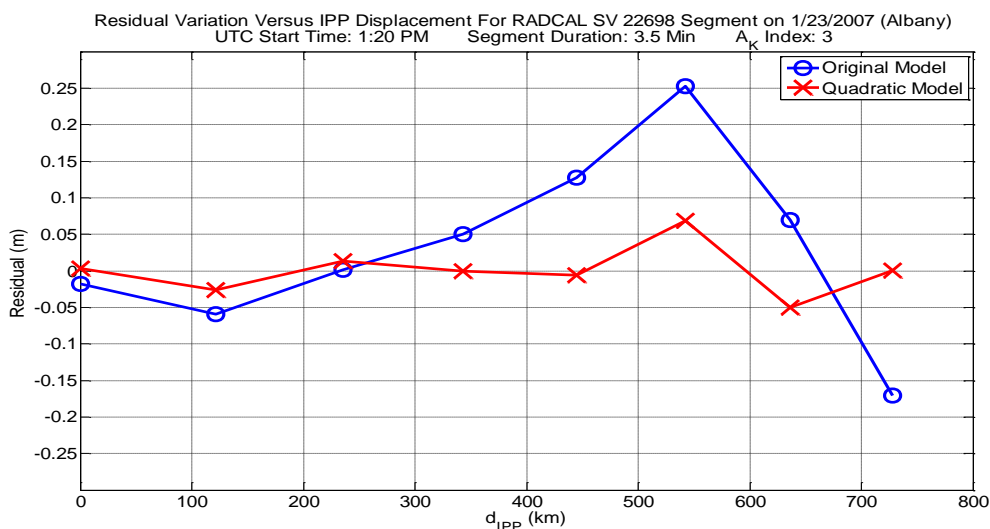


Figure 7.12. Original and Quadratic Model Comparison with Actual LEO Data at Albany, New York

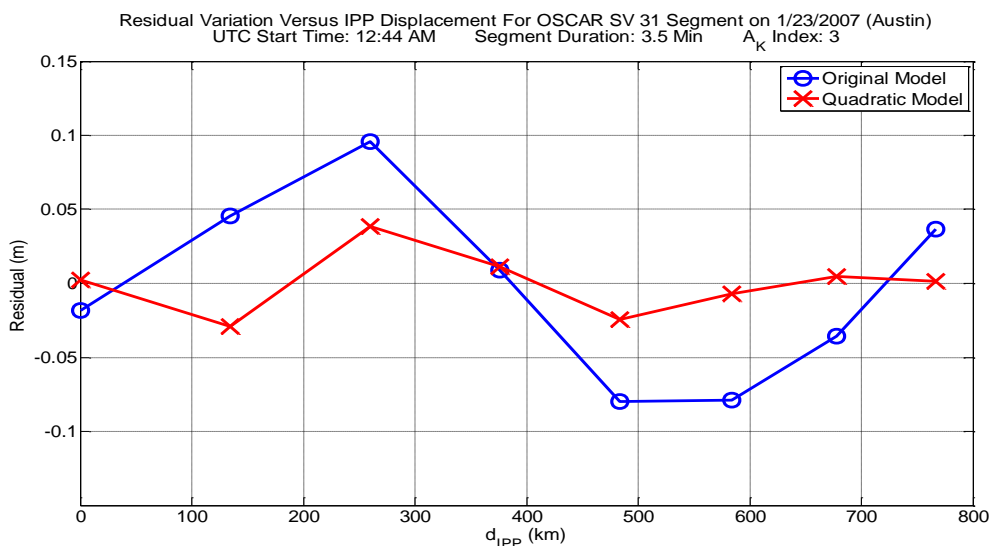


Figure 7.13. Original and Quadratic Model Comparison with Actual LEO Data at Austin, Texas

Figure 7.14 depicts the comparison of folded residual error CDFs of the original and quadratic vertical delay error models. This figure shows that the quadratic model reduces the over-bounding standard deviation of the Gaussian distribution from 8.4 cm with the original model down to 3.5 cm.

In addition to the reduction of the over-bounding Gaussian standard deviation, the maximum residual value is reduced from 25 cm with the original model to 10.31 cm with the quadratic model.

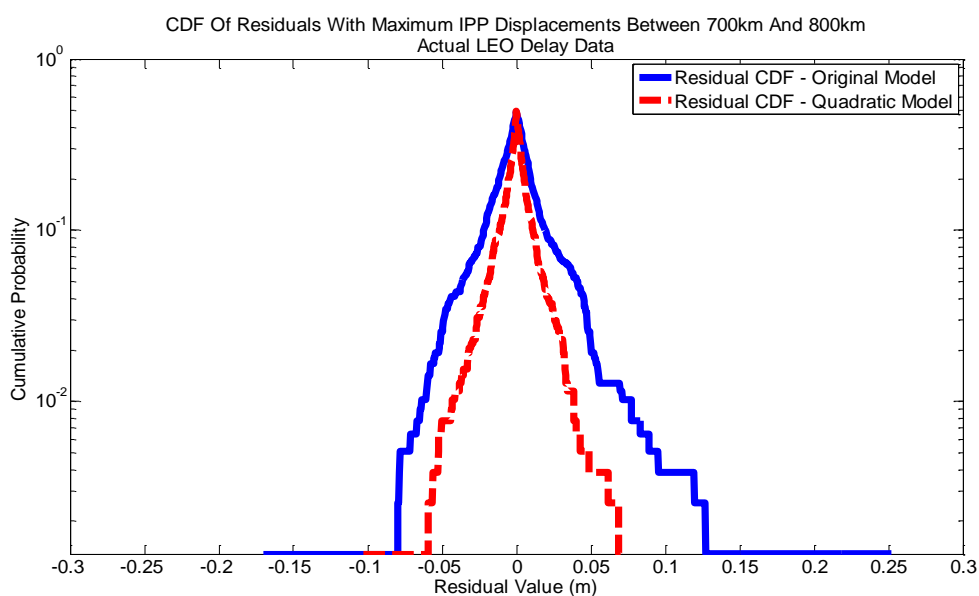


Figure 7.14. Folded Residual CDF Comparison for Original and Quadratic Models with Actual LEO Data

Table 7.5 lists the estimated parameter values and the corresponding standard deviations of these estimates obtained from the application of the quadratic model to the actual LEO data. The estimated  $b_{VI}$  value is about four times smaller than the one obtained with the quadratic model applied to GPS data. This can be explained by remembering that the L1 delays are relative for the LEO data instead of absolute as with GPS.

Table 7.5. Estimated Parameter Values for Actual LEO Data with Quadratic Error Model

State	Mean Value	Standard Deviation
$b_{VI}$ (m)	0.454	2.12
$g_{VI}$ (m/km)	$-2.09 \times 10^{-4}$	$1.01 \times 10^{-3}$
$q_{VI}$ ( $10^{-3}$ /km)	$-2.0 \times 10^{-4}$	$1.05 \times 10^{-3}$

Although the quadratic model provides an improvement in residual magnitudes, it still produces decimeter-level residuals as evidenced in the folded CDF comparison of figure 7.14. In an effort to eliminate these decimeter-level residuals, the next logical progression would be to add both a quadratic and a sinusoidal term to the model since the quadratic model provides much more improvement with LEO data than it does with GPS data (Section 6.1). However, the results of adding both these terms to the model (not shown here) does not reduce the residual magnitudes or over-bounding standard deviation much more than if the sinusoidal term was considered alone. For this reason, only the model with the sinusoidal term will be presented here. Considering only the sinusoidal term (without the quadratic) brings an added benefit: the number of error model parameters which must be estimated is kept smaller, which introduces less uncertainty into the iGPS positioning algorithms. The fewer number of states also means that system availability will be improved.

Examination of figures 7.8 and 7.9, where the largest residuals exist with the original model, show that the wavelength of the structures in these residual variations appears to be approximately 600 km. This is twice the 300 km wavelength found in the GPS analysis. This 300 km wavelength was used in chapter 6 as the initial guess value for the frequency term in order to fit the sinusoidal model to GPS data using the Newton-Raphson method. If a 300 km value is used when fitting the model to LEO data (instead

of 600 km observed in figures 7.8 and 7.9), then the model might not converge to the actual frequency. This is illustrated in figure 7.15, where the residual variation of the original model, sinusoidal model with an initial wavelength of 300 km, and the sinusoidal model with an initial wavelength of 600 km are compared using the same example as in figure 7.9. Initial values for the states (except frequency) from table 6.2 and convergence criteria (equation 6.13) used for the Newton-Raphson method are the same as the ones used in the GPS analysis of chapter 6. It is evident that the 300 km wavelength case provides little or no decrease in the largest residual magnitudes, while the 600 km wavelength case provides substantial improvement.

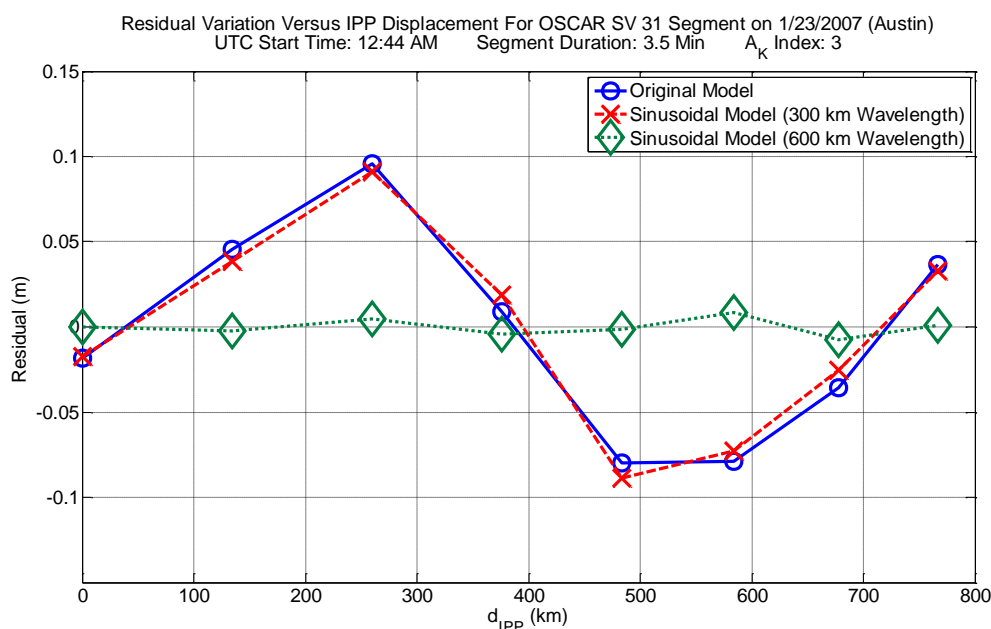


Figure 7.15. Original and Sinusoidal Model Comparison with Actual LEO Data at Austin, Texas

The difference in the observed wavelengths between the GPS and LEO data can be explained geometrically. As mentioned in chapter 3, TIDs appear as a result of collisions between the neutral particles of the thermosphere and charged particles of the ionosphere. The majority of these collisions happen at altitudes of about 100 km, which is

lower than where the largest electron concentrations are observed (assumed in this work to be at 350 km). A different pierce point displacement  $d_{IPP}$  should therefore be considered for the sinusoidal terms and for the main trend of the ionosphere (original model). For GPS satellites orbiting at 20,000 km of altitude, IPP displacements at 100 km and 350 km are very similar, in contrast these IPP displacements for LEO satellites orbiting at about 1,000 km altitude are rather different. This explains the discrepancy between observed TID wavelengths. There is no practical issue in using different wavelength values for GPS and LEO satellites.

Figure 7.16 revisits the example of figure 7.8 where the largest residuals are observed with the original model. This example shows that the model including sinusoidal vertical delay terms with an initial wavelength of 600 km significantly reduces the largest residual magnitudes. The residuals produced by the sinusoidal model in this example are smaller than those obtained with the quadratic model applied to the same segment.

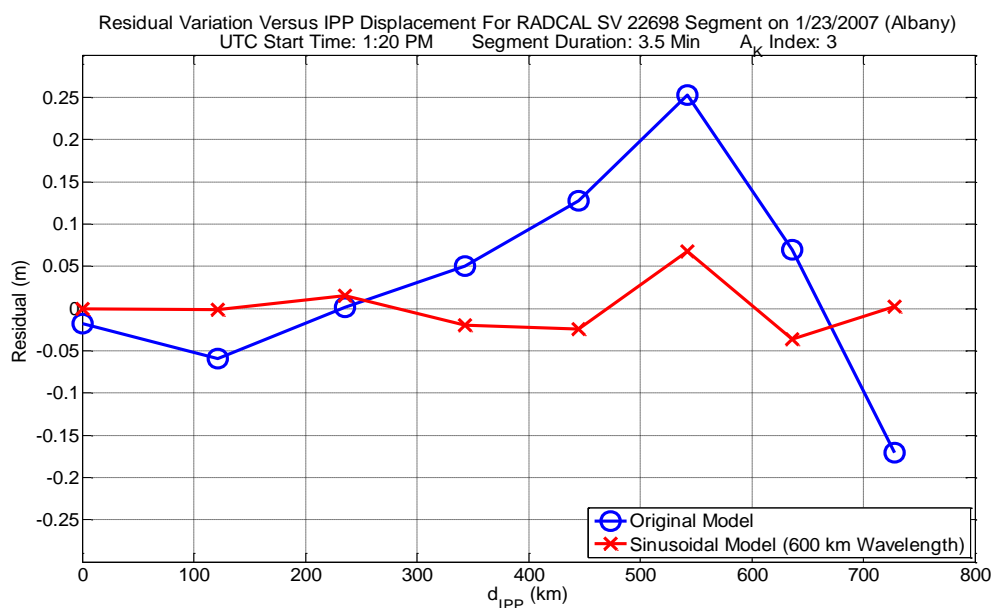


Figure 7.16. Original and Sinusoidal Model Comparison with Actual LEO Data at Albany, New York

Since the sinusoidal model with an initial wavelength of 600 km provides the greatest decrease in residual magnitudes, it will be compared to the original model results. This is done through the folded residual error CDF in figure 7.17. The sinusoidal model offers a significant improvement in the tails of the distribution by reducing the largest residual magnitude from 25.27 cm down to 6.74 cm.

Additionally, the sinusoidal model reduces the over-bounding standard deviation from 8.4 cm with the original model down to 2.3 cm. It is to be noted that the sinusoidal model is found to converge for all segments considered.

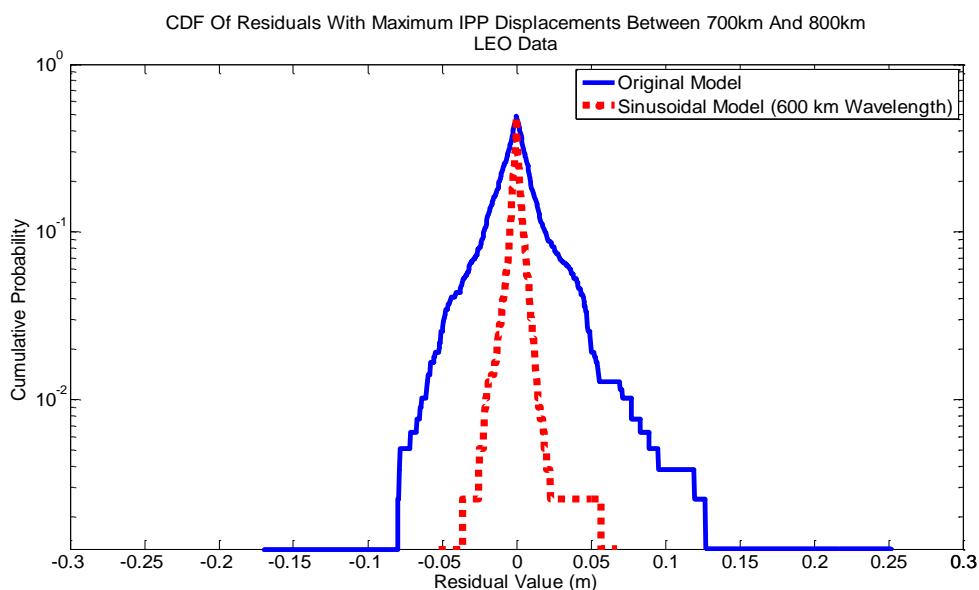


Figure 7.17. Folded Residual CDF Comparison for Original and Sinusoidal Models with Actual LEO Data

Estimated parameter values for the states of the sinusoidal model have been evaluated using the LEO data. These values are found in table 7.6. Once again, the  $b_{VI}$  estimate is smaller than the GPS analysis since the LEO data is in terms of relative L1 delay.

Table 7.6. Estimated Parameter Values for Actual LEO Data with Sinusoidal Error Model

State	Mean Value	Standard Deviation
$b_{VI}$ (m)	0.694	2.58
$g_{VI}$ (m/km)	$9.84 \times 10^{-5}$	$2.05 \times 10^{-3}$
$a_C$ (m)	-0.0046	0.098
$a_S$ (m)	-0.0322	0.504
$f_{TID}$ (1/km)	$1.59 \times 10^{-3}$	$4.45 \times 10^{-4}$

The LEO data analysis has revealed trends in the observed residual variations similar to the GPS analysis. More specifically, the vast majority of 700-800 km-long segments exhibit centimeter-level residuals with the original model. However, there are also cases where decimeter-level residuals are observed which increase the standard deviation of the over-bounding Gaussian distribution. The quadratic and sinusoidal models developed to decrease residual magnitudes have been shown to provide improvement over the original model in terms of the over-bounding standard deviation. Although the over-bounding standard deviation can be reduced to the level of the assumed measurement noise standard deviation, it is difficult to draw definitive conclusions about the robustness of the error model with LEO delays due to the limited amount of available data and the fact that this data is only for quiet ionospheric days.

Now that the error models have been evaluated with both GPS and LEO data and a baseline has been established for the quality of these models, a summary of what has been done in this work and suggestions for future work are provided in the next chapter.

## CHAPTER 8

### CONCLUSIONS AND FUTURE WORK

Carrier phase measurements can potentially enable high precision positioning applications. In order to fully exploit these carrier measurements, cycle ambiguities must be estimated. One solution for achieving real-time carrier phase positioning is to augment GPS with LEO satellites [20-22]. By exploiting the fast changes in LEO satellite geometry, cycle ambiguities can quickly be distinguished from other system states.

However, accurately estimating cycle ambiguities is challenging because satellite measurements are subject to a variety of errors. The largest and most sensitive error source is the ionosphere. To account for errors introduced by the ionosphere, this work has aimed at evaluating ionospheric error models which can be used with both GPS and LEO measurements for single frequency carrier phase positioning. A summary of the error model evaluation carried out in this work is given below.

#### **8.1 Summary of Error Model Evaluation**

The evaluation began with a nominal linear vertical delay model given in equation 3.1, which was derived in previous work [20-22]. This model was shown to provide centimeter-level residual errors in the majority of cases, both for GPS and LEO data. Decimeter-level residual errors were also discovered in the analysis. These residuals inflated the standard deviation of the Gaussian distribution over-bounding the residual errors well above the measurement noise level.

In an effort to decrease residual magnitudes, and subsequently the over-bounding standard deviation, new quadratic and sinusoidal models were derived. Since the error models must be incorporated into the iGPS positioning algorithms, practical constraints

on maximum IPP displacement and number of parameters within the model, both of which ultimately affect iGPS system availability, had to be considered when deriving them.

The maximum IPP displacement plays a role because even though applying a model over small IPP displacements (less than the 700-800 km considered in this work) ensures a good match with ionospheric data, it has been shown (Figure 5.2) that overall iGPS system availability decreases rapidly for maximum IPP displacements below 600 km. As discussed in chapter 5, this drop in system availability occurs because of the increase in the number of  $g_{VI}$  states introduced to account for each segment of a satellite pass. The increased number of parameters leads to larger uncertainty in the position solution and, therefore, a decrease in system availability. This means that the error model must be applied over IPP displacements greater than 600 km to ensure high system availability.

As mentioned above, the number of parameters in the error model is an important factor to consider because an increase in the number of error model parameters leads to greater uncertainty in the iGPS positioning solution and consequently to a decrease in system availability. Thus, even though adding more parameters will help the model to match the data more closely (i.e., help ensure integrity for the system), the addition of parameters comes at the cost of decreased system availability.

Both the quadratic and sinusoidal models have been shown to lower the largest residual magnitudes and the over-bounding standard deviations, as compared to the original model. For example, when over-bounding residual errors in the GPS analysis, the sinusoidal model decreases the standard deviation of the Gaussian distribution by 2.5 cm

(8.2 cm to 5.7 cm) over the original model. The problem is that the standard deviation is still greater than twice the measurement noise standard deviation of 2.3 cm. The residual mis-modeling error must be accounted for in high-integrity applications.

In the case of LEO delay data, the quadratic model greatly reduces the over-bounding standard deviation, although it is still higher than the assumed measurement noise standard deviation. The sinusoidal model with an initial wavelength of 600 km gives an over-bounding standard deviation of 2.3 cm. Although the over-bounding values provided by these models are at the same order of magnitude as the measurement noise, it must be remembered that the sample size is much smaller as compared to GPS data. This means that larger amplitude TIDs that might increase the tails of the residual distribution may not have been encountered.

Although the sinusoidal model shows substantial improvement over the original model in terms of residual reduction, it is more complex to implement than either the original or quadratic models. This is because it requires the input of more precise nominal parameter values as well as the standard deviations of these parameters. Other parameters such as the maximum number of iterations and the convergence threshold must be tuned. In addition, non-converging segments are also encountered which must be analyzed separately.

The results of the model evaluation show that the residual variation over time can have a wide variety of shapes (due to the presence of TIDs). Consequently, it is very difficult to develop a single ionospheric error model which will accurately capture the errors in all cases. This underlines the basic tradeoff which is at the heart of this work: The ionospheric error model must be robust enough to accurately capture the

ionosphere's uncertainty, but it should not be overly conservative or it will decrease system availability.

## **8.2 Review of Contributions**

### **8.2.1 Methodology to Analyze Ionospheric Errors using Experimental Data.**

Experimental data was obtained from a variety of sources. This data was then processed through the modified time-step method developed in section 4.2.1 using least-squares batch estimation (section 4.3.1). The processed data was used in the analysis of ionospheric delays. These delays were examined based on several parameters, including location, time of the day, level of ionospheric activity, and satellite elevation.

Data was analyzed from the year 2007 because it is between solar maxima, which means that most of the days throughout this period exhibit quiet ionospheric activity. Ionospheric delays during quiet days are expected to be more predictable and easier to model as compared to unsettled and active ionospheric days. The underlying reasoning is that if the modeling problem proves to be intractable on quiet days (for which a large amount of data is available), then there is no need to seek out and evaluate unsettled and active days.

Moreover, an elevation mask of ten degrees was used in the processing in order to help mitigate the effects of multipath which are more prevalent at low elevations. The methodology for data processing was not only employed for GPS data, but also for simulated and actual LEO data.

**8.2.2 Accuracy of a Linear Model for the Vertical Ionospheric Delay.** Dual-frequency carrier phase GPS measurements collected from seven CORS sites over eight

months have been used to analyze an initial ionospheric error model. This error model was derived in earlier work [20-22], and served as the starting point for this work.

One of the assumptions used in deriving the ionospheric error model states that the vertical ionospheric delay is assumed to vary linearly with IPP displacement up to a certain limit. Using the dual-frequency carrier phase GPS data obtained from CORS sites, this upper IPP displacement limit has been determined by considering the distribution of residual errors and the impact the limit has on iGPS system availability.

### **8.2.3 Piece-wise Linear and a Piece-wise Quadratic Model for the Vertical**

**Ionospheric Delay.** As a consequence of the upper IPP displacement limit, the error model must be applied in a piece-wise fashion to segments of satellite passes. The nominal model, which is linear with respect to the vertical ionospheric delay, was applied to the available data. Residual errors were used as the metric to determine the quality of the model by measuring how accurately the model fits the data. With the available data, over 3.7 million residual errors were computed. It was found that in the majority of cases, the model produced centimeter-level residual errors. Much less frequently observed were cases exhibiting decimeter-level residuals. These decimeter-level residuals were shown to be the result of Traveling Ionospheric Disturbances (TIDs). TIDs were analyzed and their likelihood of occurrence proved to be significant: about 1% of all GPS satellite passes were affected by decimeter-level TIDs.

Also discovered in the analysis were bow shapes in the residual error variations. To better capture these structures, a piece-wise quadratic model of the vertical ionospheric delay was developed. By applying the quadratic model to the available GPS

and LEO data, it was shown that this model does provide a decrease in residual magnitudes, most significantly with LEO data.

**8.2.4 Ionospheric Error Model to Account for TIDs.** The largest residual error magnitudes were caused by residual variations exhibiting a wave-like shape. To account for these residuals, a new harmonic model was derived, which introduces a nonlinear frequency term. Adding this term necessitates the need to perform nonlinear estimation. A Newton-Raphson method was employed for conducting the estimation in order to obtain residual errors and determine parameter values for the states in the model. The new model was found to significantly decrease the largest residual magnitudes observed with the original (nominal) model. As a result, the over-bounding standard deviation of the residual errors was reduced, indicating less mis-modeling error.

### **8.3 Future Work**

Recommendations for future work are provided below. These can be explored in an effort to make the error model more robust. It must be kept in mind that while the model needs to be robust (able to fit large amounts of data accurately to ensure integrity), it must also be kept as uncomplicated as possible (minimal number of parameters) in order to not compromise system availability.

**8.3.1 Investigation of the Impact of Decimeter-level Residuals on Positioning.** The residual errors observed with the original model in chapter 5 are at the decimeter-level. Since these are above the desired centimeter-level (measurement noise), their impact on positioning performance needs to be determined. If these residuals do not cause a major impact on positioning accuracy and integrity, the original model could be used exclusively. This would prove to be very beneficial because it contains the fewest number

of parameters of any of the error models considered in this work, which means less uncertainty would be introduced into the positioning algorithms of [20-22].

**8.3.2 Further Ionospheric Error Model Refinement.** Robustness of the error model may be achieved by refining the assumptions used to derive the error model, most specifically the thin shell approximation. The model could be enhanced if the entire effect of the ionosphere is not concentrated at one altitude. Since the total electron content (TEC) varies with altitude within the ionosphere, there may be unforeseen effects at various altitudes that the model cannot capture in its current form. To address this issue, the vertical variation of the TEC could be modeled, for example with a Chapman function [13], which would allow the model to account for the variation in the ionospheric delay as a function of altitude.

Another way to encapsulate a wider range of altitudes within the ionosphere is to create a multiple thin shell model. Each thin shell would have a different vertical ionosphere bias and gradient. Drawbacks to this approach include the introduction of several additional states and the fact that there will not be a large difference in the altitudes of the thin shells. In the case of GPS satellites, this means that the pierce point location will not change significantly from one shell altitude to another, although LEO satellites will not have this issue. Multiple thin shells could provide a more accurate representation of the error as function of altitude within the ionosphere.

The model in its current form is one-dimensional. This means IPP motion is only considered to be along a straight path across the great circle. In reality, IPP trajectories do not follow precise great circle paths. Introducing a vertical ionosphere bias and gradient

in two different directions would allow the model to become two-dimensional, leading to a more detailed representation of ionospheric errors.

**8.3.3 Analysis of a Larger Set of Experimental Data.** Quiet, unsettled, and active ionospheric days have been examined in this work. Significant time and effort have been put into understanding the model's behavior on these types of days since they occur over 99% of the time (Table 3.3). In the future, stormy days should be examined since the behavior of the ionosphere on these days is less predictable. Incorporating the results from analyzing stormy days will help to make the model more robust.

Also in this analysis, a year in the middle of an eleven-year-long solar cycle was used. To see how the model behaves with a more disturbed ionosphere, processing data from years closer to a solar maximum should be carried out. This will allow for a determination of how much larger (if at all) residual magnitudes are during a period of greater solar activity.

## BIBLIOGRAPHY

- [1] Afraimovich, E.L., I.K. Edemskiy, S.V. Voeykov, Yu. V. Yasyukevich, and I.V. Zhivetiev. "The first GPS-TEC imaging of the space structure of MS wave packets excited by the solar terminator." *Annales Geophysicae* 27 (2009): 1521-1525.
- [2] *Astronomical Applications Department*. United States Naval Observatory. <<http://aa.usno.navy.mil/index.php>>.
- [3] Cohen, C., B. Pervan, and B. Parkinson. *Estimation of Absolute Ionospheric Delay Exclusively through Single-Frequency GPS Measurements*. Proceedings of the Institute of Navigation GPS Conference, Albuquerque, NM. 1992.
- [4] *Continuously Operating Reference Stations Data*. National Geodetic Survey. <<http://www.ngs.noaa.gov/CORS/Data.html>>.
- [5] Crassidis, J. and J. Junkins. *Optimal Estimation of Dynamic Systems*. Boca Raton, FL: Chapman and Hall/CRC, 2004.
- [6] Datta-Barua, S. *personal communication*. 2009.
- [7] Datta-Barua, S. *Review of Traveling Ionospheric Disturbances*. 2009.
- [8] DeCleene, B. *Defining Pseudorange Integrity-Overbounding*. Proceedings of the Institute of Navigation GPS Conference, Salt Lake City, UT. 2000. 1916-1924.
- [9] Fossa, C., R. Raines, G. Gunsch, and M. Temple. *An Overview of the Iridium Low Earth Orbit (LEO) Satellite System*. Proceedings of the IEEE National Aerospace and Electronics Conference, Dayton, OH. 1998. 152-159.
- [10] Garner, T. *personal communication*. 2010.
- [11] *GPS Almanac Data*. United States Coast Guard Navigation Center. <<http://www.navcen.uscg.gov/archives/gps/2007/ALMANACS/YUMA/>>.
- [12] Gurevich, A.V. *Nonlinear Phenomena in the Ionosphere*. New York: Springer-Verlag, 1978.
- [13] Hansen, A. *Tomographic Estimation Of The Ionosphere Using Terrestrial GPS Sensors*. PhD Dissertation. Stanford University, 2002.

- [14] Hansen, A., J. Blanch, T. Walter, and P. Enge. *Ionospheric Correlation Analysis for WAAS: Quiet and Stormy*. Proceedings of the Institute of Navigation GPS Conference, Salt Lake City, UT. 2000.
- [15] Hansen, A., E. Peterson, T. Walter, and P. Enge. *Correlation Structure of Ionospheric Estimation and Correction for WAAS*. Proceedings of the Institute of Navigation NTM, Anaheim, CA. 2000.
- [16] Hernandez-Pajares, M., J.M. Juan, and J. Sanz. "Medium-scale traveling ionospheric disturbances affecting GPS measurements: Spatial and temporal analysis." *Journal Of Geophysical Research* 111 (2006).
- [17] Hofmann-Wellenhof, B., M. Lichtenegger, and J. Collins. *Global Positioning System: Theory and Practice*. 3<sup>rd</sup>, Revised Ed. New York: Springer-Verlag, 1994.
- [18] *Interface Control Document (ICD) GPS-200*. Revision C.  
<<http://www.navcen.uscg.gov/pubs/gps/icd200/icd200cw1234.pdf>>.
- [19] "International Reference Ionosphere." *SPDF - ModelWeb: Geophysical Models*.  
<<http://modelweb.gsfc.nasa.gov/ionos/iri.html>>.
- [20] Joerger, M. *Carrier Phase GPS Augmentation Using Laser Scanners And Low Earth Orbiting Satellites*. PhD Dissertation. Illinois Institute of Technology, 2009.
- [21] Joerger, M., J. Neale, and B. Pervan. *Iridium/GPS Carrier Phase Positioning and Fault Detection Over Wide Areas*. Proceedings of the Institute of Navigation GPS Conference, Savannah, GA. 2009.
- [22] Joerger, M., L. Gratton, B. Pervan, and C. Cohen. "Analysis of Iridium-Augmented GPS for Floating Carrier Phase Positioning." *NAVIGATION: Journal of the Institute of Navigation* 57 (2010).
- [23] Kidder, S. and T. Vonder Haar. *A Satellite Constellation To Observe The Spectral Radiance Shell Of Earth*. Proceedings of the Conference on Satellite Meteorology and Oceanography. 2004. 1-5.
- [24] Lee, J., S. Pullen, S.Datta-Barua, and P. Enge. *Assessment of Nominal Ionosphere Spatial Decorrelation for LAAS*. Proceedings of the Institute of Navigation PLANS Conference, San Diego, CA. 2006.
- [25] Mayaud, P.N. *Derivation, Meaning, and Use of Geomagnetic Indices*. Washington, D.C.: American Geophysical Union, 1980.

- [26] Misra, P. and P. Enge. *Global Positioning System: Signals, Measurements, and Performance*. 2<sup>nd</sup> Ed. Lincoln, MA: Ganga-Jumuna Press, 2006.
- [27] O’Keefe, J.M., D.A. Campbell, and L.W. Cahill. *Frequency Estimation Of Traveling Ionospheric Disturbances*. Proceedings of the IEEE Symposium on Circuits and Systems, Atlanta, GA. 1996.
- [28] Olynik, M., M.G. Petovello, M.E. Cannon, and G. Lachapelle. *Temporal Variability of GPS Error Sources and Their Effect on Relative Positioning Accuracy*. Proceedings of the Institute of Navigation NTM, San Diego, CA. 2002.
- [29] Pervan, B., D. Lawrence, and B. Parkinson. *Autonomous Fault Detection and Removal Using GPS Carrier Phase*. IEEE Transactions On Aerospace And Electronic Systems. 1998.
- [30] RTCA Special Committee 159. “Minimum Aviation System Performance Standards for the Local Area Augmentation System (LAAS).” RTCA/DO-245. Washington, D.C., 2004.
- [31] RTCA Special Committee 159. “Minimum Operational Performance Standards for Global Positioning System/Wide Area Augmentation System Airborne Equipment.” RTCA/DO-229C. Washington, D.C., 2001.
- [32] Simon, D. *Optimal State Estimation: Kalman,  $H_{\infty}$ , And Nonlinear Approaches*. Hoboken, NJ: John Wiley and Sons, 2006.
- [33] Tascione, T. *Introduction to the Space Environment*. 2<sup>nd</sup> Ed. Malabar, Florida: Krieger Publishing Company, 1994.
- [34] Tsugawa, T., Y. Otsuka, A. Coster, and A. Saito (2007). “New Characteristics of Medium- Scale Traveling Ionospheric Disturbances Detected with Dense Wide-Coverage TEC Maps over North America.” *Geophysical Research Letters* 34 (2007).
- [35] Tsui, J. *Fundamentals of Global Positioning System Receivers: A Software Approach*. New York: John Wiley and Sons, Inc., 2000.